A Sparse Representation-Based Framework for Preprocessing Brain MRI

On the Road to Identifying Biomarkers of the Offending Brain

Nallig Eduardo Leal Narváez

Supervised by Eduardo Zurek

Systems Engineering and Computing

Division of Engineering

Universidad del Norte

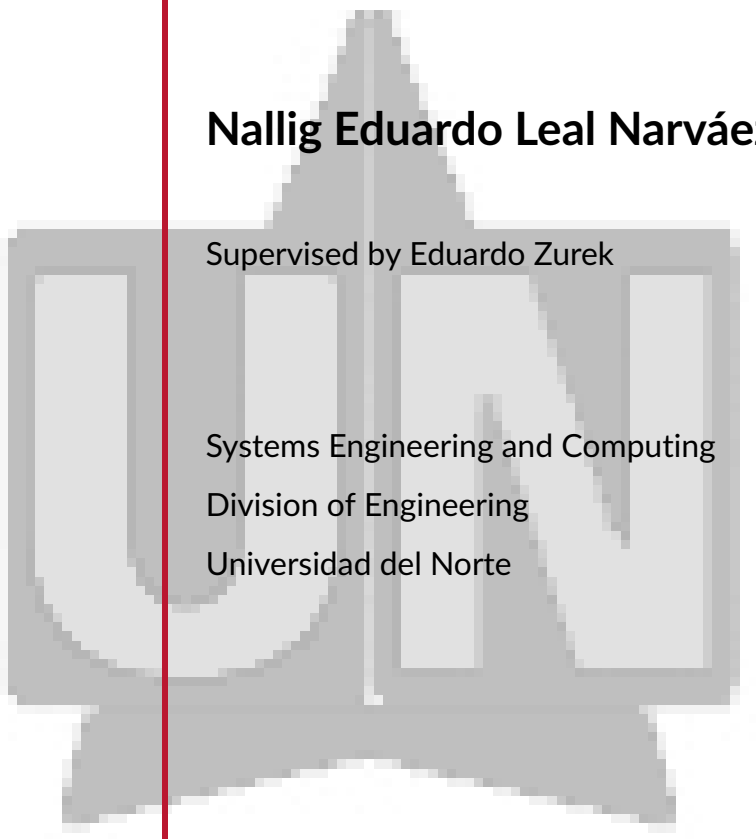

April, 2020

A dissertation submitted in partial fulfilment of the requirements for the degree of Ph.D. in Systems Engineering and Computing.

Declaration by Postgraduate Students

Authenticity of Dissertation

I hereby declare that I am the legitimate author of this Dissertation and that it is my original work.
No portion of this work has been submitted in support of an application for another degree or qualification of this or any other university or institution of higher education.
I hold the Universidad del Norte harmless against any third party claims with regard to copyright violation, breach of confidentiality, defamation and any other third party right infringement.

Faculty/Institute/Centre/School	Division of Engineering
Degree	Ph.D. in Systems Engineering and Computing
Title	Sparse Representation-Based Framework for Preprocessing Brain MRI
Candidate	Nallig Eduardo Leal Narváez

Signature of Student	_____
Date	June 3, 2020

To my beloved Greace, Thomas and Andrés

For their constant support and patience during the journey on this long and difficult road.

Acknowledgements

The completion of this thesis has required all my effort and dedication. However, it would not have been possible without the contribution of many people. I especially want to thank my wife and children for understanding that the time I stopped being with them was to dedicate to my studies. I want to thank their full support and understanding.

I want to thank my parents for instilling in me the desire to study and improve myself, that is one of the reasons why I decided to do doctoral studies.

I want to thank my director Eduardo Zurek for trusting that I could lead this work and for allowing me to make my own decisions. I want to thank Dr. Mariana Pino for supplying the images that are the object of this study.

I can't stop thanking Professor José Vicente Manjón for his support during my internship in the Polytechnic university of Valencia and because his collaboration was essential in achieving the third objective of my research, which is the spirit of this thesis.

I want to thank my brother Esmeide for helping me to understand the fundamental theory on which my work is based, the Sparse Representations. Without his help it would have been much more difficult to achieve my goals.

Finally, I want to thank the Administrative Department of Science and Technology of Colombia—COLCIENCIAS, beacuse they support me with a scholarship of the program of doctoral scholarship COLCIENCIAS-UNINORTE 2015-006. Without that support this thesis it would not have been possible.

Abstract

Adolescence is a particular period of risk to trigger criminal behaviors. These criminal behaviors, in the case of young offenders, are for all purposes a mental health problem whose treatment is likely to improve its results if it is identified early. However, a potential risk factor, alterations of brain structures, has been neglected. A common way for identifying alterations of brain structures is by analyzing brain Magnetic Resonance (MR) Images. However, typically this type of images suffers from problems like noise, blurring, low contrast, and in-homogeneity, among others, which difficult the analysis of the image.

Analyzing an MR image implies to deal with the above problems. Although such problems have been addressed by previous works, this is still an open field of research. This thesis addresses the use of sparse representations, specifically Dictionary Learning and Sparse Coding, for pre-processing brain MR images, so that the processed image retains the fine details of the original image, to improve the segmentation of brain structures, in order to assess whether there is any relationship between alterations in brain structures and the behavior of young offenders.

A novel method for MR images denoising is presented. Denoising an MR image while keeping fine details is a difficult task; however, the proposed method, based on sparse representations, Non-Local Means (NLM), and Singular Value Decomposition (SVD) can filter noise while prevents blurring, artifacts, and residual noise.

A novel method for improving the boundaries between segmented regions of an MR image is presented. Segmenting an MR image is a non-trivial task; because, normally the limits between regions in these images may be neither clear nor well defined, due to the aforementioned problems which affect MR images. However, our method, from both the label matrix of the segmented MR image and the original image, yields a new improved label matrix in which the limits among regions are better defined.

The method for improving the boundaries definition between segmented regions was applied to a case study. This case study was aimed to relate alterations of brain structures with offending behaviors in young people. For such a purpose, the widely recognized online brain MR Imaging volumetry system, volBrain was used. The results obtained with volbrain were re-processed using the method for improving boundaries of segmented regions, showing interesting results.

Keywords — Biomarkers identification, boundaries improvement, brain structures analysis, dictionary learning, image denoising, image segmentation, MR Images, non-local filtering, singular value decomposition, sparse coding, sparse representation, young offenders.

Contents

List of Figures

List of Tables

List of Abbreviations

DTI Diffusion Tensor Imaging xv
EEG Electroencephalography 13
fMRI Functional Magnetic Resonance Imaging 13
ICA Independent Component Analysis 13
MR Magnetic Resonance xi
MEG Magnetoencephalography 14
NLM Non-Local Means xi
RF Radio frequency 12
SVD Singular Value Decomposition xi

Part 1

This part of the document presents both the basics and theories that explain the behaviour of peoples as a function of some brain structures, like the limbic system, and the basics of computer sciences theories that support the methods proposed in this thesis. It Presents fundamental concepts or topics like Biomarker, MR Imaging, and the social and mathematical background of this thesis. Finally, it presents in detail the proposed method for denoising MR images, and the method for improving the boundary definition of the brain structures on a segmented brain MR image.

1

Introduction

1.1 | Social motivation

Early diagnosis is essential for successful treatment of a mental illness; however, achieving it is more difficult than it appear. Even for experts in psychiatry or neurology is very difficult to identify when an individual begins to present symptoms of a mental illness, even using clinical tests. The physiological condition of the brain of young offenders is for all purposes a mental health problem whose treatment is likely to improve its results if it is identified early. This problem has received a growing interest that has led from the development of research focused on establishing relationship between brain structures alterations and criminal behavior (Cope et al. (2014)), to re-evaluate the assessment and treatment options that are available for youth within correctional facilities (Odgers et al. (2005)) and propose a dynamic system of care that extends beyond mere treatment within juvenile justice, since these people require a different system of care, a different intervention model, and a juvenile justice system that provide them with mental health services (Underwood and Washington (2016)). Early identification of young offenders could prevent or reduce social problems of delinquency in adults.

Previous research suggests that, the behavior of youths who have committed homicide may have origin on the abnormality of some brain structures (Cope et al. (2014)). This indicates that there could be biomarkers that explain the behavior of young criminals. This thesis, tries to contribute in the line of research focused on establishing a relationship between brain structures alterations and criminal behaviors in young people. Therefore, it is focused on finding such alterations.

1.2 | Computer sciences motivation

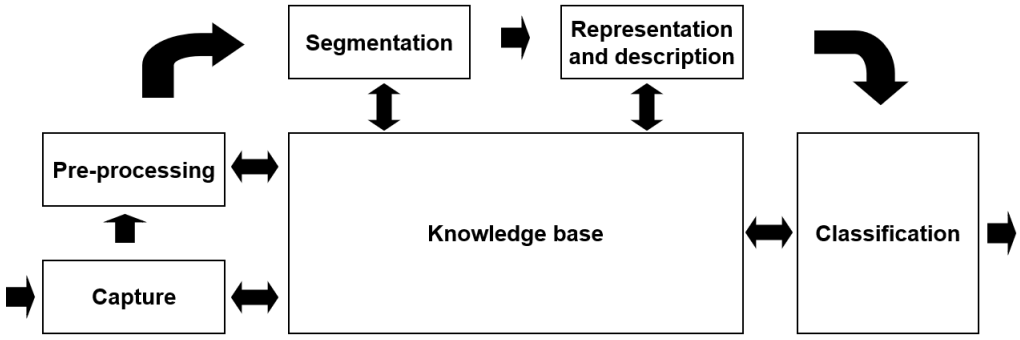

Figure 1.1: Fundamental stages of digital image processing Gonzalez and Woods (2017)

Digital image processing has always brought challenging problems to the computer science community. Generally, processing an image involves to carry out a set stages, like presented in Figure 1.1, which are expected will lead us to the solution of a problem (Gonzalez and Woods (2017)). The nature of the problem will determine what steps we should perform. For example, if we want to improve the appearance of an image, we should deal with the Capture and Pre-processing stages. However, if we only have the images and it is not possible to intervene in the capture process, we should focus on improving the appearance of the image based on some assumptions of its capture process. In addition, depending on what the final objective is, the image treatment should focus on highlighting or preserving certain characteristics.

For our case, finding alterations of brain structures, which it is supposed are minimal and can constitute a biomarker, for identifying young offenders, it would be necessary to focus on analyzing brain MR Images accurately. However, typically this type of images suffers from problems like noise, blurring, low contrast, and inhomogeneity, among others, hindering the analysis of the image and therefore the identification of such alterations.

Correcting these problems while keeping fine details on the MR image, which probably underlie the differences between the brain structures of young offenders and those who are not, is not an easy task and is still an active field of research that motivates the interest of the computer science community.

1.3 | Goal of this thesis

This thesis addresses the problem of improving the image denoising and image segmentation tasks, towards the identification of brain biomarkers of the behaviour of young offenders. Therefore, focuses on both denoising brain MR images while keeping fine details like edges and small structures, and improving the boundaries definition between brain structures.

In this context, the following are the objectives of this work

1.3.1 | General

Propose methods, based on sparse representations, for preprocessing brain MRI towards identification of biomarkers of the offending brain

1.3.2 | Specifics

1. Propose a method based on sparse representations for denoising brain MRI keeping fine details

2. Propose a method based on sparse representations for improving the definition of the boundaries of brain structures in a segmented MRI

3. Identify brain structure alterations of individuals with offending behavior from brain MRI

1.4 | Contributions

This thesis started from the following three questions:

1. Is it possible to filter the noise of brain MR images using sparse representations, while both preventing blurring and keeping fine details of the MR images?

2. Is it possible to improve the boundary definition of the regions on a segmented brain MR image using sparse representations?

3. Are there brain biomarkers of young individuals with offending behavior?

Hence, the following contributions were made:

1. Regarding the denoising method, it was possible to fully exploit the sparse representation (known as Dictionary Learning) to improve the filtering of the image while keeping fine details, avoiding the blurring effect and reducing the residual noise that remains after the denoising process.

2. Regarding the edge improvement method, the sparse representation was novelly used to create a method that corrects the edges of segmented regions, which is robust to noise and blur.

3. Finally, it was possible to characterize the alterations of some brain structures possibly related to the behavior of young offenders.

Such contributions are supported on the results here presented, and on the following publications:

1. Leal, N.; Zurek, E.; Leal, E. Non-Local SVD Denoising of MRI Based on Sparse Representations. Sensors 2020, 20, 1536.

2. Leal, N.; Zurek, E. A Simple Sparse Representation-based Method for Improving the Boundaries Definition among Segmented Regions from Grey Level Digital Images. In Proceedings of the 11th International Multi-Conferences on Complexity, Informatics and Cybernetics: IMCIC 2020, Orlando, Florida, USA, 10-13 March 2020.

3. Leal, N.; Moreno, S.; Zurek, E. Simple method for detecting visual saliencies based on dictionary learning and sparse coding. In Proceedings of the 14th Iberian Conference on Information Systems and Technologies (CISTI), Coimbra, Portugal, 19–22 June 2019; IEEE: Piscataway, NJ, USA, 2019; pp. 1–5. doi:10.23919/CISTI.2019.8760988.

4. Leal, N.; Zurek, E. A New Approach on Skull Stripping of Brain MRI based on Saliency Detection using Dictionary Learning and Sparse Coding. Prospectiva 17, 2, 2019.

Some other contributions made during the development of this thesis were

1. Gamarra, M.; Meriño, I.; Calabria, J. C.; Gutierrez, O.; Barrios, M.; Leal, N.; Wightman, P. Privacy perception in location-based services for mobile devices in the university community of the north coast of Colombia. Ingeniería y Universidad, 23, 1, 2019.

2. Hernández-Julio, Y.; Jimeno, M.; Leal, N.; Muñoz, H.; Nieto, W. "Framework for the development of Business intelligence using computational intelligence and service-oriented architecture". in 12th Iberian Conference on Information Systems and Technologies (CISTI), Lisbon, Portugal, 2017, pp. 1-7.

1.5 | Overview of this thesis

The remaining of this thesis is organized as follows:

Chapter 2 presents both the physiological and computer sciences basics of this thesis. It presents the brain networks, and the fundamental brain structures related to human behavior. In addition, it presents the mathematical and statistical tools used in this research. It focuses on inverse problems from the Bayesian point of view and its relationship with the sparse representations. The NLM basics and SVD basics are also presented.
Chapter 3 presents the proposed method for denoising MR images while preventing blurring and keeping fine details.
Chapter 4 presents the proposed method for improving the boundaries definition between brain structures on a segmented brain MR image.
Chapter 5 presents the statistical analysis for discovering and characterizing possible biomarkers that may partially explain the behavior of young offenders
Chapter 6 presents the application of the method for improving the boundaries between regions for defining more accurately the biomarkers found in Chapter 5.

2

Background

This chapter presents the basics that support both the social and physiological theories that explain the behavior of young offenders, as well as the theories of the proposed methods of this framework for the pre-processing of MR images.

2.1 | Physiological background and cerebral data acquisition

This section presents the fundamental theories and concepts of the behaviour of people, focusing on theories that try to explain the physiological reasons of the why of the behaviour of young offenders.

2.1.1 | Biomarker

A biomarker or biological marker is "a characteristic that is objectively measured and evaluated as an indicator of a normal biological processes, pathogenic processes, or pharmacologic responses to a therapeutic intervention" (Biomarkers Definitions Working Group (2001)). Biomarkers can be used for diagnosis, prognosis, staging or prediction and monitoring of the clinical response of a disease to a therapeutic intervention (Prescott (2013)). Biomarkers can be classified in three main categories, Hormonal, Neuropsychological and Neurophysiological.

Hormonal Biomarkers refers to endocrinological markers for assessing the vulnerability to a specific disorder. For example: adrenocorticotropin hormone (ACTH), testosterone cortisol ratio, and hypothalamic pituitaryadrenal (LHPA) axis.

Neuropsychological biomarkers concerns to changes in higher psychological functions involved in the efficient processing of information. For example, executive function, attention network, psychomotor performance, and decision making.

Neurophysiological biomarkers concerns brain potentials, and changes in sensorial and galvanic responses. For example, event-related potentials, electroencephalography, autonomic stress reactivity (startle reflex modulation, Skin conductance reactivity, electromyography, heart rate, and pupillary reflex (Valencia and Cuartas (2016)). This thesis focuses on neurophysiological biomarkers, which may be presented by young individuals in condition of offenders and can be revealed by MR imaging techniques.

2.1.2 | Limbic system

The limbic system is a system made up of various brain structures that regulate physiological responses to certain stimuli. The limbic system is the origin of human instincts. These instincts include involuntary memory, hunger, attention, sexual instincts, pleasure, fear, aggressiveness, personality, and behavior. It is made up of parts of the thalamus, hypothalamus, hippocampus, cerebral amygdala, corpus callosum, septum, and midbrain (Schacter et al. (2011)).

The Septo-Hippocampal theory (Blair et al. (2001)), the Amygdaloid theory (Sato et al. (2011)), and the Connectivity theory (Craig et al. (2009)), suggests that some dysfunction in this system may result, among other things, in the Antisocial Personality Disorder (ASPD). However, this theories can not fully explain all the cases of ASPD, which suggests that other brain structures may determine the behaviour of a person, and therefore serching for behavioral biomarkers shoud not be only focused on the limbic system but in the whole brain.

2.1.3 | Brain networks

The human brain is a network of approximately 100,000 million of neurons, where a neuron can interconnect up to approximately 10,000 other neurons; hence their physiology is very complex. The study of brain functions is based both on the identification of the active regions and on the functional interactions between them. The first one is known as functional segregation, which is the activation of specialized brain regions. The second one is known as integration, which is the coordinated activation of large numbers of neural regions distributed across different cortical areas, constituting a large-scale distributed system of the cerebral cortex (Friston (2009)).

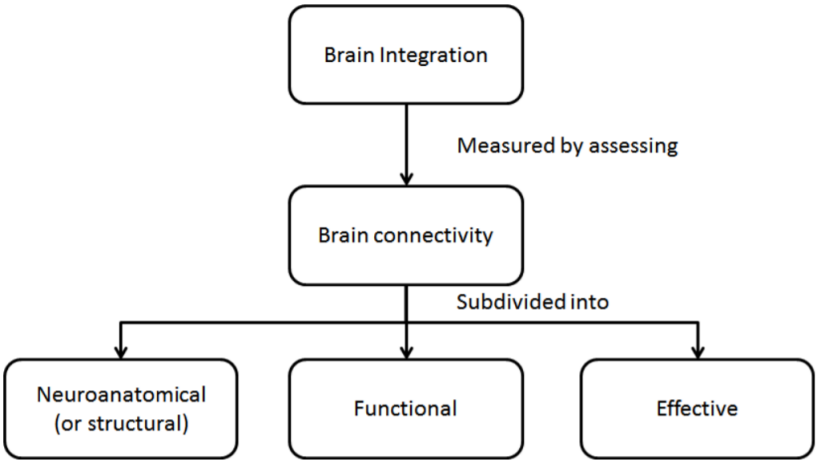

Figure 2.1: General diagram of cerebral connectivity

The cerebral connectivity is divided into neuroanatomical or structural connectivity, functional connectivity and effective connectivity. Figure 2.1 presents a diagram that facilitates the understanding of cerebral connectivity

2.1.3.1 | Neuroanatomical or structural connectivity

The neuroanatomical or structural connectivity can be considered as "Routes of extended fibers on broad regions of the brain according to the general anatomical knowledge" (Koch et al. (2002)). Structural connectivity can be verified through magnetic resonance imaging.

2.1.3.2 | Functional connectivity

Functional connectivity is the temporal correlation (in terms of significant dependencies) between the activity of different neural regions (Fingelkurts et al. (2002)). Many neurophysiological signals can be evaluated using functional connectivity techniques, such as EEGs and MEGs.

2.1.3.3 | Effective Connectivity

Effective connectivity is the direct or indirect influence exerted by one neural system on another. It describes the dynamic directional interactions between brain regions (Horwitz (2003)). It can be estimated directly from signals or models that specify causal links; for example, those based on the combination of functional and structural connectivity. It is measured very well with EEG and MEG.

2.1.4 | Methods for acquisition of cerebral data

This section presents some of the most important techniques for acquiring cerebral data.

2.1.4.1 | MR Imaging

Is a non-invasive radiology technique, which allows obtaining internal information from the human body through detailed and high contrast images for diagnostic purposes in the medical field. MR imaging bases its operation on the phenomenon of magnetic resonance, avoiding the use of ionizing radiation, as in the case of Computerized Tomography (CT). The working principle of the magnetic resonance phenomenon (Bloch (1946); Bloch et al. (1946); Purcell et al. (1946)) is the interaction between an external magnetic field and an atomic nucleus that have a magnetic moment different from zero.

Nucleus of certain atoms, are able to absorb and emit energy by being excited by Radio frequency (RF) signals when they are inside of an intense magnetic field. The nucleus of the hydrogen atom has magnetic moment different from zero. This is the more common and simple atom in the nature, since it is composed of a nucleus that has a single proton and a single electron orbiting around it. Hydrogen atoms are found in abundance in the soft tissues of the human body and have a random orientation.

By subjecting the atoms to a very strong magnetic field, the protons of their nucleus rotate with a precessional motion that allows them to absorb energy when exposed to RF wave impulses. When the RF wave disappears, the nucleus releases the absorbed energy in the form of the same wave. The generation of magnetic resonance imaging is based on capturing the energy released by the protons and analysing it in a computer that transforms into images. Figure 2.2 illustrates the MR imaging scanning process.

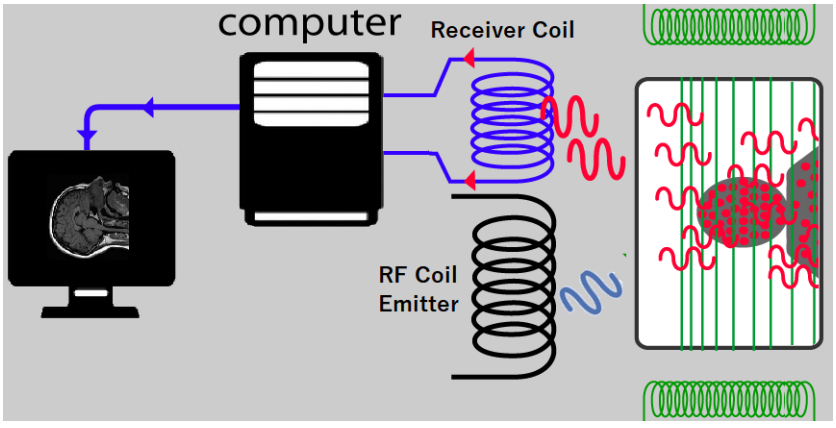

Figure 2.2: Illustration of the MR imaging scanning process

2.1.4.2 | Functional Magnetic Resonance Imaging (fMRI)

fMRI is a procedure based on magnetic resonance imaging that allows to measure brain activity from the detection of changes associated with blood flow (Rinck (2015)). fMRI uses the blood level dependent contrast (BOLD) found by Seiji Ogawa (Ogawa et al. (1990)). The evaluation of resting brain networks using the BOLD response can be performed by several methods, the seed-based approach and the Independent Component Analysis (ICA) are the most used. The seed-based approach uses regressions to examine the temporal coherence between a selected voxel and all of the other voxels in the brain (Uddin et al. (2008)). Such an approach is used to examine the temporal coherence between regions as well as functional connectivity. In (Biswal et al. (1995)) the use of this technique is presented. The ICA method is a non-model approach that decomposes data into independent components representing time characteristics and spatial signatures of the underlying sources of the recorded mixed signals (McKeown et al. (1998)).

2.1.4.3 | DTI

DTI is an MRI-based neuroimaging technique that allows to estimate the location, orientation and anisotropy of the white matter tracts of the brain. The images constitute a relatively new method of magnetic resonance that allows quantifying the degree of anisotropy of water protons in tissues. Anisotropy is the property of normal brain tissues that depends on the directionality of water molecules and the integrity of white matter fibers. The tractography is the 3D representation of DTI and can be plotted by means of a color map obtained from the directionality of the displacement of water molecules along the tracts of white matter, and in the three axes of space: "x" right-left, "y" antero-posterior and "z" face-caudal.

By convention the "x" or commissural tracts appear in red color, such as, for example, callused fibers. The tracts of the "y" axis that represent interlocking connecting fibers have green tonality; and the tracts of the axis "z" are the blue ones; for example, the pyramidal beam, as Figure 2.3 illustrates. The first experiences with DTI have awakened interest and expectations about its diagnostic and prognostic utility in stroke, sclerosis in plaques, diffuse axonal injury, as well as in certain mental illnesses and particularly in the study of brain tumors (Romero et al. (2007)).

2.1.4.4 | Electroencephalography (EEG)

It is a test that measures the electrical activity of the brain, so that it is used to detect failures related to this activity. Normal brain activity has recognizable patterns; therefore,

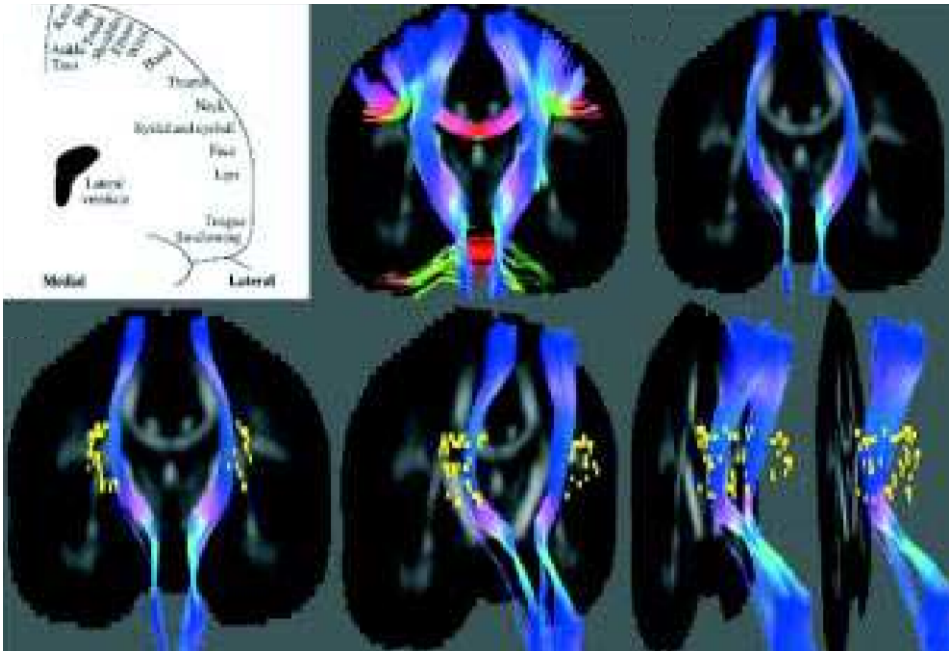

Figure 2.3: Representation of a DTI in 3D (Taken from Romero et al. (2007))

a physician can detect faults through an EEG by observing alterations in these patterns. Through an EEG, alterations can be detected that suggest diseases such as epilepsy or dementia (Henderson et al. (2006)).

2.1.4.5 | Magnetoencephalography (MEG)

It is a methodology through which the electromagnetic correlations of brain activity can be examined. MEG acts as a test of direct neural activity in real time (to the order of milliseconds) and can provide high spatial resolution (to the order of millimeters) when used with structural models. Hence MEG is useful in the study of several mental diseases, like Parkinson's disease, Alzheimer's disease, and mild cognitive impairment, among others (Bosboom et al. (2006); Mandal et al. (2018); Osipova et al. (2006); Stam et al. (2006)).

Table 2.1 summarizes the main characteristics of the methods presented for capturing information of brain activity. Given the characteristics of MR imaging to obtain high precision data of brain structures, Chapter 5 will review some works oriented to the analysis of MR images in search of biomarkers. Next section will present some issues that MR images can suffer, which are necessary dealing with, when it comes to MR images processing.

Method	Temporary resolution	Spatial resolution	Connectivity
EEG	High (ms)	Low (cm)	Functional and Effective
MEG	High (ms)	Low (cm)	Functional and Effective
MRI	Low (s)	High (mm)	Structural
fMRI	Low (s)	High (mm)	Functional
DTI	Low (s)	High(mm)	Structural

Table 2.1: Characteristics of the methods for capturing data of brain activity

2.1.5 | Artifacts in MR imaging

Typically, MR images may show feature information that is not present in the original object. Such feature information is known as artifacts, and can seriously affect the image, even compromising its diagnostic quality. The origin of the artifacts is very varied and may be caused by hardware or software problems, as well as by physical restrictions, human physiological phenomena, or causes as simple as the movement of patients during the scanning process (Budrys et al. (2018)). Below are some of the most common artifacts that MR images present.

2.1.5.1 | Movement artifacts

Movements are one of the most important source of artifacts in MR images. Typical movements are the breathing, the heartbeats, and the blood vessels pulsations among others. These movements cause ghosting artifacts and blurring. Figure 2.4 show some movement artifacts.

Figure 2.4: Movement artifacts. From left to right, artifact due to movement of the patient, Artifact due to pulsations (marked by one arrow), and artifact due to the eye balls movement (marked by two arrows) (Taken from Budrys et al. (2018))

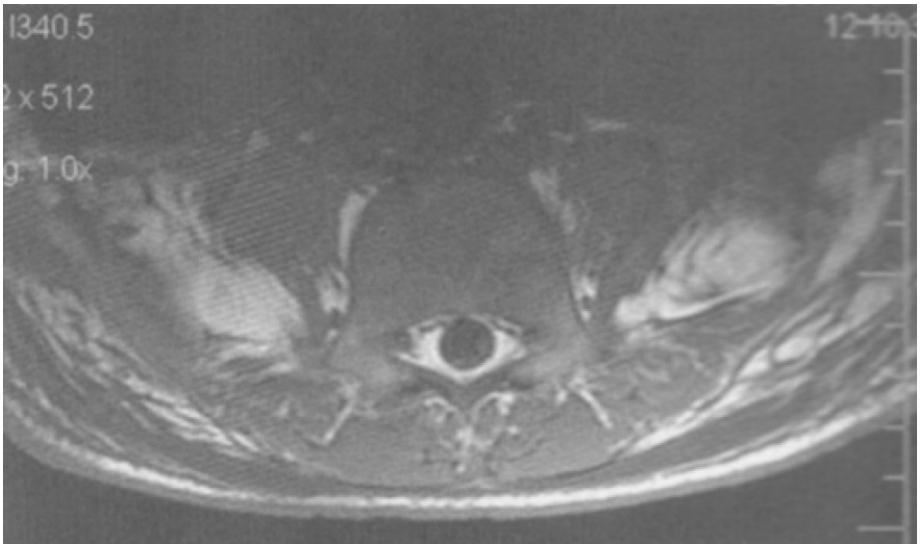

Figure 2.5: B0 inhomogeneity. Intensity distortion across a T1 axial study of the lumbar vertebrae (Taken from Erasmus et al. (2004))

2.1.5.2 | Magnetic field artifacts

Uncontrolled variations of magnetic fields may cause artifacts in the imagined object. This variations may occur due to both external magnetic fields and deviations in the gradient of the resonator magnetic field. As a consequence, the resulting image presents distortions in the intensity levels of its voxels, known as inhomogeneity. Inhomogeneity due to external magnetic fields is also called B0 Inhomogeneity. Inhomogeneity due to variations in the resonator gradient is also called B1 inhomogeneity.

Inhomogeneity occurs because the magnetic field gradients are used to encode the location of the excited proton signals within the volume being imagined; therefore, any deviation in the gradient results in a distortion of the intensity of the voxel. As the distance from the center of the applied gradient increases, a loss of field strength occurs at the periphery (Erasmus et al. (2004)). This is especially noticeable on coronal and sagittal images. Figure 2.5 shows a B0 inhomogeneity artifact.

2.1.5.3 | RF artifacts

As with magnetic field artifacts that may be due to internal or external causes to the resonator, there are radio frequency artifacts that can be caused either by internal failures in the RF coil or by the interference caused by external sources that occupy the same bandwidth than the resonator instruments.

RF artifacts can be reflected in the image as noise, which can be commonly generated

Figure 2.6: Some common artifacts caused by RF issues. From left to right Noise (Taken from Zhuo and Gullapalli (2006)) and Quadrature ghost (Taken from Oghabian (2020))

by devices such as computers, radios, televisions, or even fluorescent lamps. Inhomogeneity can also be an RF artifact. This may be due to a non-uniform sensitivity of the receiving coil. Quadrature Ghosts is also a RF artifacts. These are usually caused when one detector channel has a higher gain than the other (Erasmus et al. (2004)). Figure 2.6 presents some common RF artifacts.

2.1.5.4 | Signal processing artifacts

Partial volume artifacts and Gibbs artifacts are the most common signal processing artifacts. Partial volume is due to hardware limitations which cause that objects smaller than the voxel be lost or averaged with other tissues. Gibbs artifacts are caused by the under-sampling of high spatial frequencies at sharp boundaries in the image (Erasmus et al. (2004)). Figure 2.7

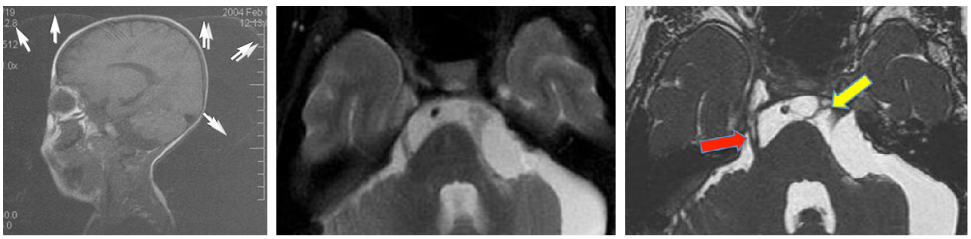

Figure 2.7: Signal processing artifacts. The image on the left show an example of Gibbs artifact (Taken from Erasmus et al. (2004)). The image on the center shows an example of partial volume artifact of the image on the right. It can be seen how the details pointed out by the red and green arrows are lost in figure on the center (Courtesy of Elster (2020))

2.2 | Computer sciences background

This section presents the fundamental theories and concepts where the proposed methods in this thesis are based on. Mathematical and statistical tools for processing digital images and optimization techniques are also described. In particular, the concepts of inverse problems and the Bayesian theory, the sparsity visual theory and its mathematical representation as sparse vectors are the core of the methods presented in the remaining chapters.

2.2.1 | Inverse Problems

Commonly, information systems process input signals to extract relevant information. It is inevitable that, during the process of capturing information through a sensor, there exist some degradation of the signal being measured. This degradation can be caused by technological limitations, electronic noise, or electromagnetic radiation, among others. These are typical factors that reduce the signal quality. Therefore, any measurement or captured information in the form of audio records, digital images generally need to be restored and improved. The recovering of original data from its degraded measurement is usually referred as an inverse problem, because it has not an unique solution. Normally, real-world signals bring with them some inherent features or structures that make this process of signal recovery more manageable. The use of this prior knowledge, which is called signal modeling, is what allows the development of successful methods for signal processing applications. In general, this type of applications can be described as an inverse problem (Turek (2015)).

2.2.2 | Image Pre-processing as Inverse Problem

Since an image is the result of a measurement process, we have a degraded signal that need to be reconstructed, then it can be concluded that the problems addresses by this research have in common that they are ill posed problems, that may have infinite solutions and therefore can be treated as inverse problems. In general, the inverse problems can be solved from the point of view of the Bayesian theory. This theory can contribute to an approach to the solution, since it allows to build models to deal with this kind of problems. This thesis addresses the following two problems: noise reduction and improving the segmentation. In general, these two problems can be described as an

inverse problem as follows:

$$y = x + n \tag{2.1}$$

where x is the latent or unknown image, y is the observed information (noisy, low contrast, or inhomogeneous image) and n is an additive random noise.

2.2.3 | Bayesian Inference

Bayesian inference is widely used in areas such as digital machine learning, decision theory, and of course image processing. If the information observed is y, and the latent or unknown image is x, the goal is to compute the optimal posterior probability using the Bayes rule.

$$p(x \mid y) = \frac{p(y \mid x)p(x)}{p(y)} \propto p(y \mid x)p(x) \tag{2.2}$$

where $p(y \mid x)$ is the likelihood (data, fitting error, fitting data) term, and is usually Gaussian distributed, $p(x)$ denotes the prior model, in our case the knowledge of how the image should be. According to how the prior model is chosen for an image, the problem to be solved will take different solutions. i.e. one method of solution will be more effective than another, since the prior information represents the model of how we want our final solution be, to have the result we are looking for.

2.2.4 | Sparse Representations

Sparse representations have a biologically inspired motivation. Recent researches (Olshausen and Field, 1996) (Vinje and Gallant, 2000) in neuroscience field proved that cells of primary visual cortex, in the human brain, uses sparsity for visual recognition task as extract information from outside sources, because the information of interest is always sparse compared with the whole data. For example, Figure 2.8 shows different images where the human visual system fixed the view in particular objects (red car, woman and dog, white flower, red line) that are different respect to the background, the human brain is using sparsity to disregard the rest of visual information in each image.

From the linear algebra point of view, the term sparsity refers to the number of non-zero elements in a vector. One indicator to measure the sparsity of a vector $\boldsymbol{\alpha}$ is the l_0–norm or l_0–pseudonorm, which measures the dispersion by counting the number of non-zero coefficients in the vector $\boldsymbol{\alpha}$. The l_0–norm is defined as follows:

$$\|\boldsymbol{\alpha}\|_0 = |\{i : \boldsymbol{\alpha}_i \neq 0\}| \tag{2.3}$$

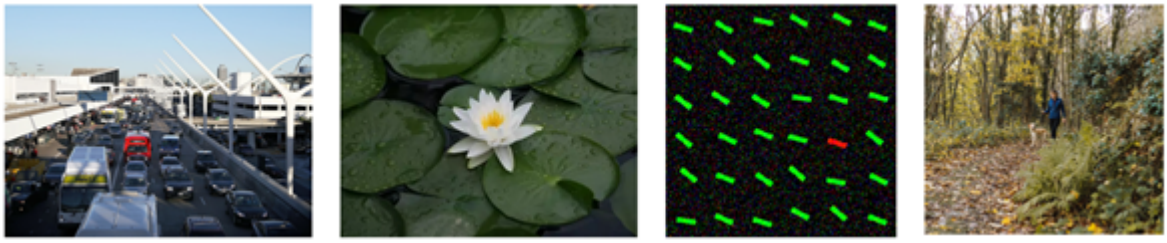

Figure 2.8: Set of images illustrating the sparsity concept.

where $|\{i : \boldsymbol{\alpha}_i \neq 0\}|$ denotes the cardinality of $\{i : \boldsymbol{\alpha}_i \neq 0\}$. Thus, a vector $\boldsymbol{\alpha} \in \mathbb{R}^n$ is sparse if $\|\boldsymbol{\alpha}\|_0 = k \ll n$. Another way to approximate sparsity is using the l_1–norm, which is the sum of the absolute value of the elements in a vector $\boldsymbol{\alpha} \in \mathbb{R}^n$, is defined as follows:

$$\|\boldsymbol{\alpha}\|_1 = \sum_{i=1}^{n} |\alpha_i| \tag{2.4}$$

Thus, a vector $\boldsymbol{\alpha} \in \mathrm{R}^n$ is sparse, if $\|\boldsymbol{\alpha}\|_1 = k \ll n$. If a signal can be characterized by a few significant terms in some domain, the signal is sparse.

2.2.5 | Dictionary Learning and Sparse Coding

Dictionary Learning is a typical example of sparse representation. It aims to find the sparse representation of a set of signals $\mathbf{Y}$ from a dictionary $\mathbf{D}$, learned from the signals themselves Zhang et al. (2015b). i.e., $\mathbf{Y} \approx \mathbf{DA}$ where $\mathbf{A}$ is the sparse coding matrix or the sparse representation of $\mathbf{Y}$.

Formally, let $\mathbf{Y} := [\mathbf{y}_1 \mathbf{y}_2 \dots \mathbf{y}_\mathrm{P}] \in \mathbb{R}^{n \times \mathrm{P}}$ be a matrix representing a set of P n-dimensional signals, the dictionary learning aims to find a dictionary $\mathbf{D} := [\mathbf{d}_1 \mathbf{d}_2 \dots \mathbf{d}_\mathrm{K}] \in \mathbb{R}^{n \times \mathrm{K}}$ and a sparse matrix $\mathbf{A} := [\boldsymbol{\alpha}_1 \boldsymbol{\alpha}_2 \dots \boldsymbol{\alpha}_\mathrm{P}] \in \mathbb{R}^{\mathrm{K} \times \mathrm{P}}$ such that $\mathbf{Y}$ can be approximated by a linear combination of the basis vectors (column vectors known as atoms) of $\mathbf{D}$ according to $\mathbf{A}$. Most of the coefficients $\alpha_{i,j}$ of $\mathbf{A}$ are zeros, or close to zero Bao and Ji (2016). Dictionary learning can typically be formulated as an optimization problem, as Equation (2.5) indicates:

$$\begin{aligned} &\min_{\mathbf{D},\mathbf{A}} \sum_{c=1}^{\mathrm{P}} \|\mathbf{y}_c - \mathbf{D}\boldsymbol{\alpha}_c\|_2^2 \\ &\text{s.t.} \\ &\|\boldsymbol{\alpha}_c\|_0 \leq \mathrm{L} \end{aligned} \tag{2.5}$$

In this formulation, $\mathbf{y}_c$ is the $c-th$ column vector (signal) of $\mathbf{Y}$, $\mathbf{D}$ is learned from the signals themselves, L is a regularization parameter, and $\boldsymbol{\alpha}_c$ is the $c-th$ column vector of $\mathbf{A}$. The term $\|\boldsymbol{\alpha}_c\|_0$ measures the sparsity of the decomposition. It can be understood as the number of coefficients different from zero in $\boldsymbol{\alpha}_c$, or sparse coefficients, to approximate the signals in $\mathbf{Y}$ as sparse as possible.

The KSVD algorithm proposed by Aharon et al. in Aharon et al. (2006a,b) allows us to obtain the optimal values of $\mathbf{D}$ and $\mathbf{A}$ in Equation (2.5).

However, when the dictionary $\mathbf{D}$ is predefined, the optimal $\mathbf{A}$ can be obtained through a process denominated sparse coding, which commonly consists of finding the coefficients in $\mathbf{A}$ by solving Equation 2.6, where Equation 2.6 is the relaxed form of Equation 2.5 and λ is a regularization parameter.

$$\min_{\boldsymbol{\alpha}_c} \sum_{c=1}^{\mathrm{P}} \|\mathbf{y}_c - \mathbf{D}\boldsymbol{\alpha}_c\|_2^2 + \lambda \|\boldsymbol{\alpha}_c\|_1 \tag{2.6}$$

2.2.6 | The K-SVD Algorithm

The K-SVD algorithm is a generalization of K-Means clustering process presented in (Aharon et al. (2006a)). Is used for dictionary learning to build a dictionary for sparse representations. The K-SVD is an iterative method that alternates between sparse coding step and updating the dictionary atoms to better fit the data. The K-SVD is described in Algorithm 2.1

Algorithm 2.1: The K-SVD dictionary learning algorithm (Aharon et al. (2006a))

Requires: Set of training signals Y
Ensure: Trained dictionary D

Initialize Dictionary: Build $D_{(0)} \in \mathbb{R}^{nxm}$
while $\|\mathbf{Y} - \mathbf{D}\boldsymbol{\alpha}\|_2^2 > \epsilon$ **do**
  Sparse Coding Stage: Use a pursuit algorithm to approximate the solution of
  $$\alpha_i' = \min_\alpha \|\mathbf{y}_i - \mathbf{D}_{k-1}\boldsymbol{\alpha}\|_2^2 \; s.t. \; \|\boldsymbol{\alpha}\|_0 \leq k_0$$
  obtaining sparse representations α_i' for $1 \leq i \leq M$. These from the matrix $\mathbf{X}_{(4)}$
  K-SVD Dictionary - Update Stage:
  for $j_0 = 1, 2, \ldots, m$ **do**
    Update the columns of the dictionary and obtain $D_{(k)}$
    Define the group of examples that use the atom α_{j0},
    $$\omega_{j0} = \{i \mid 1 \leq i \leq M, \mathbf{X}_{(k)}[j_0, i] \neq 0\}$$
    Compute the residual matrix
    $$E_{j0} = \mathbf{Y} - \sum_{j \neq j_0} \mathbf{d}_i \boldsymbol{\alpha}_j^T$$
    where x_j are the $j'th$ rows in the matrix $\mathbf{X}_{(k)}$
    Restrict E_{j0} by choosing only the colulmns corresponding to ω_{j0}, and obtain E_{j0}^R
    Apply SVD decomposition $E_{j0}^R = U\Delta V^T$
    Upadate the dictionary atom $d_{j0} = u_1$ where u_1 is the higher value of matrix U, obtained from SVD decomposition.
  end for
end while
return D

2.2.7 | Numerical Methods for L1 Norm Minimization

Although the l_0–norm is the real measure of sparsity of a vector, the solution of 2.5 is a NP-hard problem whose optimal solution can only be reached by a brute force algorithm. As alternative, the l_1–norm is used as approximation, and can be used as a relaxed form of 2.5. The algorithms presented in this research use the l_1–norm as regularization term. There is a wide range of numerical methods to solve problems that involve the l_1–norm, some of them are:

- Basis Pursuit Denoising Lasso type algorithms, Least Angle Regression (LARS).
- Constraint Optimization
  - Gradient Projection Sparse Reconstruction (GPRS)
  - Interior Point Method Based Sparse Representation
  - Alternated Direction Method (ADM) Sparse Representation.

- Proximity Algorithms
  - Proximal Gradient Soft Thresholding or Shrinkage Operator
  - Iterative Shrinkage Thresholding Algorithm (ISTA)
  - Fast Iterative Shrinkage Thresholding Algorithm (FISTA)
  - Augmented Lagrange Multiplier (ALM)
  - Split Bregman Method.

In this thesis it is used the LARS algorithm strategy for Sparse Coding.

Algorithm 2.2: The Least Angle Regression (LARS) Algorithm (Efron et al. (2004))

Input: $m \times n$ matrix $\mathbf{A}, \mathbf{y}$

1: **Initialize:**
$\mathbf{x} = 0, S = supp(x) = \boldsymbol{\phi}, \mathbf{r} = \mathbf{y} - \mathbf{A}\mathbf{x} = \mathbf{y}$

2: **Select first variable:**
find the predictor (column in $\mathbf{A}$) most correlated with residual $\mathbf{r}$:
$i = \arg\max_i \mathbf{a}_i^T \mathbf{r}$
$\hat{x}_i = \max_i \mathbf{a}_i^T \mathbf{r}$
$S \leftarrow S \cup \{i\}$ //update the support

3: Move the coefficient x_i from 0 towards its least-squares coefficient $\hat{x}_{i^k}$, updating the residual $\mathbf{r}$ along the way, until some other predictor $\mathbf{a}_j$ has as much correlation with the current residual as does $\mathbf{a}_j$; then add it to the support: $S \leftarrow S \cup \{j\}$

4: Move x_i and x_j in the direction defined by their joint least-squares coefficient:

$$\delta_k = (\mathbf{A}_{S^k}^T \mathbf{A}_{S^k})^{-1} \mathbf{A}_{S^k}^T \mathbf{r}$$

of the current residual on the current support set S, until some other predictor $\mathbf{a}_k$ has as much correlation with the current residual; then add it to the support: $S \leftarrow S \cup \{k\}$.

5: Continue adding predictors for $\min(m-1, n)$ steps, until full OLS solution is obtained. if $n < m$, all predictors are now in the model.

2.2.8 | Least Angle Regression for Lasso - LARS Algorithm

LARS proposed by (Efron et al. (2004)) is a model selection method for linear regression in high dimensional data, which has a fast convergence. At each step, it finds the predictor most correlated with the response. When there are multiple predictors having equal correlation, instead of continuing along the same predictor, it proceeds in a direction equiangular between the predictors. LARS is summarized in Algorithm 2.2

2.2.9 | The Non-Local Means Algorithm

The Non-Local Means (NLM) algorithm, is a method for denoising images which is based on the concept of self-similarity. This refers to the fact that some areas of a digital image are similar, regardless of whether those areas are neighboring or not. Figure 2.9 illustrates the concept. The NLM reduces the image noise by computing filtered pixel as the average of all similar pixel in the image, weighted by the level of similarity of the surrounding pixels to the reference pixel.

Many variants of the NLM have been presented. A complete review can be found in Fan et al. (2019). A complete review on variants for MR images filtering can be found in Bhujle and Vadavadagi (2019). The original NLM has two variants, the pixelwise implementation (PII) and the patchwise implementation (PAI) Buades et al. (2011). The PII is according to Equation 2.7.

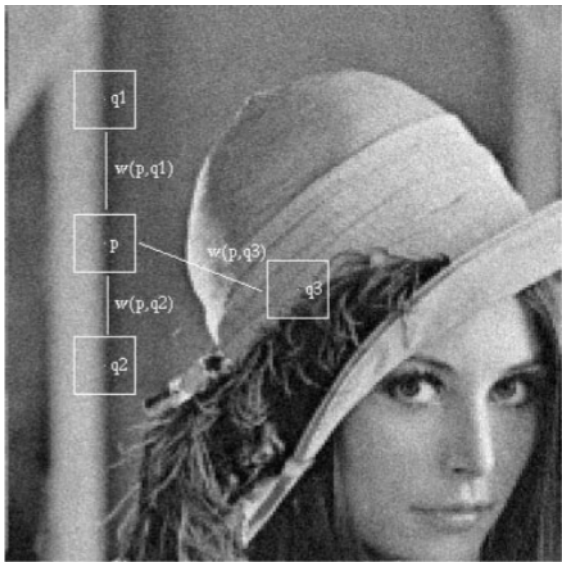

Figure 2.9: Illustration of the self-similarity concept that the NLM algorithm exploits (Taken from Buades et al. (2005a))

$$\hat{u}_i(p) = \frac{1}{C(p)} \sum_{q \in B(p,r)} u_i(q) w(p,q), \quad C(p) = \sum_{q \in B(p,r)} w(p,q) \tag{2.7}$$

where u_i is the $i-th$ pixel of image u, $B(p,r)$ is a neighborhood centered at p and $w(p,q)$, computed according to Equation 2.8, is a weighting factor dependent on the Euclidean distance d^2 between the neighborhoods $B(p,r)$ and $B(q,r)$, which is computed according to Equation 2.9.

$$w(p,q) = e^{-\frac{max(d^2 - 2\sigma^2, 0.0)}{h^2}} \tag{2.8}$$

$$d^2 = d^2(B(p,f), B(q,f)) = \frac{1}{3(2f+1)^2} \sum_{i=1}^{3} \sum_{j \in B(0,f)} (u_i(p+j) - u_i(q+j))^2 \tag{2.9}$$

The PAI is according to Equation 2.10.

$$\hat{B}_i = \frac{1}{C} \sum_{Q=Q(q,f) \in B(p,r)} u_i(Q) w(B,Q), \quad \sum_{Q=Q(q,f) \in B(p,r)} w(B,Q) \tag{2.10}$$

where $B(p,r)$ is a neighborhood centered at p. $w(B(p,f), B(q,f)$ has the same formulation than in the PII. The denoised version of a pixel in the PAI is according to Equation 2.11

$$\hat{u}_i(p) = \frac{1}{N^2} \sum_{Q=Q(q,f) | q \in B(p,f)} \hat{Q}_i(p) \tag{2.11}$$

2.2.10 | SVD

Singular Value Decomposition (SVD) is a matrix factorization that allows for the decomposition of a given matrix $\mathbf{X}$ into three new matrices $\mathbf{U}$, $\mathbf{\Sigma}$ and $\mathbf{V}$ so that $\mathbf{X} = \mathbf{U}\mathbf{\Sigma}\mathbf{V}^\intercal$, where $\mathbf{U}$ and $\mathbf{V}$ are orthogonal matrices, and Σ is a diagonal matrix whose diagonal entries σ_i are the singular values of $\mathbf{X}$.

The columns vectors of $\mathbf{U}$ are called the left singular vectors, and the columns vectors of $\mathbf{V}$ are called the right singular vectors. This vectors have some interesting properties. For example, the left singular vectors are the eigenvectors of $\mathbf{X}\mathbf{X}^T$, whereas the right singular vectors are the eigenvectors of $\mathbf{X}^T\mathbf{X}$. It is also met that $\mathbf{X}\mathbf{X}^T\mathbf{U} = \mathbf{U}\mathbf{S}^2$ and $\mathbf{X}^\intercal\mathbf{X}\mathbf{V} = \mathbf{V}\mathbf{S}^2$. Other important properties of the SVD is that the singular values σ_i of $\mathbf{X}$ are greater or equal to zero, and the rank of $\mathbf{X}$ is equal to the number of singular values different from zero.

Alternatively, the SVD can be expressed in summation form as, $\mathbf{X} = \sum_{i=1}^{n} s_i \mathbf{u}_i \mathbf{v}_i$, which can be understood as a summation of rank 1 matrices. This form of the SVD is useful when trying to approximate a matrix from another one of low rank, and has many applications. One of the most important in image processing is the low rank approximation for image filtering. This will be addressed in chapter 3.

2.3 | Summary

This chapter presented both the physiological and the computer sciences bases of the techniques proposed in the remaining of this thesis. Next chapters will address two main problems and their solution approaches, towards the discovery of brain biomarkers of the offending behavior in young people. This problems are: 1) Denoising MR images while keeping fine details avoiding both blurring and residual noise. This is crucial for subsequent segmentation process. 2) Improve the segmentation of brain structures. This is of vital importance when it comes to finding small variations in brain structures, which are expected to determine behavioral aspects of young offenders.

3

MRI Denosing

Magnetic Resonance (MR) Imaging is a diagnostic technique that produces noisy images, which must be filtered before processing to prevent diagnostic errors. However, filtering the noise while keeping fine details is a difficult task. This chapter presents a method, based on sparse representations and singular value decomposition (SVD), for non-locally denoising MR images. This method prevents blurring, artifacts, and residual noise. It is composed of three stages. The first stage divides the image into sub-volumes, to obtain its sparse representation, by using the KSVD algorithm. Then, the global influence of the dictionary atoms is computed to upgrade the dictionary and obtain a better reconstruction of the sub-volumes. In the second stage, based on the sparse representation, the noise-free sub-volume is estimated using a non-local approach and SVD. The noise-free voxel is reconstructed by aggregating the overlapped voxels according to the rarity of the sub-volumes it belongs, which is computed from the global influence of the atoms. The third stage repeats the process using a different sub-volume size for producing a new filtered image, which is averaged with the previously filtered images. The results provided show that this method outperforms several state-of-the-art methods in both simulated and real data.

3.1 | Introduction

MR Imaging is a useful diagnostic technique that produces high-resolution images that are affected by different sources of quality deterioration due to the inherent limitations in the hardware, scanning time, movements of patients, and, one of the most important, noise. The presence of noise is not only a visual problem but also may interfere during the analysis and segmentation tasks (Aja-Fernandez and Tristan-Vega (2013)).

A study of errors in radiology conducted by Donald L. Renfrew (Renfrew et al. (1992)) found that errors usually involved limitations in imaging technique and acquisition of inaccurate or incomplete clinical history, among others. Previous research found that 69.23% were perceptual errors, and 6.4% of errors were due to poor image quality (Fitzgerald (2001)). This research suggests the importance of guaranteeing the image quality in order to obtain better results in image segmentation and analysis for preventing errors. Despite the advance in MR imaging acquisition technology, which allowed the increment in the signal-to-noise ratio, the acquisition speed, and the resolution, MR images are still affected by noise (Mohan et al. (2014)), therefore the filtering of MR images continues being an active research area (Benou et al. (2017); Chang et al. (2018); Kang et al. (2018); Manjón et al. (2015); Maosong et al. (2019); Veraart et al. (2016)).

The raw captured data of an MR image are complex-valued, i.e., the image can be decomposed in amplitude and phase or real and imaginary images (Gudbjartsson and Patz (1995)). Both real and imaginary images are affected by additive Gaussian noise. However, magnitude MR images, which are obtained by computing the magnitude from the real and imaginary images, through a nonlinear mapping, are affected by noise that does not follow a Gaussian distribution; instead, it follows a Rician distribution.

According to (Foi (2011)), Rician distribution has two parameters, the noise-free magnitude of the data, which is unknown, and the standard deviation of the noise that affects the real and imaginary images. Estimating the magnitude is a difficult task, because the standard deviation of Rician noise in magnitude MR images depends on the magnitude of the data itself, and the expectation of the noisy magnitude differs from the noise-free magnitude by a nonlinear function of the noise standard-deviation and of the noise-free magnitude. (Foi (2011)) proposed a method, called Variance-Stabilization Transformation (VST), which enables methods designed for filtering additive Gaussian noise, to deal with MR images.

Some works focused on improving the MR imaging results during the scanning process (Hong et al. (2019); Zhou et al. (2017)). However, when no previous treatment has been performed, we must deal with issues in the captured image. Hence, many previous works proposed methods for denoising MR images, most of them are adaptations of approaches for filtering 2D images, such as the widely known Non-Local Means (NLM) filtering, proposed by Buades in 2005 (Buades et al. (2005a)). This method was the first approach in considering the self-similarity of the image for filtering noise. This method computes the pixel value as a non-local weighted average of all pixels in the image; the weights depend on the similarity between the patches around the pixels. This method is the basis of many proposed variants; however, blurring and blocking artifacts still affect the denoised image (Wang et al. (2018a)).

Coupé (Coupé et al. (2008)) and Manjón (Manjón et al. (2008)) introduced the first adaptations of the NLM for denoising MR Images in 2008. The proposal of (Coupé et al. (2008)) focused on an efficient implementation that reduces the dependency on parameters by automatically tuning the smoothing parameter and selecting the most relevant voxels. Similarly, the proposal of (Manjón et al. (2008)) focused on finding the optimal parameters for denoising MR magnitude images.

Due to the high computational complexity of NLM-based methods, some works focused on efficient implementations for processing MR images. (Hu et al. (2016)) proposed a variant called SNLM. The proposed algorithm drastically reduces the running time to 1/20 of other NLM's variants by randomly selecting a small subset of voxels. They introduced an optimal sampling pattern for further improvement. However, the sampling ratio needs to be high for the denoising results to be comparable to NLM. (Klosowski and Frahm (2017)) presented an efficient implementation for real-time MR image processing, which improves details preservation. The improvement was carried out by introducing a simple weighting function based on a compact support kernel. The reported results are comparable to the block-matching three-dimensional filter. Manjón proposed to use NLM along with sparseness (Manjón et al. (2012)), and NLM along with sparseness plus principal components analysis (PCA) (Manjón et al. (2015)) for denoising MR images. The last method estimates the noise level of the image, which is assumed as white noise and filters it using non-local PCA. However, this is not satisfied when using Fourier or compressed sensing; therefore, the method cannot be applied when this assumption is not met.

The SVD is also a widely recognized technique that has been used for image denoising (Hou (2003); Malini and Moni (2015); Wang et al. (2018b)). (Rajwade et al. (2012)) successfully used the higher order singular value decomposition (HOSVD) for filtering natural images, although this technique require complex criteria, which involve solving optimization models, to establish the low rank approximation for filtering noise. In addition, the HOSVD suffers from artifacts when applies on homogeneous regions (Zhang et al. (2017)). The work of Rawade was adapted for (Zhang et al. (2015a)) for filtering MR images. This adaptation improved the HOSVD, by adding an additional recursive stage which in general terms, repeats the HOSVD for filtering the noisy image resulting from the partial re-incorporation of the residual noise into the denoised image produced by the first stage. (Zhang et al. (2017)) also adapted the HOSVD for filtering diffusion-weighted images. Several other works used the SVD a long with NLM for filtering MR images (Kong et al. (2018)) and natural images (Dong et al. (2008, 2013))

(Dabov et al. (2006)) proposed one of the most important methods in state-of-the-art image denoising, "Image denoising with block-matching and 3D filtering" (BM3D).

This method exploits the self-similarity in conjunction with filtering in the transform domain, and has a variant for direct processing of volumetric data, denominated BM4D (Maggioni et al. (2013)), which is still considered a state-of-the-art algorithm (Xu et al. (2019)). Like the BM3D, the BM4D in the first stage applies thresholding for gathering similar cubes in a 4D data structure and removes noise through a 4D transform. The second stage restores the details by using collaborative filtering. The stacked 3D cube voxels in the 4D structure lead to difficulties in removing noise in the beginning and at the end of the bands of hyperspectral image (Xu et al. (2019)). In addition, when the noise level is high, the block-matching distance does not allow the program to obtain enough similar blocks; therefore, the denoising reduces its performance, and some artifacts appear.

Another important approach that attracted attention in image processing is sparse representation. It has been used for image labeling (Tao et al. (2016)), image segmentation and classification (Moradi and Mahdavi-Amiri (2019)), image inpainting (Li et al. (2014)) and image denoising (Elad and Aharon (2006); Khedr et al. (2012); Wang et al. (2017)), among others. This approach was also used for denoising MR images. Recently, (Yuan (2019)) proposed an efficient implementation, based on an improved Split-Bregman algorithm, for filtering MR images using a sparse tensor model. (Zhang et al. (2019)) use clustering to gather similar patches and filter them using a sparse model, which uses sparse gradient priors to exploit the image low-rank properties. (Kang et al. (2018)) use a sparse representation-based model for both filtering Rician noise and deblurring MR images. The model incorporates a regularization term to preserve small details and repeated patterns while using a non-convex total variation term for preserving edges. (Li et al. (2018)) presented an improved dictionary learning model for medical image fusion denoising. By incorporating a low rank and sparse regularization term, into the sparse model, this proposal can remove noise while preserving textural details.

Further contributions, such as those proposed by (Veraart et al. (2016)), use random matrix theory for filtering typical fluctuations originated from thermal noise in diffusion-weighted MR images. (Phophalia and Mitra (2017)) use Kernel principal component analysis (KPCA) and Rough Set Theory (RST) for denoising volumetric MR data. RST is used to group similar voxels forming basis vectors, which are projected into a kernel space for performing PCA where the linear separation is possible, and the filtering is carried out.

(Baselice et al. (2017)) introduced an approach from the complex domain under the argument that, in this domain, the filtering has the advantage of a simplified statistical model of the signal with Gaussian nature and zero mean. This method is an advantage

over methods that operate in the amplitude domain where the noise model may not comply with being Gaussian.

Although recently some authors have focused on accurately estimating the noise (Aja-Fernández et al. (2015)) and correcting the bias produced by the aggregation of non-stationary distributed MR images samples, before trying to remove the noise (Liu et al. (2019); Pieciak et al. (2018)), new research focused on denoising MR images by applying machine learning-based techniques. (Chang et al. (2018)) presented an extension of the bilateral filter, which adapts to voxel intensity variations by including an intensity similarity function and automates the calculations of denoising parameters values, by extracting descriptors of texture issues, through an ensemble classifier of support vector machines and artificial neural networks. Other works use deep networks for exploring the similarity between neighboring slices in order to reduce the over-smoothing (Maosong et al. (2019)) and for denoising Dynamic contrast-enhanced MR images (Benou et al. (2017)). (Zhang et al. (2017)) proposed a feed-forward denoising convolutional neural networks (DnCNNs) that took the batch normalization and residual learning architecture to denoising images, reducing the training process and improving the denoising performance. Based on the DnCNN, (Jiang et al. (2018)) proposed a denoising method for brain MR images. They proposed a multichannel version of the DnCNN for dealing with 3D images, improving filtering performance in various noise levels. (Kidoh et al. (2019)) also proposed a deep learning-based reconstruction method for denoising brain MR images. Their method reduces image noise while preserving image quality outperforming the DnCNN.

This chapter presents a filter for denoising MR magnitude images. Unlike some of the works presented based on NLM (Coupé et al. (2008); Hu et al. (2016); Klosowski and Frahm (2017); Manjón et al. (2008)), or SVD (Zhang et al. (2017, 2015a)), or sparse representations (Kang et al. (2018); Li et al. (2018); Yuan (2019); Zhang et al. (2019)), or some combination of these (Dong et al. (2008, 2013); Kong et al. (2018); Manjón et al. (2012); Zhang et al. (2019)), this is a novel method, which does not propose a new sparse model but fully exploits one of the most typical representative examples of sparse representation, dictionary learning. Dictionary learning is used for both orchestrating the non-local and the SVD approach efficiently, and for outperforming the representation of fine details of the image, by (1) enhancing the learned dictionary and determining the weighting coefficients of the patches, according to the global influence of the dictionary atoms, for filtering noise by aggregation, while avoiding blurring and keeping fine details. (2) Establishing the self-similarity of the image efficiently, in a clean space by analyzing the dictionary atoms and the sparse coding matrix, which allows to accurately recover similar patches throughout the volume, without resorting to the exhaus-

tive comparison of each patch in the volume, because the self-similarity can be inferred from the sparse coding matrix. Thus, it is minimized the appearance of artifacts. (3) Unlike (Rajwade et al. (2012); Zhang et al. (2017, 2015a)), which establishes complex criteria that use optimization models to determine the best low-rank approximation for filtering noise, this method, based on the similar patches identified from the sparse representation, determines simply and efficiently, the best low-rank approximation according to the estimated noise level of the image, thus reducing the remaining noise in the denoised image.

The rest of this chapter is organized as follows: Section 3.2 presents the proposed method for MR images denoising. Section 3.3 presents the results and discussion. Finally, Section 3.4 presents the conclusions of this chapter.

3.2 | Non-local MRI Denoising

The typical procedure for denoising images, via sparse representations, consist of decompose the noisy image I into full overlapped $n \times n$ patches to convert them into signals and filter them using a model, such as that in Equation (2.5). This procedure can be extended in the case of MR images for processing the whole volume; however, as mentioned before, noise in MR images follows a Rician distribution, which is non-additive but dependent on the data. To handle this type of noise, and to get an accurate estimation of its stabilized standard deviation γ, we apply the variance stabilization transformation (VST) proposed by Foi (Foi (2011)) before processing the noisy volume V, which give us V_{VST}. Then, we divide the volume V_{VST} into full overlapped sub-volumes of $n \times n \times n$. Each sub-volume is converted into a signal $\mathbf{y}_c \in \mathbb{R}^{n^3 \times 1}$ to conform the matrix $\mathbf{Y} := [\mathbf{y}_1 \mathbf{y}_2 \dots \mathbf{y}_P] \in \mathbb{R}^{n^3 \times P}$, where P is the number of signals. Now $\mathbf{Y}$ can be reconstructed solving Equation (2.5) by using the KSVD algorithm.

However, the reconstruction given by **DA** leads to the recovery of an MR image suffering from blurring effect, artifacts, and that keeps some residual noise, as shown in Figure 3.1. To overcome this, we focus on three important issues of the sparse representations: the weighting of its atoms, the self-similarity that emerges from these, and the scales that these representations can handle. The three steps that make up our method address each of the issues above. Figure 3.2 illustrates the steps of our method.

3.2.1 | Weighting the Dictionary Atoms

In digital image processing, there exist several approaches for denoising images corrupted by noise; one of them is filtering in the spatial domain using masks. The co-

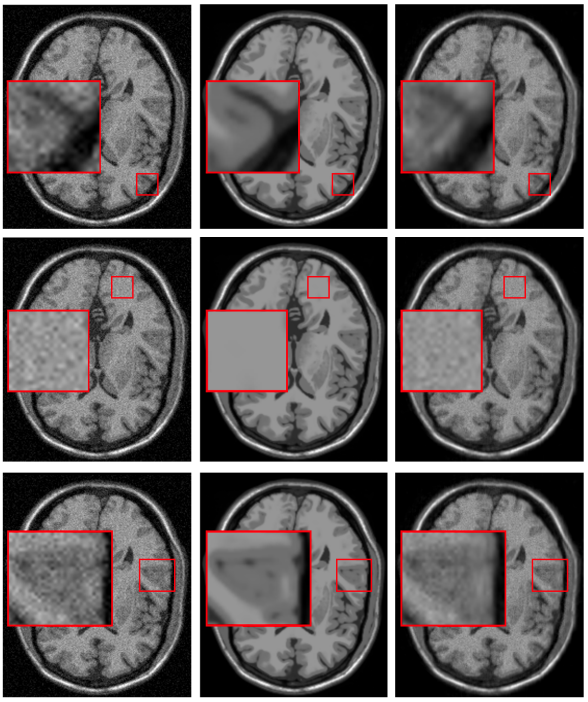

Figure 3.1: Issues of the KSVD filtering. Columns from left to right correspond to a phantom noise-free image added with 5% Rician noise, original phantom noise-free image, and image denoised by the KSVD. The third column from top to down corresponds to artifacts, residual noise, and blurring issues that the KSVD produces.

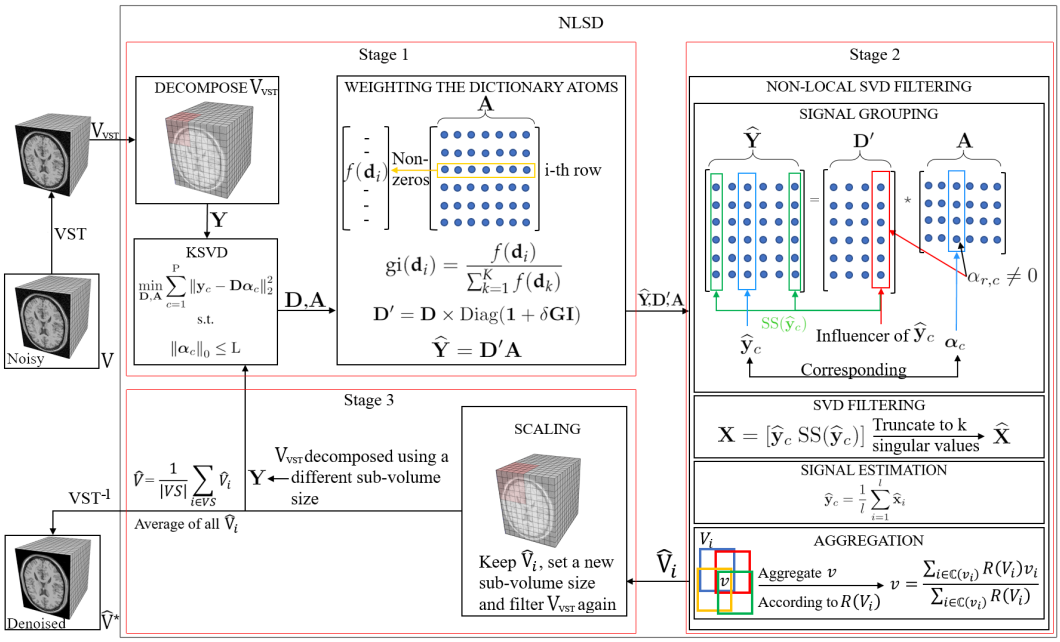

Figure 3.2: Block diagram illustrating the three steps of the proposed method.

efficients of the spatial masks are set depending on both the noise level and the type of noise. For Gaussian noise, the coefficients are weighting factors set according to the distance to the center of the mask (Gonzalez and Woods (2017)). The central coefficient gives the weight of the pixel under analysis during the denoising process. The greater this coefficient is, the more similar the filtered pixel will be to the original. This similarity implies that this coefficient can control the blurring produced by the smoothing process. We apply this reasoning to the dictionary learning, but instead of weighting the pixels of the image, we weight the atoms.

For denoising the image while keeping fine details, which is essential in MR images, this new approach proposes weighting the atoms according to its global influence. We define the global influence of a dictionary atom as the probability that such an atom appears as a linear combination in the reconstruction of a signal. i.e. For example, after finding the optimal $\mathbf{A}$ in Equation (2.5), the global influence of an atoms is calculated as the number of non-zero coefficients corresponding to that atom in $\mathbf{A}$. Formally, the global influence gi of an atom $\mathbf{d}_c$ of $\mathbf{D}$ is equal to the probability that $\mathbf{d}_c$ affects a signal, as Equation (3.1) indicates.

$$\mathrm{gi}(\mathbf{d}_c) = \frac{f(\mathbf{d}_c)}{\sum_{k=1}^{K} f(\mathbf{d}_k)} \tag{3.1}$$

$$f(\mathbf{d}_c) = \sum_{p=1}^{\mathrm{P}} \mathrm{g}(\alpha_{c,p}) \tag{3.2}$$

$$\mathrm{g}(\alpha_{c,p}) = \begin{cases} 1, & \text{if } \alpha_{c,p} \neq 0 \\ 0, & \text{otherwise} \end{cases} \tag{3.3}$$

where $\alpha_{c,p}$ is the element entry of the c-th row and the $p-th$ column of the matrix $\mathbf{A}$. The global influence is used to reinforce the effect of the more frequent atoms in the signals, to reduce the blurring caused by the average of sub-volumes during the aggregation. In the case of brain MR images, this global influence will be used for reinforcing atoms that represent common patterns found in these images, like the edges between brain structures, and therefore, for preventing the blurring in such patterns. Equation (4.3) updates the dictionary for reinforcing the atoms according to their global influence.

$$\mathbf{D}' = \mathbf{D} \times \mathrm{Diag}(\mathbf{1} + \delta \mathbf{GI}) \tag{3.4}$$

where $\mathbf{GI} := [\mathrm{gi}(\mathbf{d}_1), \mathrm{gi}(\mathbf{d}_2), \ldots, \mathrm{gi}(\mathbf{d}_{\mathrm{K}})]$ is a vector containing the global influence of all atoms, δ is a constant for controlling the influence ($\delta = 8$, which was experimentally obtained by numerical tests). $\mathbf{1}$ is a vector of ones, and $\mathrm{Diag}(\cdot)$ is a $\mathrm{K} \times \mathrm{K}$ diagonal matrix

with diagonal element entries equal to $\mathbf{1} + \delta\mathbf{GI}$. Now $\widehat{\mathbf{Y}}$, a noise-free reconstruction of $\mathbf{Y}$ that keeps fine details, is computed using Equation (4.4).

$$\widehat{\mathbf{Y}} = \mathbf{D}'\mathbf{A} \tag{3.5}$$

Although $\widehat{\mathbf{Y}}$, improves the representation of fine details, there is still some residual noise that can be eliminated, taking advantage of the self-similarity of the image, which can be easily examined from the sparse representation given by $\mathbf{D}'$ and $\mathbf{A}$. This will be addressed below.

3.2.2 | Non-Local SVD Filtering

3.2.2.1 | Signal Grouping

Non-local filtering overcomes local filtering (Buades et al. (2005b); Raghuvanshi et al. (2012)); however, it is dependent on parameters such as search windows and thresholds (Manjón et al. (2008)). Also, it is affected by searching for similar patches in a noisy space, which may affect the patch grouping and therefore lead to a bad estimation of the pixel. Instead, we search for similar signals in the clean space given by $\mathbf{D}'\mathbf{A}$ without searching windows, because the sparse representation allows examining the self-similarity of the image through the dictionary atoms.

For performing non-local filtering based on sparse representations, we rely on the fact that similar signals admit similar sparse representations (Ramirez et al. (2010); Sprechmann and Sapiro (2010)); hence, to find similar signals to a given signal $\widehat{\mathbf{y}}_c$, we starting determining which atoms make up $\widehat{\mathbf{y}}_c$ by using Equation (3.6).

$$\mathbb{I}(\widehat{\mathbf{y}}_c) := \{r : \alpha_{r,c} \neq 0,\ r = 1, 2, \ldots, \mathrm{K}\} \tag{3.6}$$

where K is the number of atoms in $\mathbf{D}'$ (number of rows of $\mathbf{A}$). $\mathbb{I}$ denotes the set of influencer atoms of $\widehat{\mathbf{y}}_c$ i.e., the set of atoms belonging to $\mathbf{D}'$ that are linearly combined according to $\boldsymbol{\alpha}_c$ for generating $\widehat{\mathbf{y}}_c$ (Figure 3.2 encloses an influencer atom of $\widehat{\mathbf{y}}_c$ in a red rectangle in the SIGNAL GROUPING box). Then, we search for the most influencer atoms of $\widehat{\mathbf{Y}}$ as Equation (3.7) indicates.

$$\mathbb{M}(\widehat{\mathbf{Y}}) := \{(r, c) : |\alpha_{r,c}| = \max(|\boldsymbol{\alpha}_c|),\ c = 1, 2, \ldots, \mathrm{P}\} \tag{3.7}$$

where $|\boldsymbol{\alpha}_c| := [|\alpha_{1,c}|, |\alpha_{2,c}|, \cdots, |\alpha_{\mathrm{K},c}|]$ is the vector $\boldsymbol{\alpha}_c$ with its components in absolut value, $\max(|\boldsymbol{\alpha}_c|)$ denotes the largest component of $|\boldsymbol{\alpha}_c|$, and P is the number of signals in $\widehat{\mathbf{Y}}$. $\mathbb{M}$ denotes the set of ordered pairs (r, c) meaning that $\mathbf{d}_r$ of $\mathbf{D}'$ is the greatest

influencer atom of the signal $\widehat{\mathbf{y}}_c$ of $\widehat{\mathbf{Y}}$. From the two previous sets, the set $\text{CSS}(\widehat{\mathbf{y}}_c)$ of candidates to similar signals of $\widehat{\mathbf{y}}_c$ is defined according to Equation (3.8).

$$\text{CSS}(\widehat{\mathbf{y}}_c) = \left\{ \widehat{\mathbf{y}}_j : (r, j) \in \mathbb{M}(\widehat{\mathbf{Y}}) \wedge r \in \mathbb{I}(\widehat{\mathbf{y}}_c) \right\} \tag{3.8}$$

where $\text{CSS}(\widehat{\mathbf{y}}_c)$ contains all the signals $\widehat{\mathbf{y}}_j$ of $\widehat{\mathbf{Y}}$ whose greatest influencer atom belongs to $\mathbb{I}(\widehat{\mathbf{y}}_c)$. Figure 3.3a shows an example of a given reference signal $\widehat{\mathbf{y}}_c$ in a MR image. Figure 3.3b shows the set of candidates to similar signals $\text{CSS}(\widehat{\mathbf{y}}_c)$ from the given reference signal of Figure 3.3a, obtained using Equation (3.8). For obtaining the set of similar signals of $\widehat{\mathbf{y}}_c$ denoted by $\text{SS}(\widehat{\mathbf{y}}_c)$ (signals pointed out by green arrows in Figure 3.2), and additionally, to get a better filtering performance in visual terms, we rely on the fact that the human eye is relatively less sensitive to dark signals than to bright ones (Kimpe and Tuytschaever (2007)). Therefore, we do not define a fixed threshold for selecting similar signals, but a variable one, dependent on both the magnitude of the reference signal and the noise level of the image. This variable threshold will allow reference signals with a large magnitude admit less difference to similar signals than the dark ones; in addition, will allow increasing the number of similar signals for MR images with high noise levels to get a better estimation of the noise-free reference signal. Hence, we define $\text{SS}(\widehat{\mathbf{y}}_c)$ according to Equation (3.9).

$$\text{SS}(\widehat{\mathbf{y}}_c) := \left\{ \widehat{\mathbf{y}}_j \in \text{CSS}(\widehat{\mathbf{y}}_c) : \frac{\left\| \widehat{\mathbf{y}}_j - \widehat{\mathbf{y}}_c \right\|}{\|\widehat{\mathbf{y}}_c\|} \leq \left(b - a \frac{\|\widehat{\mathbf{y}}_c\|}{\|\mathbf{1}_{n^3}\|} \right) (1 + \gamma) \right\} \tag{3.9}$$

where b is the upper limit and $b - a$ is the lower limit, respectively, of the interval containing the variable threshold that establishes the relative similarity between the signals ($a = 0.06$ and $b = 0.18$, which were experimentally obtained by numerical tests). $\mathbf{1}_{n^3}$ is an n^3-dimensional vector of ones (with n being the edge of the sub-volume). γ is the estimated noise level. The left side of the inequality in Equation (3.9) is undefined when $\|\widehat{\mathbf{y}}_c\| = 0$. Hence, we convert it into $\left\|\widehat{\mathbf{y}}_j\right\|$ when $\|\widehat{\mathbf{y}}_c\| \leq 10^{-6}$. Please note that a bright signal (large magnitude signal) admits less difference in their similar signals than a dark one because of the magnitude of the threshold $b - a \frac{\|\widehat{\mathbf{y}}_c\|}{\|\mathbf{1}_{n^3}\|}$ decreases as long as $\|\widehat{\mathbf{y}}_c\|$ increases. Also note that, although the threshold is inversely proportional to the magnitude of the reference signal in the interval $[b - a, b]$, this threshold will be greater for signals of high noise level images than for signals of low noise level images, because of the term $(1 + \gamma)$. We can increase the threshold for collecting similar signals on high noise level images without significantly affect the subsequent estimation of the noise-free reference signal, because we search for similar signals in the clean space given by the sparse representation.

Figure 3.3c shows the set of similar signals $\mathrm{SS}(\widehat{\mathbf{y}}_c)$ of the reference signal given in Figure 3.3a obtained after applying Equation (3.9) to $\mathrm{CSS}(\widehat{\mathbf{y}}_c)$. The red arrows in Figure 3.3c point out similar signals away from the reference signal, demonstrating that the sparse representation allows us to locate similar signals throughout the MR image, without examining the entire volume. It also shows that our method can locate signals in a space not restricted to search windows. Therefore we can collect a larger number of similar signals (with respect to methods that use such windows), which improves the denoising.

Now, the set $\mathrm{SS}(\widehat{\mathbf{y}}_c)$ can be used for estimating $\widehat{\mathbf{y}}_c$ in a non-local way; however, as was mentioned before, all the signals in $\widehat{\mathbf{Y}}$ keep some residual noise, and a better estimation could be carried out by a cleaner version of $\mathrm{SS}(\widehat{\mathbf{y}}_c)$.

3.2.2.2 | Efficient SVD Filtering

A known way for reducing the noise of an image is by analyzing its SVD decomposition. Chapter 2 presented the summation form of this decomposition, which is useful to isolate the noisy components of the image. As we know, in summation form, given a noisy image $\mathbf{X}$ its SVD decomposition $\mathbf{X} = \sum_{i=1}^{n} s_i \mathbf{u}_i \mathbf{v}_i$ can be understood as a weighted sum of component images, where the Eigen-images corresponding to the smallest singular values are commonly associated with noise (Sadek (2012)). Therefore, a vital issue for denoising based on SVD is determining what singular values correspond to the component noisy images. According to the Eckart–Young–Mirsky theorem (Eckart and Young (1936)), given a matrix $\mathbf{X} = \mathbf{U}\mathbf{\Sigma}\mathbf{V}^\intercal$ then for any rank-k matrix $\widehat{\mathbf{X}}$, it is fulfilled that:

$$\left\|\mathbf{X} - \widehat{\mathbf{X}}\right\|_F = \|\mathbf{X} - \mathbf{U}\mathbf{\Sigma}_k\mathbf{V}^\intercal\|_F \geq \sqrt{\sum_{i=k+1}^{n} \sigma_i^2} \tag{3.10}$$

where $\|\cdot\|_F$ is the Frobenius norm, $\mathbf{\Sigma}_k$ is the $\mathbf{\Sigma}$ matrix of the SVD decomposition of $\mathbf{X}$ with the singular values $\sigma_{k+1} = \sigma_{k+2} = \ldots = \sigma_n = 0$. By squaring Equations (3.10) and (3.11) is obtained.

$$\left\|\mathbf{X} - \widehat{\mathbf{X}}\right\|_F^2 = \|\mathbf{X} - \mathbf{U}\mathbf{\Sigma}_k\mathbf{V}^\intercal\|_F^2 \geq \sum_{i=k+1}^{n} \sigma_i^2 \tag{3.11}$$

Taking the right side of the inequality and matching γ^2, where γ is the stabilized standard deviation of noise (estimated according to Foi (2011)), we have:

$$\sum_{i=k+1}^{n} \sigma_i^2 \geq \gamma^2 \tag{3.12}$$

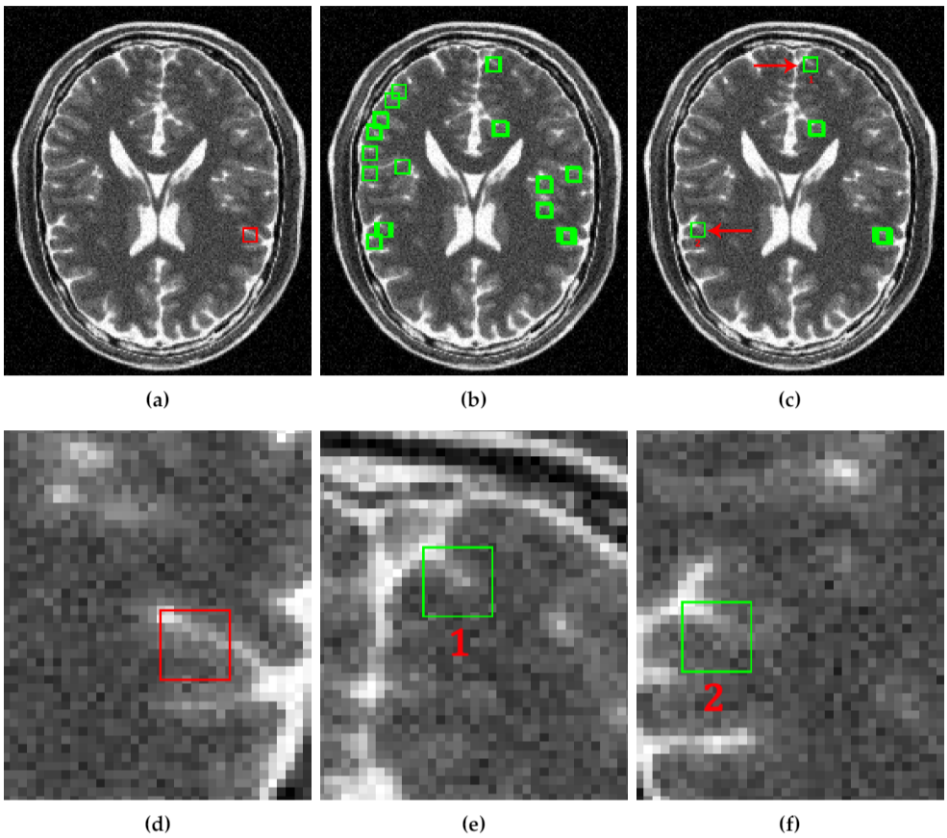

Figure 3.3: Example of a reference signal and its corresponding sets of Candidates to similar signals CSS, and Similar signals SS. (**a**) Example of a reference signal. (**b**) Candidates to similar signals of the reference signal in (**a**). (**c**) Similar signals of the reference signal in (B). (**d**) Zoom-in of the reference signal in (**a**). (**e**,**f**) Zoom-in of the similar signals 1 and 2, demonstrating that our method can locate similar signals away from the reference signal.

Equation (3.12) tells us that, when the sum of squares of the $n-k$ less significant singular values of $\mathbf{X}$ is equal or greater than γ^2, we have the best k for filtering the noise of $\mathbf{X}$. These $n-k$ less significant singular values correspond to the noisy component images (noisy component volumes in our case), and therefore, using only the first k more significant singular values we discard such component noisy images of $\mathbf{X}$.

Now, for filtering the residual noise of both $\widehat{\mathbf{y}}_c$ and $\mathrm{SS}(\widehat{\mathbf{y}}_c)$ let us define $\mathbf{X}$ as the matrix made up of $\widehat{\mathbf{y}}_c$ and its similar signals $\mathrm{SS}(\widehat{\mathbf{y}}_c)$, i.e., $\mathbf{X} = [\widehat{\mathbf{y}}_c\ \mathrm{SS}(\widehat{\mathbf{y}}_c)]$, and following Equation (3.12) the noise-free version $\widehat{\mathbf{X}}$ is obtained with the low rank approximation given by $\mathbf{U}\mathbf{\Sigma}_k\mathbf{V}^\intercal$ considering the estimated level of noise γ.

3.2.2.3 | Signal Estimation

$\widehat{\mathbf{y}}_c$ is updated from $\widehat{\mathbf{X}}$, according to Equation (3.13).

$$\widehat{\mathbf{y}}_c = \frac{1}{l}\sum_{i=1}^{l}\widehat{\mathbf{x}}_i \tag{3.13}$$

where $\widehat{\mathbf{x}}_i$ is the $i-th$ signal of $\widehat{\mathbf{X}}$ and l is the number of signals in $\widehat{\mathbf{X}}$.

3.2.2.4 | Aggregation

The restoration of the MR sub-volumes from $\widehat{\mathbf{Y}}$ involves the aggregation of overlapped voxels, which can lead to the blurry recovery of the voxel. However, as mentioned before, weighting the voxels can control blurring. Now, the voxels to be aggregated belong to sub-volumes (signals), which may be frequent (has many similar signals) or rare (has a few similar signals). Since the frequent sub-volumes are better estimated than the rare sub-volumes because of the number of signals averaged in Equation (3.13), these voxels should have more weight than the voxels from the rare sub-volumes. Therefore, we propose weighting the voxel according to the rarity of the signal they belong to.

Similar to the procedure outlined in (Leal et al. (2019)), the global influence of atoms can be used to establish the rarity of a signal. For example, a signal will be rare if it accumulates little global influence; it will be frequent if it accumulates a lot of global influence. Equation (3.14) allows computing the rarity of a signal based on the global influence of the atoms that make it up.

$$R(\widehat{\mathbf{y}}_c) = \langle \mathbf{GI}, \boldsymbol{\alpha}_c \rangle \tag{3.14}$$

where $R(\widehat{\mathbf{y}}_c)$ denotes the rarity score of the signal $\widehat{\mathbf{y}}_c$, $\langle , \rangle$ denotes the dot product, and $\boldsymbol{\alpha}_c$ is the c-th column vector of $\mathbf{A}$, which represents the sparse representation of $\widehat{\mathbf{y}}_c$ on $\mathbf{D}'$.

High scores of Equation (3.14) are related to frequent signals, while low scores are related to rare signals. The denoised version of the voxel v is obtained according to Equation (3.15), after converting back the signals into sub-volumes.

$$v = \frac{\sum_{i \in \mathbb{C}(v_i)} R(V_i) v_i}{\sum_{i \in \mathbb{C}(v_i)} R(V_i)} \tag{3.15}$$

where v_i is a version of the voxel v contained in the sub-volume V_i, $R(V_i)$ is the rarity score of the signal $\widehat{\mathbf{y}}_i$ corresponding to the sub-volume V_i, and $\mathbb{C}(v_i)$ denotes the set of sub-volumes V_i that contains a version of v.

3.2.3 | Scaling

An important parameter for denoising based on sparse representations is the patch size. Large patches lead to denoised images suffering from blurring effect, while small patches lead to denoised images that can keep a high level of noise. However, small patches keep also fine details of the original image.

Averaging images denoised using different patch sizes can carry out a good trade-off between blurring and fine details. The noisy image can be denoised several times; but, each time with a different patch size, then the denoised versions of the image are averaged. The different patch sizes for processing the image are known as scales. Let us define $\widehat{V}_n$ as the denoised version of a noisy MR image V using the proposed method with a sub-volume of size $n \times n \times n$. The averaged denoised version $\widehat{V}$ of V, is obtained using Equation (3.16).

$$\widehat{V} = \frac{1}{|VS|} \sum_{i \in VS} \widehat{V}_i \tag{3.16}$$

where $|VS|$ denotes the number of elements in VS, and VS is the set of different sub-volume sizes for processing V. In our tests, we achieved the best results by averaging the denoised versions $\widehat{V}_3$ and $\widehat{V}_4$. To obtain the final output $\widehat{V}^*$, we apply the inverse VST (VST^{-1}) to the denoised volume $\widehat{V}$. The denoising of Rician data using the proposed method, Non-local SVD Denoising — NLSD, is synthesized by Equation (3.17)

$$\widehat{V}^* = VST^{-1}(NLSD(VST(V,\sigma),\gamma),\sigma) \tag{3.17}$$

where γ is the stabilized standard deviation induced by the VST, V is the volume corrupted by Rician noise with standard deviation σ.

3.3 | Results and Discussion

We conducted several experiments to obtain the values of the parameters for the optimal setting of our method and to compare some state-of-the-art methods. These experiments were conducted in MATLAB R2016a running under the Windows 10 Professional OS on an Intel Core i7 First Generation CPU with 8GB of memory.

A dataset of MR phantom images (1 T1w, 1 T2w, and 1 PDw) from the BrainWeb data base (Cocosco et al. (1997)), with a size of $181 \times 217 \times 181$ voxels (resolution = 1 mm^3), was used for numerical comparisons, as well as for setting the optimal parameter values of our method.

3.3.1 | Parameter Estimation

The first stage of our method, which is preceded by the VST, aims to compute the global influence to reinforce the atoms for avoiding blurring in the denoised image. This reinforcing is controlled by the parameter δ, which does not intervene in the remaining stages. For determining a suitable value for this parameter, it was performed an experiment which consisted of corrupting the dataset of MR phantom images with different levels of Rician noise (1–10% of the maximum intensity), i.e. from each volume of the dataset were obtained 10 different noisy versions, one per each level of noise, for a total of 30 corrupted images. Then, we ran the first stage of our method over each corrupted image, followed by the inverse VST. Finally, we calculate the widely recognized quality measures Peak Signal to Noise Ratio (PSNR), and the Structural Similarity Index (SSIM) (Wang et al. (2004)) of each denoised image to establish the best value for this parameter numerically.

Figure 3.4 shows the results of applying the first stage of our method over the dataset of MR phantom images corrupted with the different Rician noise levels. Each point on the green curve is the average PSNR of the denoised images for a given value of δ, and each point on the blue curve is the average SSIM.

We observed that the PSNR is maximum (31.991) at $\delta = 8$ and the SSIM is maximum (0.8934) at $\delta = -3$. It is preferable to choose the value of δ that generates the maximum PSNR instead of the value that generates the maximum SSIM. Since this metric (PSNR) is more sensitive to noise than the SSIM (which is more correlated with a human visual system) Hore and Ziou (2010), and by choosing the value of δ that give us the maximum PSNR we are choosing the cleaner search space for the next stage. Additionally, the best PSNR and SSIM pair is reached at $\delta = 8$.

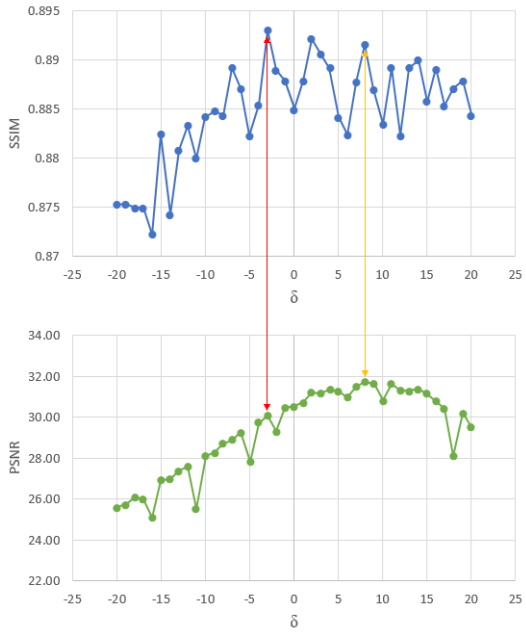

Figure 3.4: Summary of the tests performed to numerically establish the best value of the parameter δ for controlling the global influence of the atoms. The red arrow points out the maximum SSIM (blue curve) and its corresponding PSNR (green curve). The yellow arrow points out the maximum PSNR and its corresponding SSIM.

The second stage of our method is to perform the Non-Local-SVD filtering. At this stage, we search for similar signals to a reference signal in the clean space given by the first stage. We defined a variable threshold in the interval $[b - a, b]$ for establishing the level of similarity between the signals (right side of the inequality in Equation (3.9)). This threshold depends on the magnitude of $\widehat{\mathbf{y}}_c$ and the noise level γ estimated in the first stage. The interval where the threshold moves is determined by the constants a and b. To establish a suitable value for these constants, it was performed an experiment which consisted of running the second stage of our method over the sparse representation $\widehat{\mathbf{Y}} = \mathbf{D}'\mathbf{A}$ of each denoised image produced by the tests of the first stage (previous to the application of the inverse VST), trying different values for a and b. In this experiment, the application of the second stage of our method was followed by the inverse VST. Figure 3.5 shows the results. Each point on the PSNR surface (Figure 3.5a) represents the average of the PSNRs computed after applying the second stage or our method over the images denoised by the first stage, for a given pair of values a and b. Similarly, Each point on the SSIM surface (Figure 3.5b) is the average SSIM.

As shown in Figure 3.5a, the maximum PSNR is equal to 36.247, which is reached at $a = 0.06$ and $b = 0.18$. At this point, the SSIM is 0.9407. As shown in Figure 3.5b, the

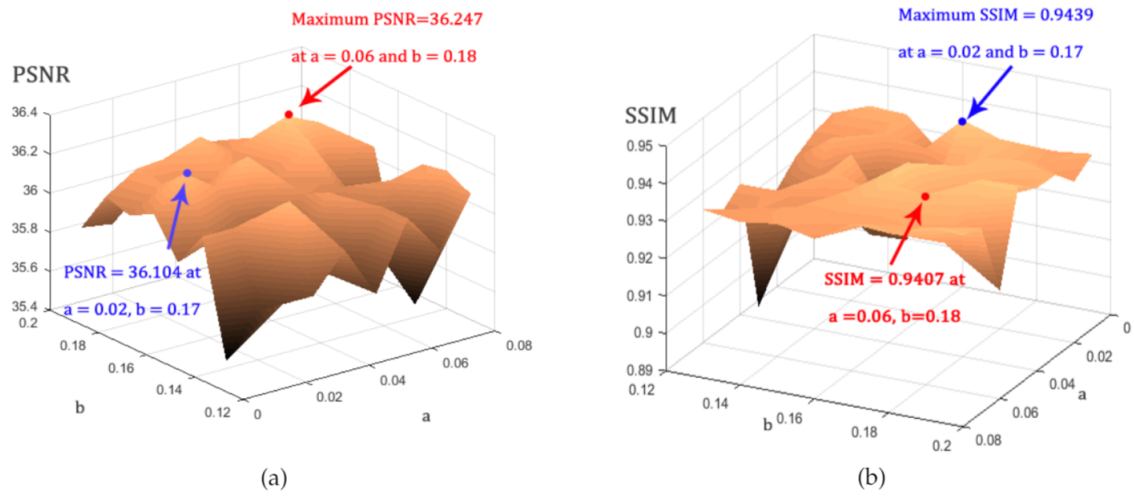

Figure 3.5: Summary of the tests performed to numerically establish the best values for the parameters a and b for controlling the similarity between the signals according to the magnitude of the reference signal and the estimated level of noise. (**a**) PSNR surface where each point corresponds to the average PSNR of the MR phantom images corruped with different Rician noise levels and denoised using the two first stages of our method. (**b**) SSIM surface obtained similarly to the PSNR surface.

maximum SSIM is 0.9439, which is reached at $a = 0.02$ and $b = 0.17$. At this point, the PSNR is 36.104. We chose the pair $a = 0.06$ and $b = 0.18$ because the increment of the PSNR at this point with respect to the PSNR at the point where the maximum SSIM is reached, is more significant than the increment of the SSIM at $a = 0.02$ and $b = 0.17$, with respect to the SSIM at the point where the maximum PSNR is reached.

3.3.2 | Methods Comparison

This method for MR images denoising, named NLSD, was compared to the following widely adopted filters: KSVD (Aharon et al. (2006a)), PRINLM (Manjón et al. (2012)) (implementation downloaded from Coupé (2019)), BM4D (Maggioni et al. (2013)) (implementation downloaded from Tampere University of Technology (2019)), and DnCNN (Zhang et al. (2017)) (implementation dowloaded from Zhang (2020)). The implementation of the methods PRINLM and BM4D used for comparison are developed in MATLAB with its core developed in C++. The DnCNN, the KSVD, and the NLSD, are implemented purely in MATLAB and do not use any graphic acceleration. The application of the KSVD was preceded by the VST, and followed by its inverse. Both quantitative and qualitative comparisons were performed for demonstrating the effectiveness of this method.

3.3.2.1 | Synthetic Data

For numerical comparisons, we used the MR phantom images dataset, corrupted with Rician noise (1–10% of the maximum intensity). The PSNR, and the SSIM were used to evaluate the performance. Figures 3.6–3.17 and Tables 3.1–3.4 show the results of these comparisons.

Figure 3.6 shows the results of the comparisons on the T1w synthetic noise-free MR image corrupted with 5% Rician noise. It shows that the methods PRINLM, BM4D, DnCNN, and NLSD perform very well removing noise; however, the PRINLM produces some artifacts as the zoom-in in Figure 3.7d,k show. The KSVD and the BM4D also produce artifacts but to a lesser extent, as shown in Figure 3.7c,e, respectively, and Figure 3.7j,l respectively. The DnCNN over-smooth the image and therefore fine details as shown in Figure 3.8m. Instead, the NLSD removes noise while keeping fine details, in addition, does not produce artifacts. The KSVD maintains a lot of residual noise, as well as the BM4D, although to a much lesser extent, as shown in Figure 3.8c,e, respectively. Figures 3.8d,g show that the PRINLM and the NLSD, respectively, do not keep residual noise. Figure 3.8h–n show the zoom-in on the details labeled as "c" in Figure 3.6. It shows that the methods KSVD, BM4D, and DnCNN are affected by the blurring effect (Figure 3.8j,l,m, respectively). The PRINLM (Figure 3.8k) and the NLSD (Figure 3.8n) keep fine details; however, the PRINLM tends to swell such details. Table 3.1 summarizes the results of the numerical tests in the T1w synthetic MR image. Bold highlights indicate the best results.

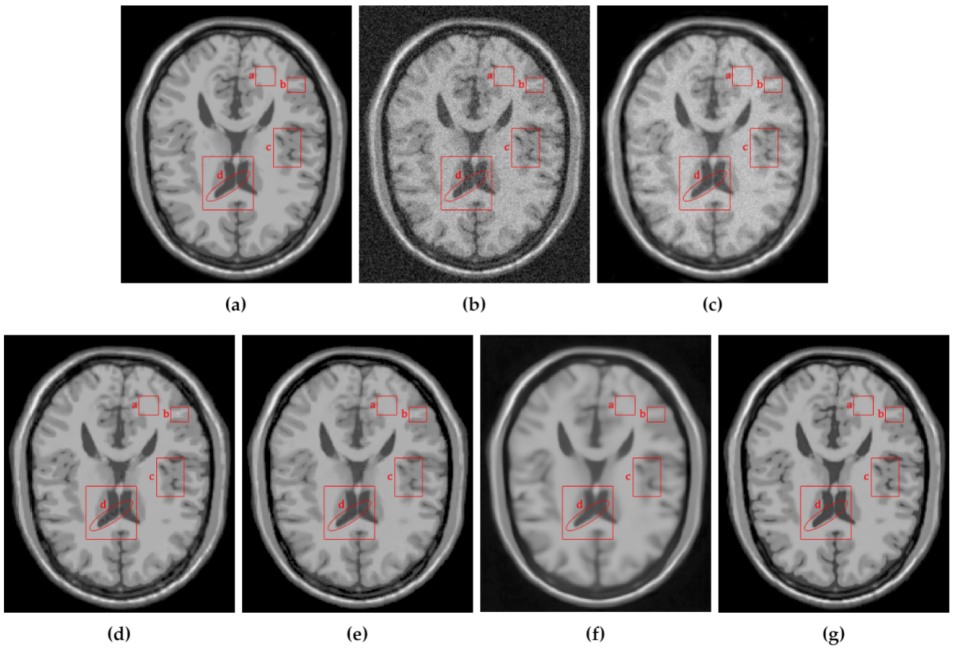

Figure 3.6: Comparison of the denoising methods on the T1w synthetic noise-free MR image corrupted with 5% Rician noise. (**a**) Original synthetic noise-free MR image. (**b**) Original image corrupted with 5% Rician noise. (**c**–**g**) Denoising results of the KSVD, PRINLM, BM4D, DnCNN, and the proposed method NLSD.

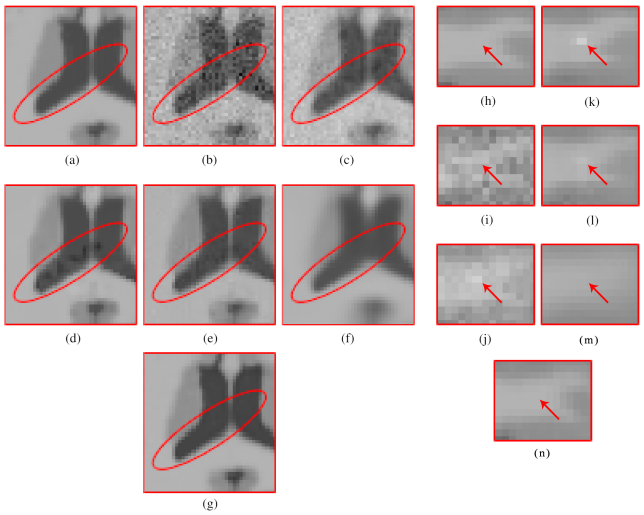

Figure 3.7: Zoom-in on the details of the regions labeled as "d" and "b" in Figure 3.6. Figures (**a**–**g**) show the detail labeled as "d" in Figure 3.6a–g respectively. Figures (**c**–**g**) Correspond to the methods KSVD, PRINLM, BM4D, DnCNN and NLSD, respectively. Figures (**h**–**n**) show the detail labeled as "b" in Figure 3.6a–g respectively. Figure (**j**–**n**) Correspond to the methods KSVD, PRINLM, BM4D, DnCNN, and NLSD, respectively.

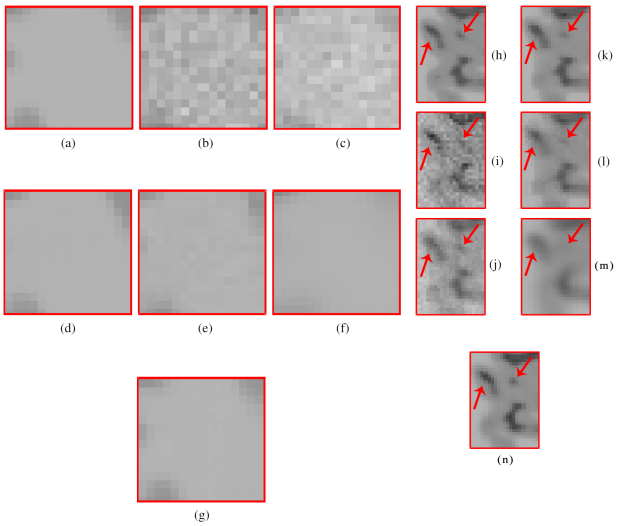

Figure 3.8: Zoom-in on the details of the regions labeled as "a" and "c" in Figure 3.6. Figure (**a**–**g**) correspond to the regions labeled as "a" and Figure (**h**–**n**) correspond to the regions labeled as "c". Figure (**c**–**g**) and (**j**–**n**) correspond to the zoom-in on the results of the methods KSVD, PRINLM, BM4D, DnCNN and NLSD, respectively.

Figure 3.9 qualitatively compares the denoising methods from the residual images (images resulting from the difference between the denoised and noisy images). It shows that the KSVD retains some structural information, and the DnCNN to a lesser extent, while the PRINLM, the BM4D, and the NLSD perform very well. However, the NLSD presents both a higher PSNR and a higher SSIM, as Table 3.1 shows.

Figure 3.10 shows the results of the comparisons on the T1w synthetic noise-free MR image corrupted with 9% Rician noise. It shows that the PRINLM do not eliminate the noise in dark regions but tends to flatten (circled area) and destroy fine details (red arrows). BM4D also keep noise in dark areas (circled area) and also destroy fine details. The DnCNN remove noise but over-blur the image destroying fine details. The KSVD keep a lot of noise and destroy fine details. The NLSD instead keep fine details and perform very well removing noise. You can zooming in the images to appreciate the details. Figure 3.11 shows the qualitative comparison of the method evaluated from the residual images. No structural information is observed on the residuals of the NLSD. The residuals of the KSVD and the DnCNN present some structural information. The residuals of the PRINLM and the BM4D also present structural information to a lesser extent.

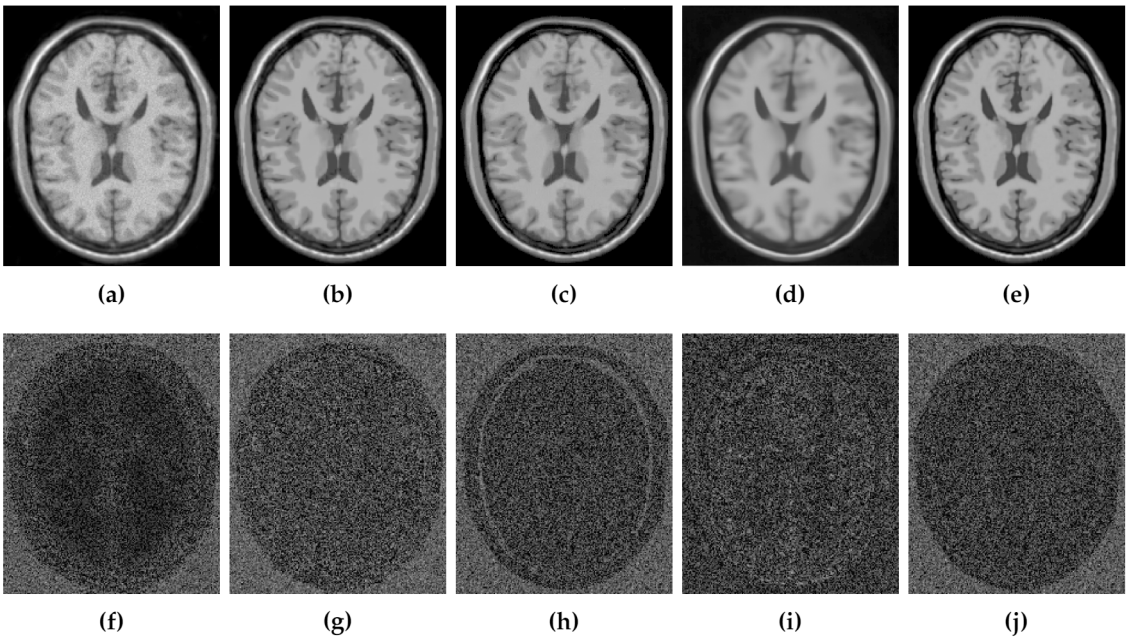

Figure 3.9: Residuals of the different results produced by the application of the methods evaluated on the noise-free T1w synthetic MR image of Figure 3.6a corrupted with 5% Rician noise. (**a**–**e**) are the denoising results of the methods KSVD, PRINLM, BM4D, DnCNN, and NLSD, respectively. (**f**–**j**) are the corresponding residuals.

Table 3.1: Comparison of the different methods evaluated on the T1w synthetic noise-free MR image corrupted with different levels of Rician noise. Bold highlights indicate the best results

	1%		**3%**		**5%**		**7%**		**9%**	
Method	**PSNR**	**SSIM**	**PSNR**	**SSIM**	**PSNR**	**SSIM**	**PSNR**	**SSIM**	**PSNR**	**SSIM**
Noisy	39.980	0.9658	30.451	0.8084	25.982	0.6644	23.045	0.5536	20.888	0.4693
KSVD	40.421	0.9773	32.637	0.9225	29.509	0.8605	27.588	0.8014	26.423	0.7368
PRINLM	44.299	0.9930	38.589	0.9655	35.512	0.9281	33.642	0.8654	**33.177**	0.8332
BM4D	44.688	0.9911	38.129	0.9799	35.618	0.9643	32.799	0.9404	30.412	0.9115
DnCNN	43.109	0.9756	37.843	0.9602	34.790	0.9581	33.744	0.9478	31.501	0.9163
NLSD	**44.901**	**0.9970**	**38.723**	**0.9895**	**35.801**	**0.9776**	**33.982**	**0.9630**	33.130	**0.9296**

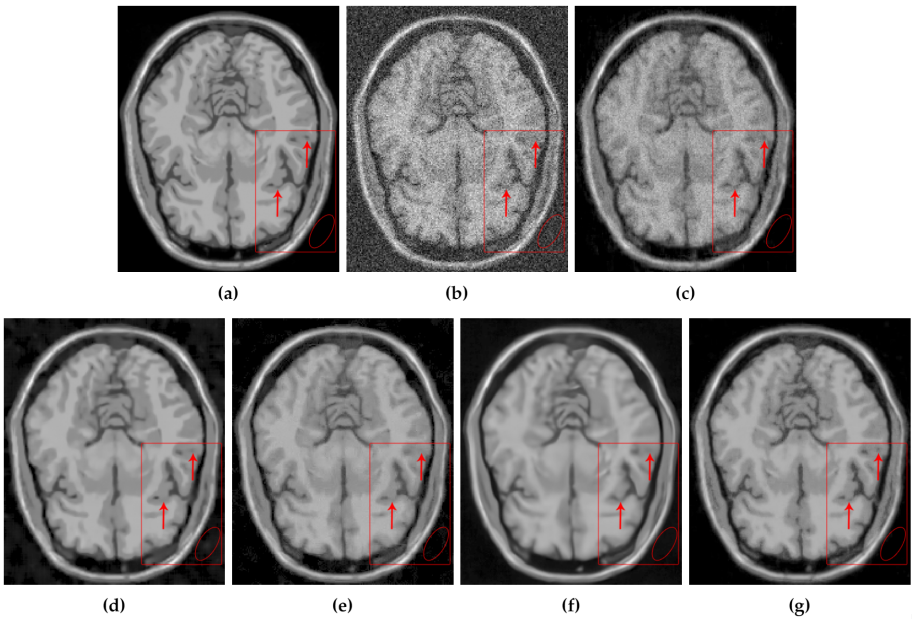

Figure 3.10: Comparison of the denoising methods on the T1w synthetic noise-free MR image corrupted with 9% Rician noise. (**a**) Original synthetic noise-free MR image. (**b**) Original image corrupted with 9% Rician noise. (**c**–**g**) Denoising results of the KSVD, PRINLM, BM4D, DnCNN and the proposed method NLSD.

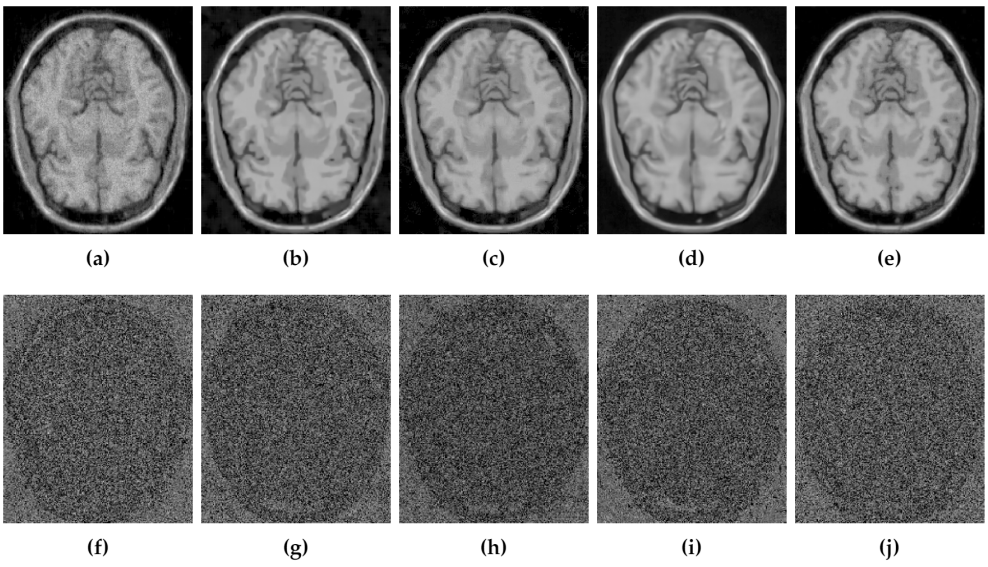

Figure 3.11: Residuals of the different results produced by the application of the methods evaluated on the noise-free T1w synthetic MR image of Figure 3.10a corrupted with 9% Rician noise. (**a**–**e**) are the denoising results of the methods KSVD, PRINLM, BM4D, DnCNN and NLSD, respectively. (**f**–**j**) are the corresponding residuals.

Figure 3.12 shows the results of the comparisons on the T2w synthetic noise-free MR image corrupted with 7% Rician noise. It shows that the image filtered by the KSVD (Figure 3.12c) keeps high levels of noise, which is corroborated by the corresponding zoom-in of region “c” in Figure 3.13c. The BM4D also keeps noise, although to a lesser extent, as shown in region “c” in Figure 3.13e. The DnCNN over-blur the image and destroy fine details, as can be seen in the corresponding zoom-in of region "b" in Figure 3.13f.The methods PRINLM and NLSD perform very well at removing noise; however, as shown in the zoom-in of the regions “a” and “b” in Figure 3.13d, the PRINLM produces artifacts. The NLSD does not produce artifacts. Figure 3.14 qualitatively compares the denoising methods from the residual images. It shows that the KSVD presents a correlated residual image and also the BM4D. The DnCNN present a residual image that keep some estructural information, but to a lesser extent, while the PRINLM, and the NLSD perform very well. However, the NLSD presents both a higher PSNR and a higher SSIM, as Table 3.2 shows. Table 3.2 summarizes the results of the numerical tests in the T2w synthetic MR image. Bold highlights indicate the best results.

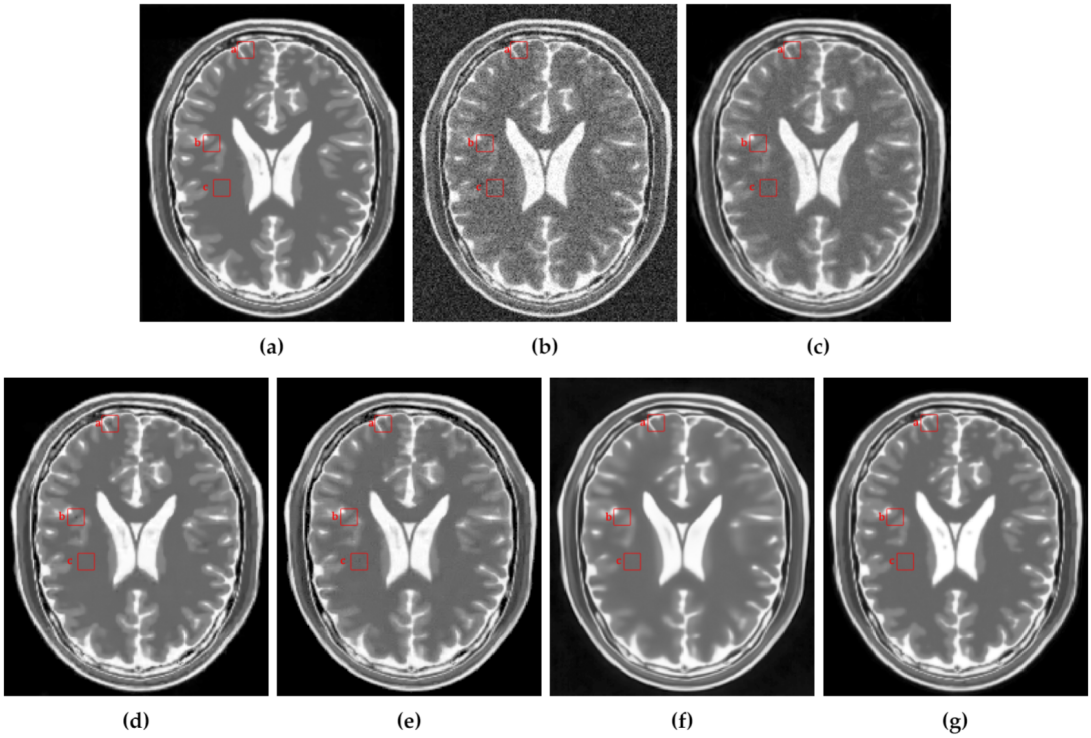

Figure 3.12: Comparison of the denoising methods on the T2w synthetic noise-free MR image corrupted with 7% Rician noise. (**a**) Original synthetic noise-free MR image. (**b**) Original image corrupted with 7% Rician noise. (**c**)–(**g**) Denoising results of the KSVD, the PRINLM, the BM4D, the DnCNN and the NLSD respectively.

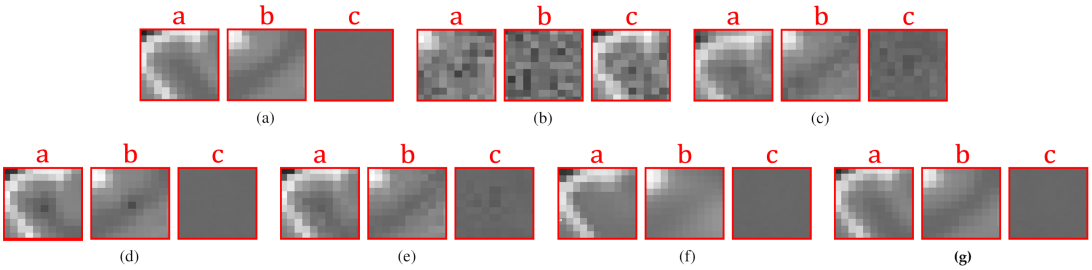

Figure 3.13: Zoom-in on the details labeled as “a”, “b”, and “c” in Figure 3.12. Figures (**a**–**g**) correspond to the zoom-in of the Original image, the Noisy image, the KSVD, the PRINLM, the BM4D, the DnCNN, and the NLSD, respectively.

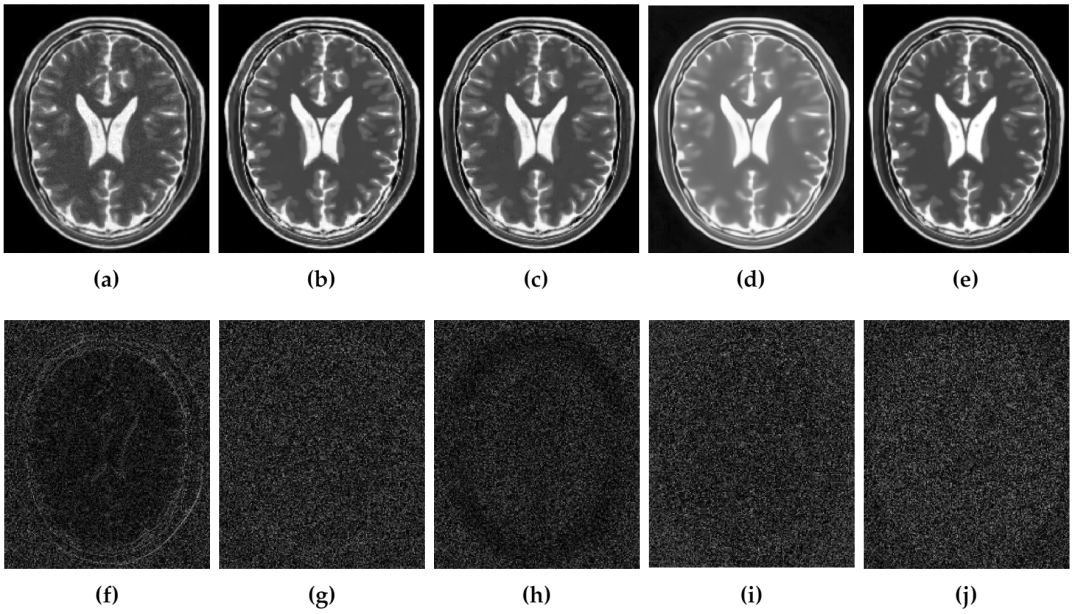

Figure 3.14: Residuals of the different results produced by the application of the methods evaluated on the noise-free T2w synthetic MR image of Figure 3.12a corrupted with 7% Rician noise. (**a**–**e**) are the denoising results of the methods KSVD, PRINLM, BM4D, DnCNN, and NLSD, respectively. (**f**–**i**) are the corresponding residuals.

Table 3.2: Comparison of the different methods evaluated on the T2w synthetic noise-free MR image corrupted with different levels of Rician noise. Bold highlights indicate the best results

	1%		**3%**		**5%**		**7%**		**9%**	
Method	**PSNR**	**SSIM**	**PSNR**	**SSIM**	**PSNR**	**SSIM**	**PSNR**	**SSIM**	**PSNR**	**SSIM**
Noisy	39.992	0.9709	30.418	0.8330	26.016	0.7151	23.073	0.6242	20.928	0.5606
KSVD	40.104	0.9706	32.098	0.9166	29.342	0.8669	26.530	0.8134	24.664	0.7633
PRINLM	43.985	0.9943	37.786	0.9703	34.738	0.9262	32.918	0.8852	31.347	0.8286
BM4D	43.655	0.9614	37.166	0.9473	34.140	0.9373	31.887	0.9273	30.030	0.9100
DnCNN	42.897	0.9569	37.003	0.9354	34.362	0.9210	32.544	0.9162	31.045	0.9139
NLSD	**44.099**	**0.9978**	**37.973**	**0.9885**	**34.910**	**0.9522**	**33.546**	**0.9327**	**31.601**	**0.9233**

Figure 3.15 shows the results of the comparisons on the PDw synthetic noise-free MR image corrupted with 5% Rician noise. Figure 3.16 shows the zoom-in of the regions labeled as "a" and "b" in Figure 3.15. It shows that the BM4D and mainly the KSVD retain noise, as shown in Figure 3.16c,e in the corresponding zoom-in. The DnCNN perform

very well filtering noise but over-blur the image destroying fine details, as can be seen in Figure 3.16f. The PRINLM and the NLSD perform very well, although the NLSD (Figure 3.16g) tends to preserve some fine structures better than the PRINLM. Figure 3.16d shows how the PRINLM tends to thicken or destroy such structures. Figure 3.17 qualitatively compares the denoising methods from the residual images. It shows that the KSVD presents a correlated residual image. The BM4D and DnCNN also shows a bit of correlation, while the PRINLM and the NLSD perform very well. However, the NLSD presents both a higher PSNR and a higher SSIM, as Table 3.3 shows. Table 3.3 summarizes the results of the numerical tests in the PDw synthetic MR image. Bold highlights indicate the best results. Table 3.4 presents the running time of the methods.

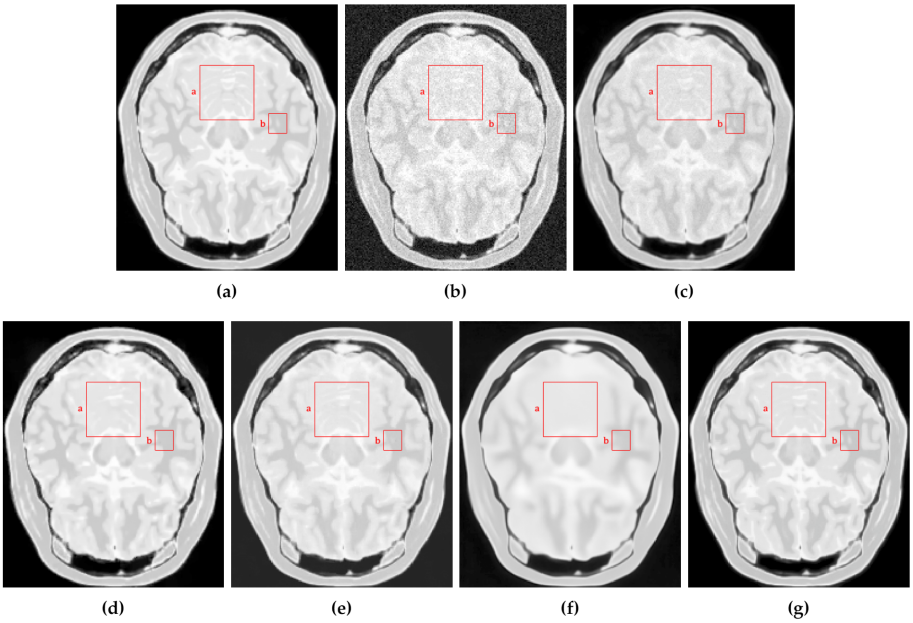

Figure 3.15: Comparison of the denoising methods on the PDw synthetic noise-free MR image corrupted with 5% Rician noise. (**a**) Original synthetic noise-free MR image. (**b**) Original image corrupted with 5% Rician noise. (**c**–**g**) are the denoising results of the KSVD, the PRINLM, the BM4D, the DnCNN and the NLSD, respectively.

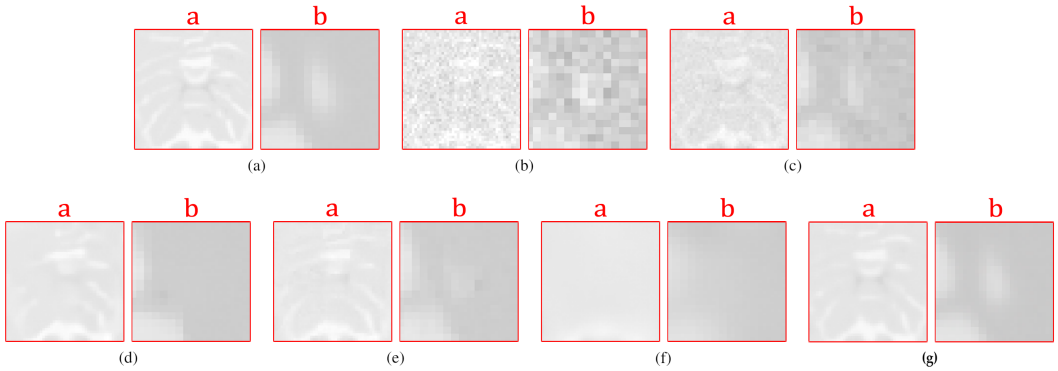

Figure 3.16: Zoom-in on the details labeled as "a" and "b" in Figure 3.15. Figures (**a**–**g**) correspond to the zoom-in of the Original image, the Noisy image, the KSVD, the PRINLM, the BM4D, the DnCNN and the NLSD in Figure 3.15, respectively.

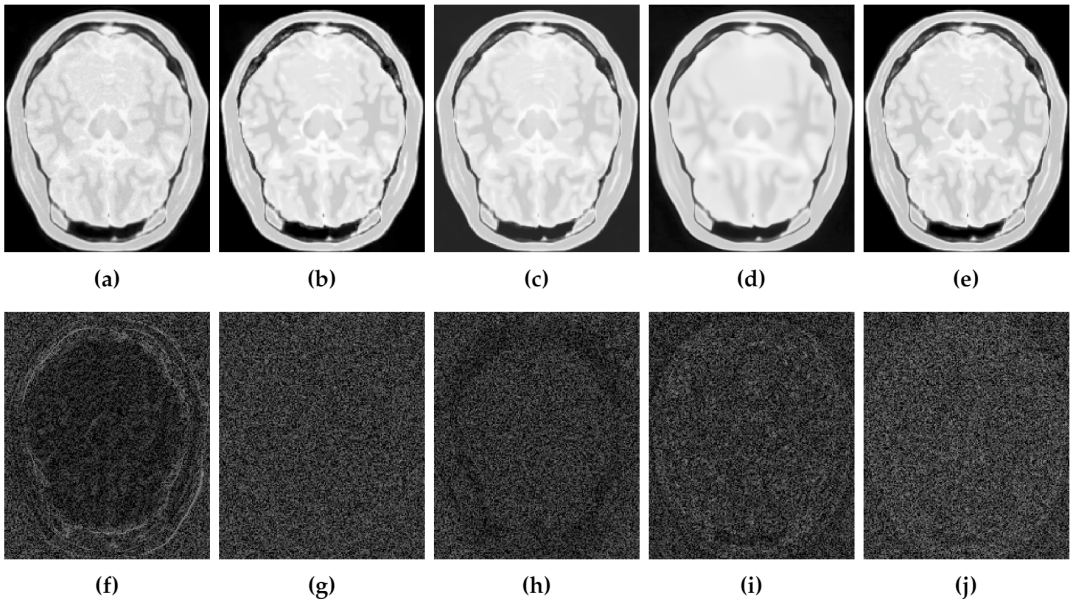

Figure 3.17: Residuals of the different results produced by the application of the methods evaluated on the noise-free PDw synthetic MR image of Figure 3.15a corrupted with 5% Rician noise. (**a**–**e**) are the denoising results of the methods KSVD, PRINLM, BM4D, DNCNN and NLSD, respectively. (**f**–**j**) are the corresponding residuals.

Table 3.3: Comparison of the different methods evaluated on the PDw synthetic noise-free MR image corrupted with different levels of Rician noise. Bold highlights indicate the best results

	1%		3%		5%		7%		9%	
Method	**PSNR**	**SSIM**	**PSNR**	**SSIM**	**PSNR**	**SSIM**	**PSNR**	**SSIM**	**PSNR**	**SSIM**
Noisy	39.971	0.9636	30.441	0.7901	25.984	0.6341	23.088	0.5250	20.898	0.4408
KSVD	39.980	0.9639	29.633	0.8956	27.626	0.8128	26.224	0.7357	24.952	0.6589
PRINLM	44.699	0.9940	38.079	0.9752	35.111	0.9228	33.101	0.8638	32.562	0.8211
BM4D	44.603	0.9626	38.621	0.9399	35.683	0.9280	**33.653**	0.9147	31.887	0.8990
DnCNN	43.245	0.9567	37.991	0.9268	35.700	0.9372	33.419	0.9075	30.643	0.8986
NLSD	**44.980**	**0.9987**	**38.906**	**0.9894**	**35.973**	**0.9532**	33.625	**0.9387**	**32.656**	**0.9102**

Table 3.4: Implementation language and computation time of the methods evaluated

	PRINLM	**BM4D**	**DnCNN**	**KSVD**	**NLSD**
Language	MATLAB - C++	MATLAB - C++	MATLAB	MATLAB	MATLAB
Average running time	45.32 s	46.83 s	65.64 min	70.13 min	120.84 min

3.3.2.2 | Real Data

For qualitative comparisons on real clinical data, we used a data set of T1w brain MR images acquired in a 1.5T Siemens Magnetom equipped with a standard head coil. The parameters of the T1w images were: TR = 7.9 ms, TE = 3.8 ms, ACQ matrix 220 $\times$ 220 pixels, voxel size 0.5 mm $\times$ 0.5 mm $\times$ 0.5 mm. We compared the NLSD results to the PRINLM, the BM4D and the DnCNN results. The KSVD was not considered because its performance was much lower in the tests on synthetic data. Figure 3.18 shows the results. The four methods perform very well, as can be seen in their corresponding zoom-ins; however, the BM4D and DnCNN results are slightly blurry and retain some noise. The PRINLM also keeps some residual noise. It can be noted that, close to the dark areas the BM4D and the PRINLM maintain residual noise slightly flattened, as can be seen in the zoom-in. The NLSD instead reduces noise while keeping fine details and yielding better visual results. This can be seen around the skull, where almost there is no any noisy pixel. This is because of the variable threshold in Equation (3.9) and the better estimation of the signals achieved by the search of similar signals in the clean space given by $\mathbf{D}'\mathbf{A}$.

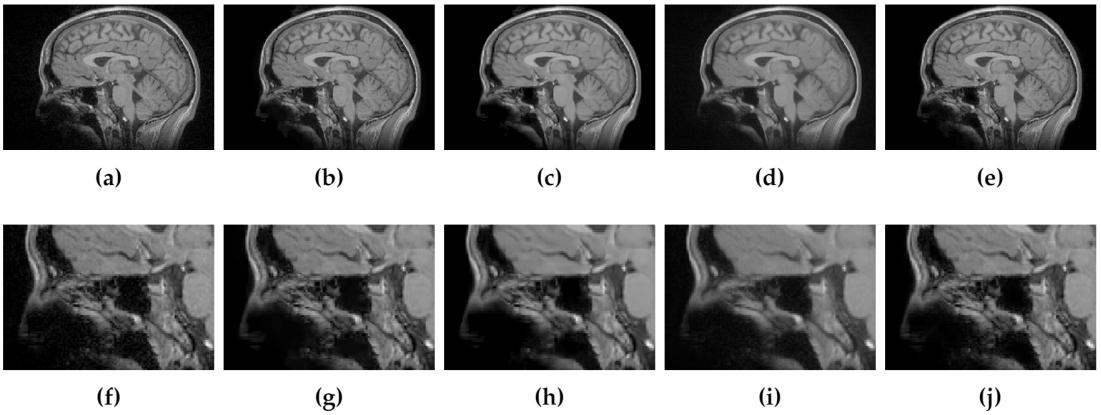

Figure 3.18: Quality comparisons on a real T1w MR image. (**a**) Original MR image, (**b**–**e**) denoising results of the PRINLM, the BM4D, the DnCNN, and the NLSD. (**f**–**i**) the corresponding zoom-in of figures (**a**–**e**).

3.4 | Conclusions

In this chapter was presented a new method for MR images denoising based on non-local means, singular value decomposition, and sparse representation. Both qualitative and quantitative results validate the effectiveness of the proposed method. It was demonstrated how the global influence of the dictionary atoms could act as weighting factors to improve the noise filtering while keeping the fine details of the image and reducing the blurring effect caused by the average of overlapping patches.

It was also demonstrated how the strategy of non-local means could be applied directly from the dictionary without resorting to the use of search windows, which limit the search for similar signals (patches or sub-volumes) to a given region. The dictionary, instead, allows finding similar signals in any location of the MR image without exploring the whole volume; and therefore, improving the filtering. Additionally, the strategy of searching for similar signals in the clean space given by the sparse representation allows the process of collecting such signals to improve; since, the level of noise in this space is lower than in the original space given by the noise MR image. Finally, it was also showed how the estimated level of noise in the image could be used for computing efficiently the number of singular values, to obtain a low-rank approximation of the set of similar signals, and to reduce their noise before proceeding to the estimation of the noise-free signal.

Previous strategies lead us to an improve in the denoising task, as showed the numerical results of Tables 3.1 — 3.3, which show that the proposed method outperform the BM4D, the PRINLM, the DnCNN, and the KSVD, whereby the first objective of this

research is met.

There is a work to do in the computational effort of the proposed method, which is very high, as shown in Table 3.4. This is because the objective was the effectiveness of the methods, not considering efficiency in the first instance, which is an issue that can be addressed in the continuity of the research through the application of analysis and design algorithm techniques, parallelization and integration with libraries developed on more efficient platforms

4

Improving segmentation

Segmentation is an important intermediate task in digital image processing, which tries to isolate the objects of interest in an image, to extract invariant descriptors to orientation, location, and size for classifying or recognizing such objects from these descriptors. However, this is a non-trivial task because normally the limits between regions may be neither clear or well defined. This chapter presents a novel method for improving the boundaries definition among segmented regions from a MR image. This method, from a label matrix of segmented regions and the original MR image, yields a new improved label matrix in which the limits among regions are better defined according to the ground truth segmentation. To determine if a pixel/voxel belongs to its assigned region, it is built a patch (or subvolume) around the pixel/voxel and also dictionaries from the patches of the regions that border such a pixel/voxel are built; then, it is runned sparse coding on each dictionary to find the sparse representation of the patch that contains the pixel/voxel. The pixel/voxel is assigned to the region whose dictionary represents in the best way the patch/subvolume that contains the pixel/voxel. Processing of patches/subvolumes instead of pixels/voxels makes this method robust to noise, outliers and blurring.

4.1 | Introduction

To recognize or classify an object present in a digital image, normally a process of isolation or separation of such an object from the surrounding background must be carried out; this process, known as segmentation, is one of the most important stages in computer vision. Segmentation facilitates obtaining the object descriptors from which the object can be recognized or classified. However, separate the object from the back-

ground is a nontrivial task that is affected by image conditions like low contrast, blurring and the inherent noise of the image, among others.

Segmenting an image to extract the objects of interest involves finding the limits among the different regions that represent such objects; however, in natural images, normally, these limits may be blurry or noisy, which affects the segmentation process and as a result the extraction of the objects may fail and, consequently, its classification or recognition. Hence, image segmentation continues being an active field of research (Chen and Tai (2010); Dong et al. (2019); He et al. (2019); Lei and Fan (2019); Peng et al. (2019); Stosic et al. (2019); Zheng et al. (2015)).

Several solution approaches to the image segmentation problem have been presented, one of the most important is the Thresholding, which is aimed at partitioning the image according to a threshold value; i.e. The pixels with an intensity level above the threshold are assigned to one class and the rest to another. Under this approach, one of the first and most representative works was presented by (Otsu (1979)) in 1979. This method establishes the best threshold value, to segment an image, by considering the homogeneity within each class and the heterogeneity between the two classes produced by such a threshold.

Other methods may be classified into two approaches: the boundary-based approach and the region-based approach (Cufí et al. (2003)). The boundary-based approach is based on the fact that abrupt changes concerning the pixel features occur at the boundary between two regions. Representative works belonging to this approach were presented by Roberts (Roberts (1965)), Prewitt (Prewitt (1970)), Sobel (Duda and Hart (1973)), and Canny (Canny (1983)).

The region-based approach is aimed to find homogeneous areas according to the pixel features. A representative work of this approach is the region growing algorithm, which was presented by (Adams and Bischof (1994)) in 1994. This algorithm starts at a seed pixel from which the region grows by adding adjacent pixels that are similar in terms of a given criterion. A complete review of the boundary-based approach and the region-based approach can be found in (Cufí et al. (2003)).

More recently, with the advance of computers, the applications of computer vision have extended to many fields like medicine, agriculture, city planning, automatic visual inspection, automatic driving, printed circuit board inspection, and graphical sentiment analysis, to name a few. These new fields of application require more accurate segmentation algorithms, which has led to the development of techniques based on fuzzy logic, evolutionary computing, sparse representations, and deep neural networks, among others.

An important technique for segmenting images, based on fuzzy logic, was presented

by (Zheng et al. (2015)). This proposal is a variant of the well-known fuzzy C-means algorithm, which involves local spatial information and intensity values to overcome the fuzzy C-means, making it robust to image noise and outliers. (Li et al. (2010)) proposed an evolutionary level set-based technique on an edge-based active contour model, for segmenting images, which maintains the regularity of the level set function during the evolution, giving numerical stability and reducing both the number of iteration and the computation time.

In the last decade research in sparse representation has increased due to its potential applications in many fields, one of them is the segmentation of magnetic resonance images (MRI). (Tong et al. (2013)) proposed a dictionary learning and sparse coding-based technique for segmenting the hippocampus on a brain MRI. This proposal uses fixed discriminative dictionary learning for learning dictionaries offline and performing online segmentations. This method reduces significantly the computation time while reaches competitive results with regards to atlas methods.

Segmentation methods based on neural networks have also proved perform very well. (He et al. (2019)) proposed a double-layer pulse-coupled neural network (PCNN) model for segmenting images to detect kiwifruit. The first layer of the PCNN determines the optimal color-difference and the second layer segments the regions. This proposal outperforms some typical existing algorithms. Deep neural models also report good performance. (Badrinarayanan et al. (2017)) presented SegNet, a convolutional deep neural network architecture of 13 layers for image segmentation. SegNet shows competitive results in road scenes and indoor scene segmentation tasks compared to other architectures.

The above are segmentation methods that generally apply for processing any type of images; however, when it is wanted to segment brain MR images, it is important to consider the particularities of these images, such as the dimensionality and type of noise they have. Some methods for segmenting brain MR images have been developed from those previously presented, others have been developed to specifically process this type of images. There are a diversity image segmentation methods since there is no single method that is suitable for processing all images, in the same way, that not all methods behave the same for a given type of image. In general terms, brain MR images segmentation methods can be classified into five classes: manual segmentation, intensity-based methods, atlas-based methods, surface-based methods, and hybrids (Despotović et al. (2015)).

Manual segmentation refers to the process by which a specialist doctor, such as a radiologist or neurologist, among others, classifies the tissues of the imagined object. This method is considered the most accurate. However, it is tedious and tiring, as a brain MR

image can typically be in the order of 200 slices, and each slice is approximately 512x512 voxels. Therefore, manually classifying them in addition to being strenuous can introduce biases in the classification due to the fatigue that the specialist may present during the process. In addition to being considered the most accurate segmentation method, manual segmentation is the starting point of atlas-based segmentation methods, since these are based on previously classified basic models to carry out the segmentation process. A common tool for manual segmentation is ITK-SNAP (Yushkevich et al. (2006)).

As presented at the beginning of this section, intensity-based methods were the most common targeting approaches at the beginning, which has also been adapted to process brain MR images. The first proposals were simple adaptations of thresholding techniques (Pham et al. (2000); Prastawa (2007)) and region growing (del Fresno et al. (2009); Passat et al. (2005); Weglinski and Fabijanska (2011)), but more recently more complex proposals have been presented. These works employ soft computing techniques, more specifically fuzzy logic, to carry out segmentation, showing competitive results. (Kahali et al. (2017)) proposed a fuzzy logic-based framework for segmenting brain MR images. This proposal uses a fuzzy c-means algorithm to process the neighborhood of the voxels for defining both a local membership function and a global membership function for each voxel. This gives the real relationship between the voxel and its neighborhood. This information is used by a modified fuzzy c-means algorithm that incorporates the information of the voxel to decide what region the voxel belongs to.

Atlas-based approach is used when we counting on previously classified (segmented) models. Basically, the task of these methods is to match the brain to segment with the previously classified model (label image known as atlas); therefore, the effectiveness of these methods lies in the registration process. One way to merge the atlas labels and the image to be segmented is by weighted voting. This technique uses as weights the similarity of atlas-target intensity. When there are several atlases, these differences are treated independently when merging the labels with the image to segment. (Wang and Yushkevich (2013)) proposed a fusion label method that exploits the fact that different atlases can produce similar label errors, and therefore these labels can be considered together for improving the atlas-target correspondence. This proposal won the first place in the 2012 MICCAI Multi-Atlas Labeling Challenge.

Given both the dependencies that these methods have on the atlases and the differences that exist in the human, brain depending on the stage of development in which it is found, these methods present important variations. This is the case of the approach proposed by (Makropoulos et al. (2014)) for the segmentation of the developing neonatal brain. This approach models the intensity levels of the entire brain, considering a hierarchical structure and anatomical restrictions, when transferring the labels to the

image to segment.

Atlas-based approach has been also used along with machine learning for improving segmentation results. (Hao et al. (2014)) proposed to use support vector machine (SVM) along with k nearest neighbor (kNN) to learn how classifying the voxels of the target image based on features of intensity and texture of the corresponding surrounding voxels on the atlas. Other important works of the atlas-based approach can be found on (Ashburner and Friston (2005); Prastawa et al. (2005); Weisenfeld and Warfield (2009); Xue et al. (2007))

The widely recognized tool for volumetric brain analysis, volBrain (Manjón and Coupé (2016)), implements several atlas-based approaches for segmenting brain MR images. The volBrain tool, using several pipelines, segments the brain into left-cerebrum, right-cerebrum, left-cerebellum, right-cerebellum, and brainstem. It is also able to classify brain tissues into gray matter, white matter, cerebro spinal fluid, in addition to classify subcortical structures.

Surface-based methods for segmenting brain MR images are adaptions of classical methods of active Contours and Surfaces. Typically, this adaptations are combined with other methods, therefore can be also considered hybrid approaches. An important work under this approach, that addresses neonatal brain image segmentation, was proposed by (L. Wang and Shen (2011)). This method combine active contour/surface models with local intensity information and atlas spatial prior showing promising results. Hybrid methods typically are combination of some of previous methods like intensity based methods with statistical, mathematical morphology, active contours, and artificial neural networks based, among others, for improving segmentation results (Despotović et al. (2015)). (Mesejo et al. (2015)) proposed an geometric deformable model combined with genetic algorithm and scatter search. The genetic algortihm find the features parameters of the voxels and the scatter search perform properly segmentation.

Although the revised methods report good results, they still have problems to solve when operating on images suffering from blurring, noise, and outliers. This chapter presents a method to improve the boundaries of segmented regions of an MR image, from the original image and a given segmentation of it. This method is robust to noise, outliers, and blurring, because it works on patches instead of pixels. It takes advantage of the patches around the pixel neighborhood, which constitute natural dictionaries of the surrounding regions, to establish the real region to which the pixel neighborhood belongs, and therefore, the pixel.

4.2 | Improving the boundaries of segmented regions

This method consists of two stages. The first builds dictionaries from the patches around the pixel neighborhood and the second runs a sparse encoding to establish which dictionary best represents such a neighborhood, and therefore, the region that owns the pixel. Below are presented the two stages of this method.

4.2.1 | Dictionary construction

It is common that the boundaries between regions in digital images are blurry, or are affected by noise and outliers, as Figure (4.1) shows. It can be seen how these situations difficult the boundary definition between two regions, even to human beings. In front of these situations, when it comes to manually detect such boundaries, it would be convenient zooming out the image for getting a better point of view of the scene, to decide where the boundary should be set. However, when it comes to automatically detect the boundaries under such conditions because the pixel itself has not reliable information due to its noisy or blurry context; make a zooming out is equivalent to process the patch around the pixel instead of the pixel itself.

Formally, given an image I and its segmentation in regions given by the label matrix L, the edge matrix of I denoted by E is obtained from Equation (4.1).

$$E = \text{Canny}(L) \tag{4.1}$$

where the Canny function represents the application of the Canny operator on L and E is a binary matrix with $E_{i,j} = 1$ if the pixel $I_{i,j}$ is a boundary pixel, and $E_{i,j} = 0$ otherwise. With i and j being row and column indexes, respectively. We use the Equation (4.1) for obtaining the corresponding boundaries of the regions in L.

Now, to decide if a boundary pixel $I_{i,j}$ belongs to its corresponding region in L, we evaluate what patches of the adjacent regions to $I_{i,j}$ best represent the 3x3 neighborhood of $I_{i,j}$. This is carried out by using sparse representations, as follows:

Let $N_3(I_{i,j})$ be the $3x3$ neighborhood of $I_{i,j}$ and $\mathbf{y}_c \in \mathbb{R}^{9x1}$ its corresponding representation in vector form, and be $\mathbf{D}_1, \mathbf{D}_2, \ldots, \mathbf{D}_n$ the dictionaries created from the patches of the adjacent regions $\mathbf{R}_1, \mathbf{R}_2, \ldots, \mathbf{R}_n$ to the pixel $I_{i,j}$, as illustrates Figure 4.2, the pixel $I_{i,j}$ belongs to the region whose associated dictionary best represents the neighborhood $N_3(I_{i,j})$.

In Figure 4.2, $I_{i,j}$ represents a boundary pixel of the image I, and the pixels in the red square represent its neighborhood $N_3(I_{i,j})$. The yellow blocks and the green blocks represent the patches of the adjacent regions to $I_{i,j}$. Under conditions of blurring or

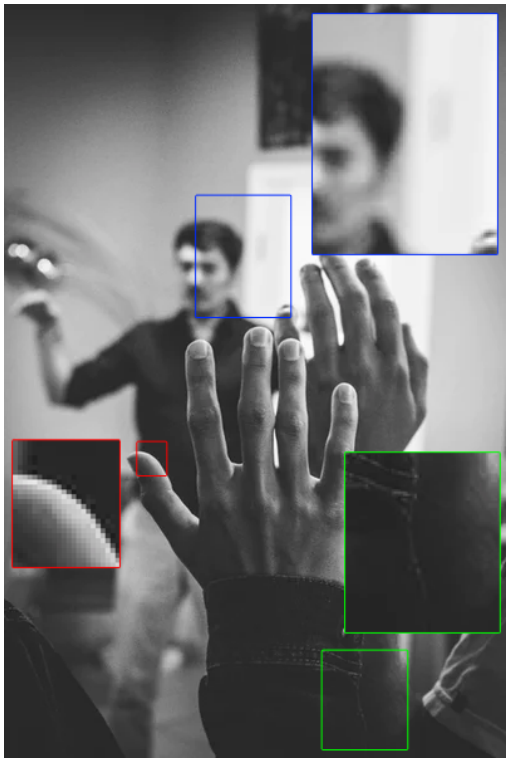

Figure 4.1: Examples of boundaries between regions that can cause the segmentation failed. The red rectangles show a boundary affected by noise. The blue ones show boundaries affected by blurring, and the green ones show a boundary not well defined.

noise, it is not easy to determine whether the pixel $I_{i,j}$ belongs to the dark gray region or to the light gray region.

Therefore, following the example of Figure 4.2, we create two dictionaries because there are two regions adjacent to $I_{i,j}$, so that we use the vector form of the green blocks and the yellow blocks to construct the corresponding dictionaries of the light gray region ($\mathbf{R}_1$) and the dark gray region ($\mathbf{R}_2$), respectively, because such patches constitute themselves natural dictionaries of such regions. The bottom-left and the upper-right yellow blocks, despite containing pixels of the $\mathbf{R}_1$ region, belong to the $\mathbf{R}_2$ region because they contain more pixels of such a region. Figure 4.3 illustrates the process of building dictionaries from the surrounding regions to the Neighborhood $N_3(I_{i,j})$. To establish what dictionary best represents the neighborhood $N_3(I_{i,j})$ we run sparse coding.

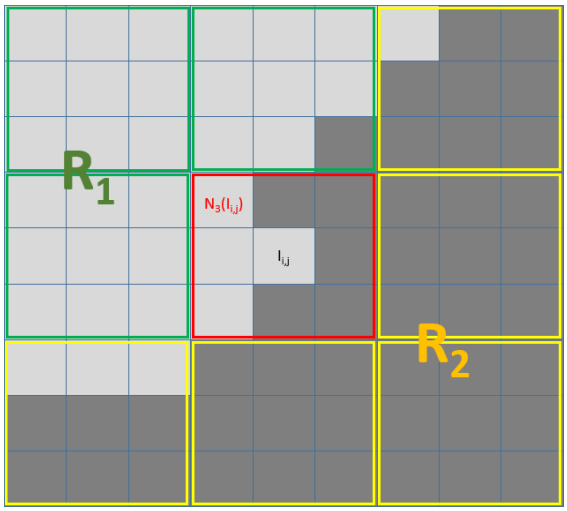

Figure 4.2: Surrounding regions of the pixel neighborhood $N_3(I_{i,j})$.

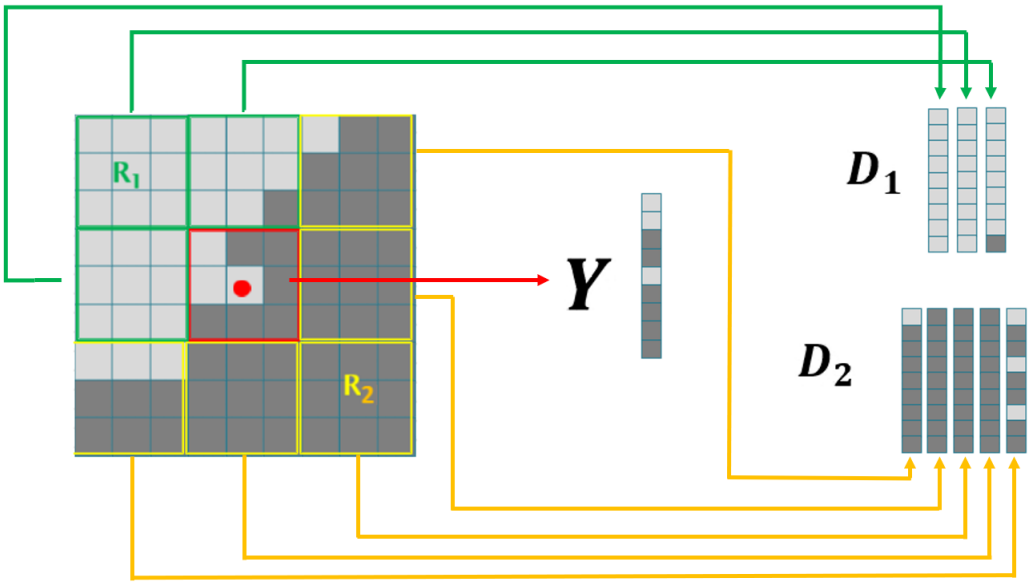

Figure 4.3: Illustration of the construction of dictionaries for the surrounding regions of the pixel neighborhood

4.2.2 | Sparse coding

Once we have built the dictionaries, we run sparse coding on each dictionary for solving Equation 4.2, which is a particular case of the model of Equation 3.1 in which $\mathbf{Y}$ only contains one signal $\mathbf{y}_c$, to obtain the sparse representation of $\mathbf{y}_c$ in each dictionary $\mathbf{D}_i$ of the adjacent regions to $\mathrm{I}_{i,j}$.

$$\min_{\boldsymbol{\alpha}_{ci}} \sum_{c=1}^{\mathrm{P}} \|\mathbf{y}_c - \mathbf{D_i}\boldsymbol{\alpha}_{ci}\|_2^2 + \lambda \|\boldsymbol{\alpha}_{ci}\|_1 \tag{4.2}$$

where $\boldsymbol{\alpha}_{ci}$ represents the sparse representation of $\mathbf{y}_c$ i.e. the sparse representation of $\mathrm{N}_3(\mathrm{I}_{i,j})$ on the dictionary $\mathbf{D}_i$ of the region $\mathbf{R}_i$.

The region $\mathbf{R}_i$ that owns the pixel $\mathrm{I}_{i,j}$ is the one whose represents the neighborhood $\mathrm{N}_3(\mathrm{I}_{i,j})$ with a minimal residual error, where the residual error is defined according to Equation 4.3.

$$\mathrm{r}_i = \|\mathbf{D}_i\widehat{\boldsymbol{\alpha}}_{ci} - \mathbf{y}_c\| \tag{4.3}$$

where $\widehat{\boldsymbol{\alpha}}_{ci}$ is the optimal $\boldsymbol{\alpha}_{ci}$ found in Equation 4.2 for a given $\mathbf{D}_i$, which represents the optimal sparse representation of $\mathbf{y}_c$ in $\mathbf{D}_i$, and r_i is the residual error or the representation error of $\mathbf{y}_c$ in $\mathbf{D}_i$.

4.3 | Results and Discussion

The proposed method for boundary definition improvement was implemented in Mathworks Matlab 2016a. Processing was done in a Windows 10 Professional OS on an Intel Core i7 CPU with 8GB of memory. The method was evaluated on synthetic images, natural images and slices of MRI through the widely recognize Sørensen–DICE coefficient, which is calculated according to Equation 4.4.

$$\mathrm{D}(A,B) = \frac{2\mathrm{TP}}{(\mathrm{FP}+\mathrm{TP}) + (\mathrm{FN}+\mathrm{TP})} \tag{4.4}$$

where TP is the true positives, FP is the false positives and FN is the false negatives, concerning the ground truth segmentation.

The region growing algorithm Coupé et al. (2008) and a PCNN model Tao et al. (2016) were used for obtaining the initial segmentations to be improved by using our method.

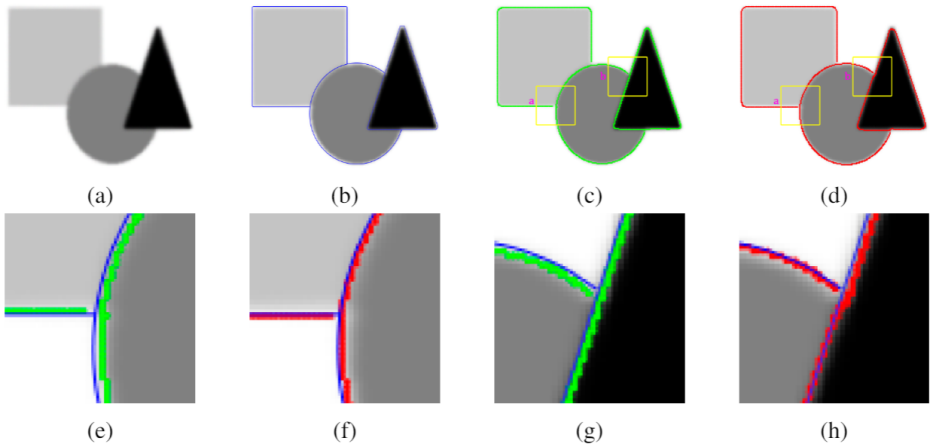

Figure 4.4: Results of applying the proposed method over the segmentation performed by the PCNN model on a synthetic image suffering from blurring effect at the boundaries between regions. (a) original image, (b) ground truth segmentation with the boundaries between regions demarked in blue, (c) PCNN segmentation with the boundaries between regions marked in green and overlapped with the boundaries of the ground truth segmentation, (d) PCNN segmentation after applying the proposed method, with the boundaries between regions marked in red and overlapped with the boundaries of the ground truth segmentation. (e) and (f) zoom-in of the regions labeled as "a" in Figures (c) and (d) respectively. (g) and (h) zoom-in of the regions labeled as "b" in Figures (c) and (d) respectively.

Figure 4.4 shows the results of our algorithm applied to the segmentation performed by the PCNN model on a synthetic image suffering from blurring effect at the boundaries between regions. It can be seen how the boundaries of the PCNN segmentation are closer to the boundaries of the ground truth segmentation after applying our method (Figures 4.4(d), 4.4(f) and 4.4(h)), than before applying it (Figures 4.4(c), 4.4(e) and 4.4(g)), as support the results in Table 4.1.

Figure 4.5 shows the results of our algorithm applied to the segmentation of the Corpus callosum brain structure over an MRI slice. This type of image is strongly affected by noise, as can be seen in the zoom-in of Figure 4.5(a), which difficult the segmentation. In Figure 4.5(g) the green curve encloses the segmentation given by the region growing algorithm. The red curve, Figure 4.5(h), encloses the same region with the improved boundaries. It can be seen how the proposed method has expanded the boundaries of the segmented region, reducing the under segmentation produced by the region growing algorithm, as support the DICE coefficient in Table 4.1. Figure 4.6 shows the results of our algorithm applied to the PCNN segmentation of a natural image. As Figures 4.6(g) and 4.6(h) show, our method improves the boundaries of the PCNN seg-

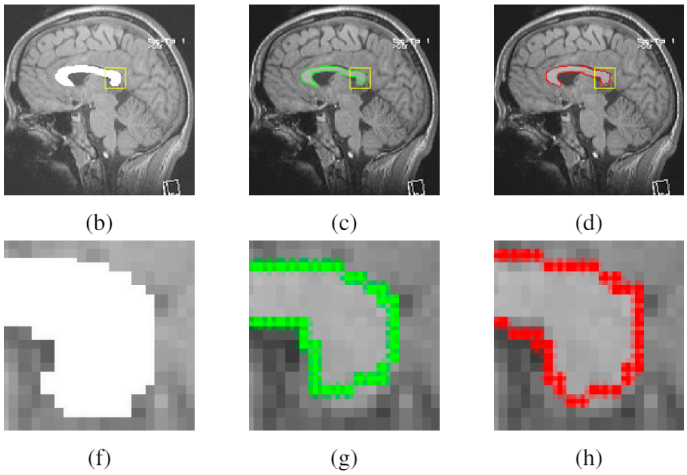

Figure 4.5: Results of applying the proposed method over the segmentation of the Corpus callosum given by the region growing algorithm over an MRI slice. (a) through (d) original image, ground truth segmentation, region growing algorithm segmentation, improved boundary given by the proposed method. (e) through (h) corresponding zoom-in of images (a) through (d).

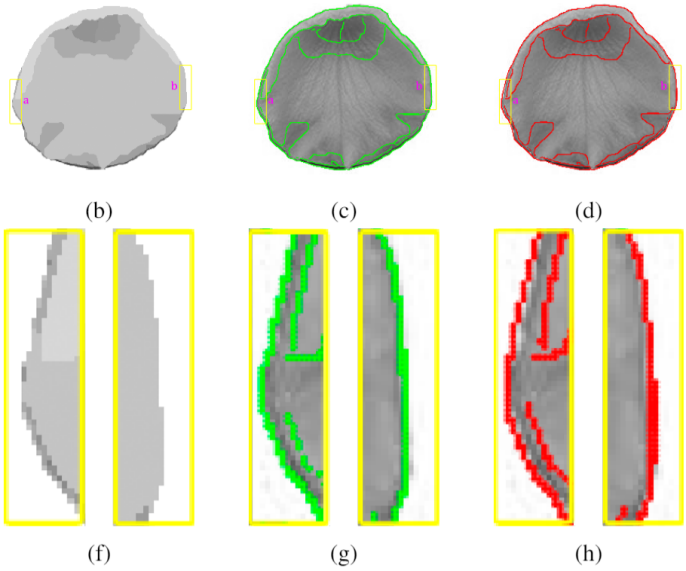

Figure 4.6: Results of applying the proposed method over the PCNN segmentation of a natural image. (a) through (d) original image, PCNN segmentation, PCNN segmentation with boundaries marked in green, improved boundary given by the proposed method. (e) through (h) corresponding zoom-in of images labeled as "a" and "b" in Figures (a) through (d).

mentation (Figure 4.6(f)). The green curve shows the under-segmentation produced by the PCNN, which is partially fixed by the proposed method, Figure 4.6(h). It shows the reduction of under-segmentation.

Table 4.1: Summary of the numerical tests

	DICE	
Image	Original segmentation	After boundary improvement
Synthetic	0.9817	0.9923
MRI	0.7530	0.8649
Natural	0.8261	0.8392

4.4 | Extending to MR images

For simplicity and without loss of generality, the proposed method for improving the edges of the segmented regions was presented in its two-dimensional version; however, since the objective of this chapter is to improve the definition of the edges of the segmented regions of MR images, followed will be presented some brief considerations that must be taken into account to extend the two-dimensional version for processing MR images.

4.4.1 | Volumetric neighborhood

The first aspect to consider is the neighborhood of the voxel. Since voxels will be processed instead of pixels, the neighborhood to consider should be the volume surrounding the voxel. A neighborhood of size 3x3x3 has been selected; However, depending on the noise level of the image, it could be considered a larger neighborhood. Figure 4.7 illustrates the 3x3x3 volumetric neighborhood of a voxel.

Around the volumetric neighborhood will be constructed other sub-volumes of the same size, similar to those constructed around the pixel in the two-dimensional version (see Figure 4.2).

4.4.2 | Dictionary atoms

Similar to the construction of dictionaries in the two-dimensional version, the volumetric neighborhood is converted into a vector by rearranging each column of each plane, of the volumetric neighborhood, one after another. As Figure 4.8 illustrates. This produces a R^{e^3}–vector for each surrounding $e \times e \times e$–volume of the volumetric neighborhood. e

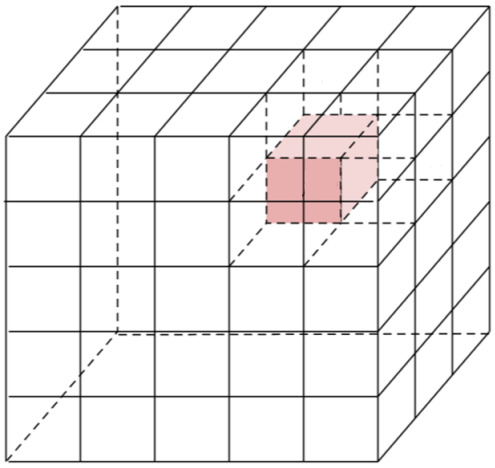

Figure 4.7: Illustration of the volumetric neighborhood of a voxel for extending to MR images the proposed method for improving boundaries

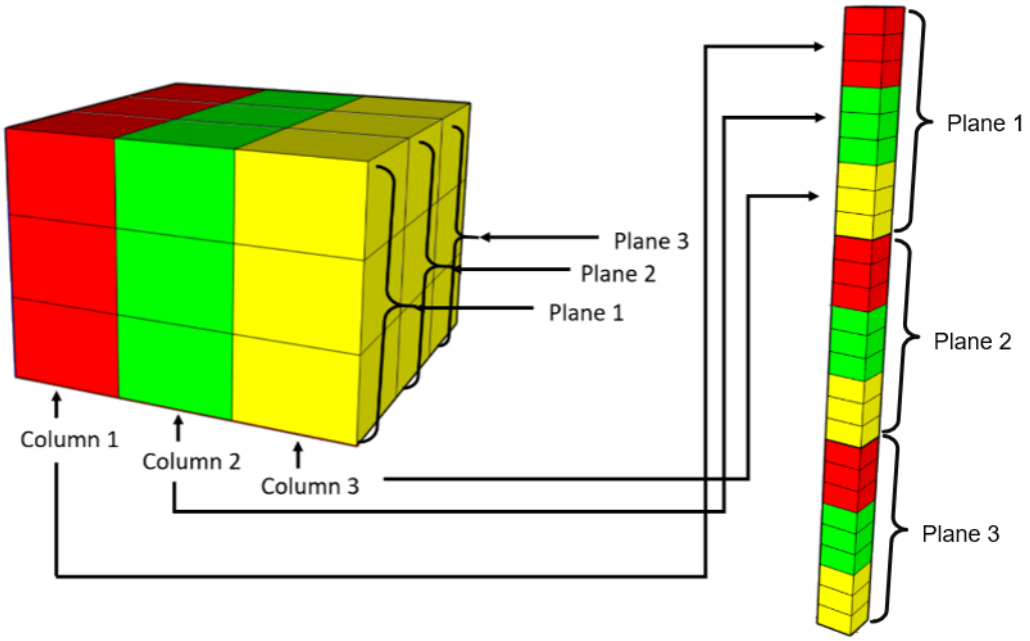

Figure 4.8: Illustrating the conversion of the volumetric neighborhood into a vector

indicates the length (number of voxels) of the sub-volume edge. Once the dictionaries have been constructed, the process continues equal to the two-dimensional version.

4.5 | Conclusions

This chapter presented a method, based on sparse representation, for improving the boundary definition between regions of gray level digital images. It was shown that, under conditions of blurring and noise, it is better to process image patches for detecting edges than using the pixels themselves. As a consequence, it was shown that the proposed method is robust to noise, blurring and outliers. It was also shown how to process patches from a sparse coding approach for improving the boundaries definition of segmented regions.

Previous strategies lead us to improve the definition of boundaries of segmented regions, as shown in Table 4.1, where the DICE of the segmentation increases after applying the proposed method, whereby the second objective of this research is met.

As future work, it is planned to implement an iterative version of this method for moving the boundaries more than one pixel. The method will iterate until reaches a stop criterion. This can be, for example, until the shifting of the boundaries stabilizes, i.e. No boundary moves.

Part 2

This part of the document presents the process performed to establishes the brain characteristics, or possible biomarkers, that can partially explain the why of the behaviour of young offenders. It also presents, how the application of the proposed method for improving the boundaries definition of a segmented MR image reduces the uncertainty of the statistical tests performed to find these biomarkers.

5

On the Road to Identifying Biomarkers of the Offending Brain

This chapter presents an exploration made from brain MR images, to find differences at the level of brain structures, in two groups of individuals; the first, young offenders, and the second, the control group. These differences could be considered as the biomarkers of the behavior of the individuals in the first group. In addition, this chapter presents the application of the proposed method for boundary improvements of segmented regions of brain MR images, in the finding for biomarkers. It is showed how the proposed method reduces the uncertainty in the identification of the biomarkers.

5.1 | Introduction

Theories in neurosciences suggest that some mental illness like anxiety, panic, obsessive-compulsive, depression, bipolar, mood, and the antisocial personality disorder (ASPD), among others, may have their origin or can be explained by alterations in several structures of the limbic system.

The ASPD is one of the most studied disorders. Several works have found some relationships between ASPD and both structural alterations of the limbic system and dysfunctional connections of its substructures. Gordon et al. (2004) suggested that individuals with ASPD have decreased amygdala volume and have lower levels of activation in this structure. Sato et al. (2011) found, instead, that ASPD may be caused by abnormalities in structures of the septo-hippocampal system. They used support vector machines (SVM) and maximum uncertainty linear discrimination analysis (MLDA), with a feature-selection algorithm in order to distinguish psychopaths (15 individuals) from healthy controls (15 individuals) based on the gray matter quantification.

Craig et al. (2009) found that a dysfunction in the connections between the hippocampus and the amygdala may cause the symptoms of the ASPD. This theory is also supported by the research of Tang et al. (2016) and Jiang et al. (2017a). They examined the topological organization in the data from fMRI at rest (R-fMRI) obtained from 32 patients with ASPD and a group of 32 control patients, without ASPD. Individuals with ASPD usually have symptoms of insensitivity, irritability, and impulsivity. This is suggested by previous studies in neuroimaging that indicate that the ASPD could have neurobiological bases, which may involve structural, metabolic and functional anomalies.

Abundant evidence shows that these anomalies are related to the deficit in the frontal and temporal cortices, the insula, the angular gyrus, the parahippocampal and the anterior / posterior cingulate gyrus. The study also showed that people with ASPD have interrupted functional connectivity at rest, as well as an alteration of functional integrity between widely distributed brain regions. Finally the study revealed an aberrant topological organization of the functional brain network in individuals with ASPD; the findings provide novel information about the neuropathological mechanisms of ASPD.

Jiang et al. (2017b), claim that recent research links antisocial personality disorder (ASPD) with abnormalities in the anatomy of the brain; indicating that many are the works that focus on the study of anomalies in gray matter, but little is known about the possible degradation of the microstructure of white matter in people with ASPD, as well as its relationship with impulsivity or risky behaviors. To do this, the white matter is analyzed through diffusion tensor images (DTI): fractionated anisotropy (FA), axial diffusivity (AD) and radial diffusion (RD). This analysis is done in order to find correlations with risky behaviors. It was found that patients with ASPD showed a decreased FA in the white matter that connects the fronto-parietal control network and the frontotemporal network, as well as AD / RD deficiency in tracts of white matter that was not detect by FA. The study found correlations between impulsiveness and risk behaviors in the AD and RD values, but not in the values of FA, including the splenium of the corpus callosum, the left posterior corona radiate / posterior thalamic radiate, the superior longitudinal fasciculus right and the left inferior longitudinal fascicle. What shows that these regions can be potential biomarkers to characterize patients with ASPD.

Gregory et al. (2012) carried out a study using MR images for analyzing brain structures of 50 men. 12 were violent with ASPD and psychopathy (ASPD+P), 20 were violent with ASPD but not psychopathy (ASPD-P) and 18 were healthy people not violent. MR images were used to measure the brain activation associated with the representation of punishment or reward information during a probabilistic response-review task related to an event, and that measurement was evaluated using a standard general linear

model. Individuals with ASPD+P showed discrete regions of increased activation in the posterior cingulate cortex and the anterior insula, in response to punishment for errors during the reverse phase of the task, and decreased activation to all correct responses rewarded in the superior temporal cortex. The authors suggest that this difference between violent patients with ASPD+P and ASPD-P has implications in the causes of these disorders and in the treatment approaches.

Substance use disorders (SUDs) have been also well studied. Schiffer et al. (2011) studied the relationship between changes in the volume of gray matter and lifelong substance use disorders, in order to determine if these alterations are also associated with violent behaviors and/or psychopathies. The study was based on samples of male individuals taken from prisons, forensic hospitals, outpatient and psychiatric services. They compared 12 men with SUDs who showed violent behavior, 12 violent offenders, without SUDs, 13 with SUDs who did not show violent behavior and 14 non-violent without SUDs. The study showed that when comparing non-delinquents with violent offenders, the latter presented a larger volume of gray matter in the amygdala bilaterally, the left nucleus accumbens and right caudate head and less gray matter volume in the left insula. Individuals with SUDs had a smaller gray mass volume in the orbifrontal cortex, the prefrontal cortex, and the premotor cortex. The study concluded that violent behavior is associated with greater gray mass volume in the mesolimbic system and reduced volumes of gray matter in the prefrontal and orbitofrontal cortex.

It is evident that brain alterations may influence the behavior of people at the level of psychopathies or in general terms, mental disorders. However, the behavior of young offenders although is considered a mental health problem, is not considered a mental disorder. Therefore a question arises, are there structural or functional brain alterations that explain the behavior of young offenders? Some work have been focused on this direction.

Cope et al. (2014) carried out a study on young offenders, who committed homicides and were in prison (20 individuals), against a sample of incarcerated but non-homicidal men (135 individuals), plus a control group (21 individuals) for tests. The research involved studying the neuroimaging of such individuals and analyzing them so that patterns can be found in the brain that are related to their homicidal behavior. The study found that young offenders have less gray matter in the temporal lobe than those who did not commit homicide, both those in jail and the control group. In order to be able to classify individuals, a support vector machine (SVM) was used. The results showed that they were 80% accurate in correctly classifying youths who committed serious violent crimes from those who did not. However, these differences can be produced by brain aging. Brain structures from young to adult men may varying significantly.

Liu (2011) proposed a framework of early health risk factors for predicting violence; based on the development of existing theories of criminal behavior and supported by empirical findings, this framework addresses the gaps in the literature of adolescent psychopathology by presenting a new conceptualization of disorders that emphasizes the pre, peri and postnatal periods when the development of the child is critical and opportunities for behavioral and environmental modification are high.

Risk factors that influence negative behavioral outcomes include prenatal and postnatal nutrition, smoking during pregnancy, maternal depression, birth complications, traumatic brain injuries and exposure to lead and child abuse, the author also points out that there is an abundance of literature suggesting that these health risk factors may increase the likelihood of aggressive behavior and juvenile delinquency, adult criminal behavior and / or violence.

More recent research has found that childhood trauma has been associated with long-term effects on prefrontal-limbic gray matter. Paquola et al. (2016). The above suggests that there could be brain differences at the structural or functional level that could influence or even determine the behavior of young offenders. Table 5.1 presents a summary of the reviewed works, highlighting aspects such as the objective of the work, the analysis technique and the biomarker found, among others.

The early identification of the mental health conditions of young offenders, would allow knowing the mental health services that these youths really require for their full recovery. Such an early identification for the categorization of the individuals in question, actually refers to the detection of biomarkers of their condition. However, can these conditions be considered as biomarkers?

According to the technical report of the joint program of the United Nations, the International Labor Organization and the World Health Organization, a biomarker is defined as “Any substance, structure or process that can be measured in the body or its products and influence or predict the incidence of outcome or disease. " These biomarkers must be relevant and valid. Relevance refers to the fact that they must provide information of interest and importance to the public and health authorities. Although validity is a controversial term, it refers to the range of characteristics that constitute the best approximation to truth or falsehood of biomarker. It is more in the sense of the degree of belonging than of simple truth or falsehood. United Nations Environment Programme et al. (2001).

If there are such determining characteristics of the condition of the patients, these should basically be alterations of the brain structures, which could be measured, and which would be of interest to the public and the health authorities, given that they constitute a determining factor of the psycho-social condition of the individual, while

statistically, these alterations have a high degree of validity when characterizing the individual's condition, so according to the previous definition, these characteristics would constitute behavioral biomarkers of the individuals in question.

Early detection of these biomarkers could become a determining factor when it comes to establishing the reformatory treatment to which these individuals should be exposed. This report presents the summary of the exploration carried out on the MR images of two groups of individuals; the first, young offenders, and the second, the control group, looking for biomarkers that determine the behavior of the individuals in the first group.

Table 5.1: Summary of works oriented to establish relationships between brain alterations and metal health problems

Work	**Goal**	**Imaging technique**	**Analysis or Classification Technique**	**Biomarker**	**Functional implications**
Cope et al. (2014)	Differentiate young offenders who committed homicides from those who did not	MRI	Support Vector Machine	Homicide offender present gray matter deficits in bilateral paralimbic regions including the medial and lateral temporal lobes and posterior insula	It is related to the low control of behavior, emotional numbing and impulsiveness, which favors violent attitudes and the greater risk of committing serious crimes
Schiffer et al. (2011)	Differentiate structural brain alterations associated with violent behavior from those associated with substance use disorders	MRI	Statistical analysis	Increased gray matter volume in the amygdala bilaterally, the left nucleus accumbens, and the right caudate head and less gray matter volume in the left insula	Related to violent, aggressive and impulsive behavior. Reduced ability to anticipate punishment. It is associated with psychopathy
Sato et al. (2011)	Identify relations in abnormal structures of the septo-hippocampal system and the ASPD	MRI	Support Vector Machine and Discriminant Analysis	Concentration of gray matter in the right superior temporal sulcus (STS) and lesser degree in the left STS	It is related to alterations in social cognition and emotional processing, additionally little capacity for empathy, morals, compassion, shame, feelings of compliance.

Work	Goal	Imaging technique	Analysis or Classification Technique	Biomarker	Functional implications
Gregory et al. (2012)	Measure the brain activation for distinguishing between men with ASPD+P and men with ASPD-P	MRI	Statistical analysis	Significantly reduced gray matter volumes bilaterally in the anterior rostral prefrontal cortex (Brodmann area 10) and temporal poles (Brodmann area 20/38)	Structures related to the low processing of prosocial emotions, empathy, moral abilities. In general terms, abnormalities in social behavior typical of psychopathy
Jiang et al. (2017a); Tang et al. (2016)	Analyze the relation of the topological organization of the functional brain network and ASPD	R-fMRI	Graph theoretical analysis and Statistical analysis	Altered topological configuration of the functional connectome in the frequency interval of 0.016–0.031Hz. Reduced brain integration and segregation in topological organization of functional brain networks, particularly in the fronto-parietal control network	Associated with little concern for the feelings of others and for social obligations Reduced integration capacity in brain functions, which contributes to disturbances in behavior and cognition

Work	Goal	Imaging technique	Analysis or Classification Technique	Biomarker	Functional implications
Gordon et al. (2004)	Find personality differences in a non-psychiatric population	fMRI	Measure of blood oxygen level–dependent contrast	Increased activation in several subregions of the frontal cortex (primarily right dorsolateral prefrontal cortex), as well as the amygdala when performing emotion recognition tasks	Dysfunction is reflected in emotional tasks that involve affective recognition
Jiang et al. (2017b)	Identify biomarkers of ASPD from white matter abnormalities	DTI	Statistical analysis	Decreased FA in multiple major white matter fiber bundles, which connect the fronto-parietal control network and the fronto-temporal network. AD/RD deficits in some additional white matter tracts not detected by FA	Correlation is identified with risk behavior and impulsivity
Craig et al. (2009)	Relations between abnormalities in a specific amygdala – OFC limbic network and psychopathy	DTI	Statistical analysis	Decrease in white matter tracts (Uncinated fasciculus) between the OFC and the amygdala	Structures related to severe antisocial and criminal behavior, characterized by low respect for social norms and emotional regulation

Table 5.2: Type of crime committed by YOs

Type of crime	Percentage of cases
Homicide attempt	5.7%
Homicide	40%
Theft (qualified or aggravated)	31.4%
Illegal carrying of weapons	17.1%
Extortion	2.9%
Sexual related violence	2.9%

5.2 | Materials and Methods

5.2.1 | Participants

This study included 40 male participants, consisting of 19 young offenders (YOs) and 21 controls (COs). The YOs were recruited from a reformatory school for young male offenders in Barranquilla, Colombia. These individuals had been imprisoned for various reasons, including attempted murder, murder, theft, and illegal possession of weapons, among others (see Table 5.2). COs were recruited from schools located in the same district of residence of YOs.

Recruitment was authorized and assisted by the principals and teachers of the schools. The inclusion criteria for control participants were: (a) gender (male); (b) age (between 15 and 18 years); (c) level of education (less than 12 years of education); and (d) absence of a history of psychiatric or neurological disorders. All participants completed a structured admission interview to rule out psychiatric disorders and ensure that they were not under pharmacological treatment during the assessment. All participants and parents/tutors provided written informed consent in accordance with the Helsinki declaration. The protocol was approved by the Ethics Committee of the Universidad Autónoma del Caribe.

5.2.2 | MR images scanning

A group of 19 YOs and 21 COs were scanned in a $1.5T$ Siemens Magnetom equipped with a standard head coil. The parameters of the T1w images were: TR = 7.9 ms, TE = 3.8 ms, ACQ matrix 220 $\times$ 220 pixels, voxel size 0.5 mm $\times$ 0.5 mm $\times$ 0.5 mm.

5.2.3 | Analysis

The MR images were analyzed by two types of study. The first, Voxel-based morphometry (VBM), driven in the SPM software. The second, which consisted of a processing stage conducted with the volBrain software, from the Polytechnic University of Valencia, and a statistical analysis stage performed with the IBM SPSS software. Each study is detailed below.

5.2.3.1 | Analysis using VBM

The image analysis steps by VBM using the SPM software were performed following the guide "A 12-step user guide for analyzing voxel-wise gray matter asymmetries in statistical parametric mapping (SPM)" Kurth et al. (2015). The T1-weighted images were normalized using the DARTEL algorithm, to reduce the unaccuracy of the captures between subjects. The images were segmented into gray matter, white matter, spinal fluid and non-cerebral tissue. Subsequently, to improve the signal-to-noise ratio and correct registration errors, the segmentations were smoothed by convolution with an 8mm isotropic Gaussian kernel. The model was specified and its estimation was made. Figure 5.1 shows the results obtained with VBM.

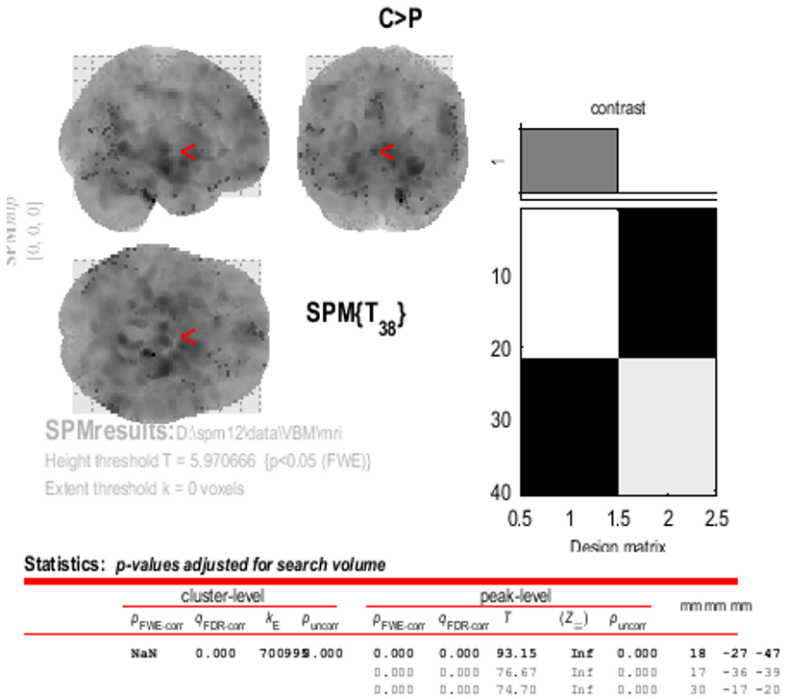

Figure 5.1: Results obtained with VBM

As can be seen in Figure 5.1, the results are inconclusive and, apparently, hint at a methodological error in the treatment of the images, however it was not detected. Other tests were performed with the CAT software with the inclusion of covariates such as the total intracranial volume; however, the results were the same.

5.2.3.2 | Analysis using volBrain and SPSS

Since it is expected to find differences between the brain structures of both groups (YOs and COs), and given that the VBM analysis failed, a second study of the images was performed using the volBrain platform for segmenting the MR images and the IBM SPSS software for analysis of the results.

Processing with volBrain

The volBrain platform consists of a set of software modules, available via the Web, for segmenting brain into its main substructures. volBrain has 4 different pipelines, of which 3 were used to process the images, these were: 1) volBrain, for the segmentation of the brain into gray matter, white matter, cerebrospinal fluid and subcortical structures of the limbic system and basal ganglia. 2) CERES, for the segmentation of the Cerebellum in each of its lobes, and 3) Hips, for the segmentation of the Hippocampus.

The segmentation produced by the volBrain pipeline generates a report that delivers the volume of the structures presented in Table 5.3. A typical report generated by volBrain is presented in Figure 5.2. A partial graphic result is presented in Figure 5.3.

Table 5.3: Brain structures segmented by volBrain

White Matter	Brain	Putamen	Thalamus
Grey Matter	Intracranial Cavity	Globus Pallidus	Hippocampus
Cerebrospinal fluid	Caudate	Lateral ventricles	Amygdala

The segmentation produced by the CERES pipeline generates a report that delivers the volume of the structures presented in Table 5.4. A typical result of a report generated by CERES is presented in Figure 5.4. A partial graphic result is presented in Figure 5.5.

Table 5.4: Cerebellum structures segmented by CERES

Cerebellum	Lobule IV	Lobule Crus I	Lobule VIIIA	Lobule X
Lobule I-II	Lobule V	Lobule Crus II	Lobule VIIIB	
Lobule III	Lobule VI	Lobule VIIB	Lobule IX	

Tissue type	Volume (cm^3/%)
White Matter (WM)	476.44 (38.56%)
Grey Matter (GM)	657.80 (53.24%)
Cerebro Spinal Fluid (CSF)	101.40 (8.21%)
Brain (WM + GM)	1134.24 (91.79%)
Intracranial Cavity (IC)	1235.64 (100.00%)

Structure	Total (cm^3/%)		Right (cm^3/%)		Left (cm^3/%)		Asym.(%)
Cerebrum	968.71 (78.40%)		481.74 (38.99%)		486.97 (39.41%)		-1.0804
	GM	WM	GM	WM	GM	WM	
	553.91 (44.83%)	414.81 (33.57%)	274.67 (22.23%)	207.07 (16.76%)	279.24 (22.60%)	207.73 (16.81%)	
Cerebelum	Total (cm^3/%)		Right (cm^3/%)		Left (cm^3/%)		Asym.(%)
	143.03 (11.58%)		71.05 (5.75%)		71.97 (5.82%)		-1.2923
	GM	WM	GM	WM	GM	WM	
	100.27 (8.11%)	42.76 (3.46%)	49.42 (4.00%)	21.63 (1.75%)	50.85 (4.12%)	21.13 (1.71%)	
Brainstem	Total (cm^3/%)						
	22.52 (1.82%)						

Structure	Total (cm^3/%)	Right (cm^3/%)	Left (cm^3/%)	Asymmetry (%)
Lateral ventricles	3.98 (0.32%)	1.17 (0.09%)	2.81 (0.23%)	-82.5060
Caudate	5.66 (0.46%)	2.80 (0.23%)	2.86 (0.23%)	-1.9726
Putamen	7.26 (0.59%)	3.68 (0.30%)	3.58 (0.29%)	2.8507
Thalamus	10.83 (0.88%)	5.41 (0.44%)	5.43 (0.44%)	-0.3518
Globus Pallidus	1.85 (0.15%)	0.90 (0.07%)	0.95 (0.08%)	-5.2187
Hippocampus	7.89 (0.64%)	3.87 (0.31%)	4.02 (0.33%)	-3.9337
Amygdala	1.08 (0.09%)	0.56 (0.05%)	0.52 (0.04%)	6.0453
Accumbens	0.65 (0.05%)	0.30 (0.02%)	0.35 (0.03%)	-13.4737

Figure 5.2: Text report generated by volBrain

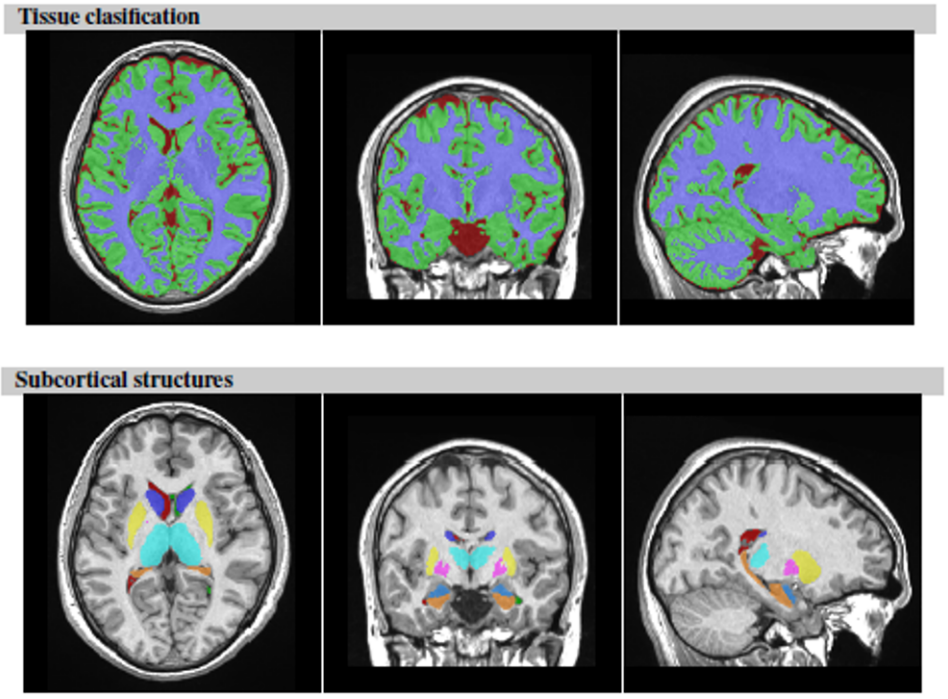

Figure 5.3: Partial graphical report generated by volBrain

Image Information

Orientation	neurological
Scale factor	0.68
SNR	19.55
Total intracranial volume (cm^3)	1242.08

Volumes	**Total (cm^3/%)**	**Right (cm^3/%)**	**Left (cm^3/%)**	**Asym.(%)**
Cerebellum	137.18 (11.0447)	68.51 (5.5158)	68.67 (5.5289)	-0.2388
Lobule I-II	0.14 (0.0112)	0.08 (0.0062)	0.06 (0.0050)	22.4390
Lobule III	1.51 (0.1214)	0.79 (0.0633)	0.72 (0.0581)	8.5317
Lobule IV	4.67 (0.3757)	2.28 (0.1837)	2.39 (0.1921)	-4.4677
Lobule V	8.30 (0.6681)	4.19 (0.3375)	4.11 (0.3306)	2.0719
Lobule VI	19.55 (1.5741)	9.20 (0.7408)	10.35 (0.8334)	-11.7647
Lobule Crus I	27.81 (2.2389)	14.62 (1.1773)	13.19 (1.0617)	10.3259
Lobule Crus II	17.32 (1.3941)	9.11 (0.7338)	8.20 (0.6603)	10.5551
Lobule VIIB	9.32 (0.7507)	4.37 (0.3515)	4.96 (0.3992)	-12.6906
Lobule VIIIA	13.94 (1.1222)	7.01 (0.5642)	6.93 (0.5579)	1.1268
Lobule VIIIB	8.81 (0.7096)	4.26 (0.3426)	4.56 (0.3671)	-6.8966
Lobule IX	9.63 (0.7751)	4.68 (0.3767)	4.95 (0.3984)	-5.5970
Lobule X	1.22 (0.0981)	0.61 (0.0489)	0.61 (0.0492)	-0.6667

Grey matter vol.	**Total (cm^3/%)**	**Right (cm^3/%)**	**Left (cm^3/%)**	**Asym.(%)**
Cerebellum	103.89 (8.3644)	52.08 (4.1931)	51.81 (4.1713)	0.5200
Lobule I-II	0.08 (0.0066)	0.05 (0.0037)	0.04 (0.0029)	33.9038
Lobule III	1.24 (0.0996)	0.66 (0.0529)	0.58 (0.0468)	18.1018
Lobule IV	4.19 (0.3375)	2.04 (0.1643)	2.15 (0.1733)	-7.8716
Lobule V	7.18 (0.5779)	3.55 (0.2856)	3.63 (0.2923)	-3.3992
Lobule VI	17.50 (1.4091)	8.15 (0.6563)	9.35 (0.7528)	-20.2374
Lobule Crus I	22.40 (1.8034)	11.94 (0.9612)	10.46 (0.8422)	19.5001
Lobule Crus II	14.48 (1.1658)	7.81 (0.6287)	6.67 (0.5370)	23.2325
Lobule VIIB	8.00 (0.6439)	3.83 (0.3085)	4.17 (0.3354)	-12.3541
Lobule VIIIA	12.22 (0.9835)	6.01 (0.4839)	6.21 (0.4997)	-4.7479
Lobule VIIIB	7.26 (0.5847)	3.46 (0.2782)	3.81 (0.3065)	-14.2919
Lobule IX	7.79 (0.6269)	3.82 (0.3076)	3.97 (0.3193)	-5.4969
Lobule X	1.18 (0.0952)	0.59 (0.0473)	0.60 (0.0480)	-2.1985

Figure 5.4: Text report generated by CERES

Lobules segmentation

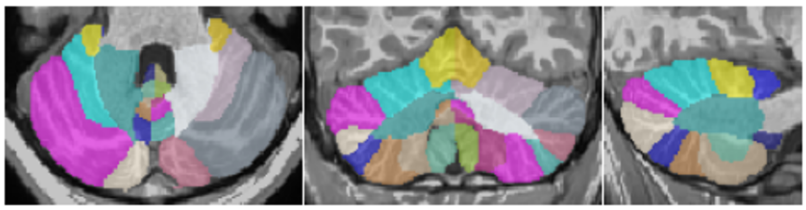

Tissue classification

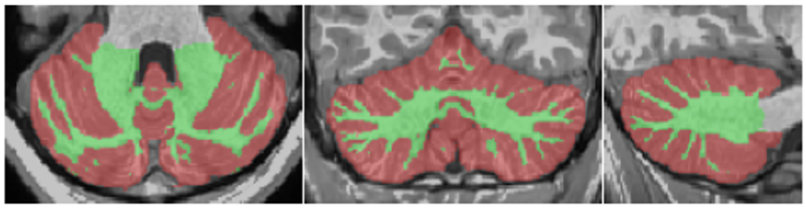

Figure 5.5: Partial graphical report generated by CERES

The Hips pipeline segments the hippocampus. For this purpose, it can use either of two protocols: Kulaga-Yoskovitz and Winterburn. The Kulaga-Yoskovitz provides information on the total volume of the hippocampus and its division into 3 substructures or circuits: CA1-3, CA4-DG and Subiculum. The Winterburn provides information on the total volume of the hippocampus and its division into 5 substructures or circuits: CA1, CA2-CA3, CA4-DG, SR-SL-SM and Subiculum. Samples of the text reports and partial graphics generated by the Hips pipeline, using the Kulaga-Yoskovitz and Winterburn protocols, are presented in Figures5.6 and 5.7, respectively.

Segmentation protocol: Kulaga-Yoskovitz[2]

Volumes[3]	Total (cm^3/%)	Right (cm^3/%)	Left (cm^3/%)	Asym.(%)[4]
Hippocampus	7.45 (0.6032)	3.73 (0.3019)	3.72 (0.3013)	0.2017
CA1-3	4.70 (0.3804)	2.41 (0.1949)	2.29 (0.1855)	4.9327
CA4-DG	0.71 (0.0575)	0.35 (0.0285)	0.36 (0.0290)	-1.9290
Subiculum	2.04 (0.1653)	0.97 (0.0785)	1.07 (0.0867)	-9.9476

Right hippocampus

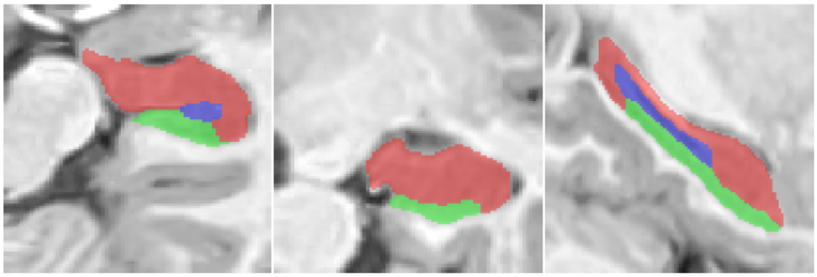

Figure 5.6: Report generated by the Hips pipeline with the Kulaga-Yoskovitz protocol

Segmentation protocol: Winterburn[2]

Volumes[3]	Total (cm^3/%)	Right (cm^3/%)	Left (cm^3/%)	Asym.(%)[4]
Hippocampus	5.29 (0.4284)	2.62 (0.2118)	2.68 (0.2166)	-2.2534
CA1	1.86 (0.1509)	0.92 (0.0746)	0.94 (0.0763)	-2.1592
CA2-CA3	0.36 (0.0291)	0.18 (0.0144)	0.18 (0.0147)	-2.1346
CA4-DG	1.34 (0.1088)	0.68 (0.0554)	0.66 (0.0534)	3.5410
SR-SL-SM	1.06 (0.0860)	0.52 (0.0424)	0.54 (0.0436)	-2.6872
Subiculum	0.66 (0.0535)	0.31 (0.0249)	0.35 (0.0286)	-13.6702

Right hippocampus

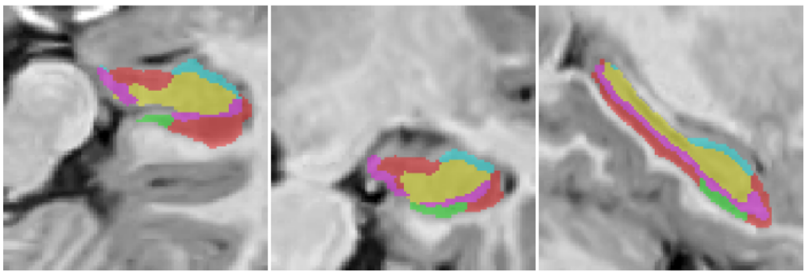

Figure 5.7: Report generated by the Hips pipeline with the Winternburn protocol

Statistical analysis with SPSS

Once the images were processed with the volBrain platform, 30 brain structures were obtained for each MR image, which were analyzed with the IBM SPSS software. Given that it is wanted to analize two groups, YOs and COs, which correspond to independent cross-sectional samples, the best option would be to perform a T-test to establish whether there is a significant difference in the brain structures of both groups; however, the application of such a test is subject to compliance with the assumptions of normality and equality of variances. Therefore, an exploratory analysis was carried out to verify that these assumptions were met. In cases where the aforementioned assumptions were not fulfilled, non-parametric tests were carried out.

Normality tests

Given that a sample of 40 individuals was available, the Kolmogorov-Smirnov (KS) test was applied to determine if the data sets obtained (random variables), from each of the 30 segmented structures, followed a normal distribution . The criterion to determine if the random variables are normally distributed is as follows:

Significance level $\alpha = 0.05$
H_a : The data does not come from a normal distribution
H_0 : The data does come from a normal distribution

If $p \geq \alpha$ we accept H_0. The data come from a normal distribution.

The results of applying the normality test, with the IBM SPSS software to the Globus Pallidus and the Nucleus Accumbens structures, are shown in Table 5.5.

Table 5.5: Normality test applied to the Globus Pallidus and the Nucleus Accumbens structures

	Kolmogorov-Smirnov Test			
	Type	Statistic	Degrees of freedom	Significance level
Globus Pallidus	COs	0,097	21	0.200
	YOs	0,126	19	0.200
Nucleus Accumbens	COs	0,145	21	0.200
	YOs	0,232	19	0.008

As can be seen in Table 5.5, for the Globus Pallidus structure the P value is 0.2 for both groups; therefore, the null hypothesis H_0 is accepted; i.e., it is accepted that the data come from a normal distribution. Similarly, for the Nucleus Accumbens structure, the P

value is 0.008 for the group "YOs" (Young offenders), therefore, the null H_0 hypothesis is rejected; i.e., it is accepted that the data does NOT come from a normal distribution. In general terms, it is accepted that the entire sample (Offenders plus Controls) does not follow a normal distribution. In this case, for the Nucleus Accumbens structure, a non-parametric test was applied to establish if there was a significant difference between the means of the two samples (This will be addressed later).

Table 5.6 shows the summary of the normality tests applied to 10 of the segmented structures.

Table 5.6: Summary of normality tests of 10 of the segmented structures

	P value		Interpretation
	YOs	**COs**	
Hyppocampus	0.2	0.2	Normal
Amygdala	0.039	0.119	Not normal
Lateral ventricles	0.005	0.099	Not normal
Caudate	0.2	0.2	Normal
Putamen	0.2	0.2	Normal
Thalamus	0.2	0.2	Normal
Globus Pallidus	0.2	0.2	Normal
Nucleus Accumbens	0.2	0.008	Not normal
Cerebellum – Lob I-II	0.2	0.2	Normal
Cerebellum – Lob III	0.2	0.2	Normal

Variance equality tests

To verify the assumption of variance equality between groups, the Levene test was used. The decision criteria is as follows:

Significance level $\alpha = 0.05$
H_a : The variances are equal
H_0 : The variances are NOT equal

If $p \geq \alpha$ we accept H_0. The variances of the groups are equal.

Table 5.7 below shows the result of applying the equality of variance test with IBM SPSS software to the Globus Pallidus structure. The P value of 0.961 is higher than the significance level of the test. We accept the null hypothesis H_0; i.e., we accept that the variances of both groups are equal, and therefore, the Student's T-test can be performed to determine whether or not there is a significant difference in the means of the two sam-

ples. In cases where the assumption of homoscedasticity was not met, a non-parametric test was applied.

Table 5.7: Result of applying the Levene test to the Globus Pallidus structure

	Levene test	
	Statistic	Significance level
Globus Pallidus	0.002	0.961

Comparison of means using the Student's T-test

The Student's T-test was applied to the structures that met the assumptions of normality and homoscedasticity. Below is the test design for the Globus Pallidus structure. For structures that meet both assumptions, the design will be the same.

Significance level $\alpha = 0.05$	
H_a :	There is a significant difference between the mean volume of the Globus Pallidus of the YOs and the mean volume of the Globus Pallidus of the COs.
H_0 :	There is NOT a significant difference

If $p < \alpha$ we reject H_0. There is a significant difference between the means of both groups.

Table 5.8 shows the result of applying the T-test to the Globus Pallidus structure. As observed in the in Table 5.8, the P value is 0.028, which is below the established level of significance, therefore, the null hypothesis H_0 is rejected; i.e., We accept that there is a significant difference between the means of both groups. We can say with 95% confidence that there is a significant difference in the volume of the Globus Pallidus of the YOs compared to that of the COs. The Table 5.9 shows the summary of the application of the T-test to the structures that met the assumptions.

Table 5.8: T-test to verify equality of means

	T-test for equality of means		
	Statistic	Degrees of freedom	Significance level
Globus Pallidus	2.291	38	0.028

Table 5.9: T-test to verify equality of means

	T-test result
Hyppocampus	There is no significant difference
Caudate	There is no significant difference
Putamen	There is no significant difference
Thalamus	There is no significant difference
Globus Pallidus	***There is significant difference***
Cerebellum – Lob I-II	There is no significant difference
Cerebellum – Asymmetry Lob I-II	***There is significant difference***
Cerebellum – Lob III	There is no significant difference

For the structures that did not meet the assumptions of normality or equality of variances, a non-parametric test was applied, in these cases, since two independent cross-sectional samples were counted, the Mann-Whitney test was applied.

Comparison of means using the Mann-Whitney test

The brain structures that did not meet the assumptions of normality and equality of variances are listed in Table 5.10. As mentioned above, the non-parametric Mann-Whitney test was applied to these structures. Table 5.11 shows the result of the application of this test to the left Lobe I-II of the Cerebellum. The summary of the application of this test on the other structures is presented in Table 5.12.

Table 5.10: Structures that did not meet the assumptions of normality and / or homoscedasticity

	Assumption not fulfilled
Amygdala	Normality
Lateral Ventricles	Normality
Nucleus Accumbens	Normality
Cerebellum – Left Lobe I-II	Homoscedasticity
Cerebellum – Left Lobe Crus I	Normality
Cerebellum – Right Lobe Crus II	Normality
Cerebellum – Asymmetry Lobe VIIB	Normality
Cerebellum – Lobe VIIIA	Normality
Cerebellum – Asymmetry Lobe VIIIB	Normality
Cerebellum – Asymmetry Lobe V	Normality
Cerebellum – Right Lobe IV	Normality
Cerebellum – Lobe VI	Normality
Cerebellum – Lobe VI	Normality

Table 5.11: Mann-Whitney test applied to the Cerebellum Left Lobe I-II

	Cerebellum Left Lobe I-II
U of Mann-Whitney	115.000
W of Wilcoxon	346.000
Z	-2.289
Significance level	0.022

The P value is 0.022. It indicates that we must reject the null hypothesis H_0; i.e., there is a significant difference between the means of the two groups.

Table 5.12: Summary of the application of the Mann-Whitney test on structures that did not meet the assumptions

	Mann-Whitney test result
Amygdala	There is no significant difference
Lateral Ventricles	There is no significant difference
Nucleus Accumbens	There is no significant difference
Cerebellum – Left Lobe I-II	***There is significant difference***
Cerebellum – Left Lobe Crus I	There is no significant difference
Cerebellum – Right Lobe Crus II	There is no significant difference
Cerebellum – Asymmetry Lobe VIIB	There is no significant difference
Cerebellum – Lobe VIIIA	There is no significant difference
Cerebellum – Asymmetry Lobe VIIIB	There is no significant difference
Cerebellum – Asymmetry Lobe V	There is no significant difference
Cerebellum – Right Lobe IV	There is no significant difference
Cerebellum – Lobe VI	There is no significant difference
Cerebellum – Lobe VI	There is no significant difference

5.2.4 | Discussion

According to the statistical results obtained, there is a significant difference between the mean volume of the Globus Pallidus of the YOs and the mean volume of the Globus Pallidus of the COs. Similarly, there is also a significant difference between the left Lobe I-II (gray matter) of the cerebellum between the YOs and the COs, as well as the mean of the asymmetry index of these structures between both groups. Table 5.13 shows the summary of descriptive statistics of these structures.

According to the results presented in Table 5.13, the average volume of the Globus Pallidus of the YOs is 6.36% lower than the average volume of the Globus Pallidus of

Table 5.13: Summary of measures of the structures that present significant differences between both groups

	YOs(μ)	COs(μ)
Globus Pallidus	0,149378294421*	0,159520*
Cerebellum left Lobe I-II (Gray matter)	0,002905*	0,00227699*
Asymmetry of the Lobe I-II	16,14958421^{+}	44,49972381^{+}

*Measurements are relative to the total intracranial volume
$^{+}$ Asymmetry depends on the right and the left volume of the structure

the COs. According to recent studies [16], the efferences of this structure of the basal ganglia contain the main neurotransmitter γ-aminobutyric acid (GABA), which is inhibitory in nature. Similarly, according to Table 5.13, there is also a marked difference in the gray matter volume of the left Lobe I-II of the two groups. The cerebellum left Lobe I-II of YOs is 27% larger compared to that of the COs. This structure has been related, according to recent research [17], with emotional associative learning aspects. It can be quickly related that, the decrease in gray matter of Globus Pallidus, in turn decreases its inhibition capacity, and likewise, the marked increase in the left Lobe I-II of the cerebellum, increases the need for emotion of these individuals. Therefore, it can be thought that, when these two alterations occur simultaneously in an individual, it could become an explanatory factor for the behavior of such individuals.

This is only an initial exploration; however, the verification of these possible biomarkers could be a starting point that would help determine the most appropriate treatments for the YOs in favor of their full recovery. Based on these results, next section go further and propose an indicator of this biomarker

5.3 | Biomarker of the offending brain

Considering that, in the previous results, there is an inverse relationship between the variations of the brain structures that make the difference between YOs and COs; more especiffically, in the YOs it is simultaneously presented that the volume of the Globus Pallidus is less than that of the COs, while the volume of the left Lobe I-II of the cerebellum is greater than that of the COs, this could be thought as a biomarker of the offending behavior. Therefore an indicator of this biomarker should be defined from these two structures, and should exploit theirs inverse relationship. But, before defining this indicator, let us define a random variable from which such indicator will be defined.

This random variable GPLL is define accoridng to Equation 5.1.

$$\text{GPLL} = \frac{\text{Vol}_{LLI-II}}{\text{Vol}_{GP}} \tag{5.1}$$

Where Vol_{LLI-II} is the gray matter volume of the left Lobe I-II of the cerebellum, and Vol_{GP} is the volume of the Globus Pallidus. The assumptions of normality and equality of variances of the new variable will now be verified before defining the indicator of the biomarker. Table5.14 shows the result of the KS-Test.

Table 5.14: Normality test applied to the GPLL variable

	Kolmogorov-Smirnov Test			
	Type	Statistic	Degrees of freedom	Significance level
GPLL	COs	0,122	21	0.200
	YOs	0,103	19	0.200

The P value is 0.2, therefore we accept the assumption of normality. The homoscedasticity assumption will now be verified by the Levene test (See Table 5.15).

Table 5.15: Result of applying the Levene test to the GPLL random variable

Levene test		
	Statistic	Significance level
GPLL	5.153	0.029

The homoscedasticity assumption is not fulfilled, therefore, it will be verified if there is significant difference between the two groups, on this variable, using the Mann-Whitney test (See Table 5.16).

Table 5.16: Mann-Whitney test applied to the GPLL random variable

	GPLL
U of Mann-Whitney	93.000
W of Wilcoxon	324.000
Z	-2.884
Significance level	0.004

The P value is 0.004, therefore the existence of a significant difference between the

two groups is verified. We proceed to define the indicator according to Equation 5.2

$$\text{OBB} = \frac{\text{GPLL}}{mean(\text{GPLL}_{COs})} \tag{5.2}$$

Where OBB is the proposed indicator of offending behavior, $mean(\cdot)$ is the mean and GPLL_{COs} is the set of values corresponding to the variable GPLL of the COs. Values of this indicator greater than one (1) are related to individuals with offending behavior.

5.4 | Conclusions

This chapter presented an exploration in the pursuit of finding biomarkers related to the bahavior of YOs. It was found that some brain structures of YOs present alterations in the volume of gray matter. In general terms, the YOs have a decrease about 6.36% of the volume of the Globus Pallidus brain structure, in addition to present an increase about 27% of the gray matter volume in the Lobe I-II of the cerebellum.

Since this alterations are only presented by the YOs, could constitute a determinant factor of their behavior. This description allows us to achieve the third objective of this research; i.e, the description of the alterations of some brain structures related to the offending behavior.

This could be considered a biomarker; however, before making this conclusion, more tests should be carry out on a larger sample.

6

Applying the proposed Framework

This chapter presents the application of the proposed framework on the discovery of the biomarkers of the offending brain. The previous chapter presented an initial exploration which found some important differences in the studied subjects. However, there is some uncertainty around the differences found. This chapter shows how the application of the proposed framework reduces such uncertainty. Given that the tool used to carry out the initial exploration is a closed platform that does not allow intervention, the proposed method for denoising MR images could not be applied. Only the method for improving the boundaries of segmented regions could be applied. Below it is presented the application of this method, and the indirect measurement of its results.

6.1 | Applying boundary improvement

The previous chapter presented the results of the statistical analysis of the brain structures of the two groups of individuals under study, the Yos, and the COs. However, the data that gave rise to this analysis were not presented; since this chapter will show the numerical values of the structures that showed significant differences between YOs and COs, before (see Table 6.1) and after (see Table 6.2) the application of the edge improvement method presented in Chapter 4. The application of the method for improving the boundaries between regions, basically consist of re-processing the results of volBrain, which eventually could modify the boundaries between regions.

The values in Tables 6.1 and 6.2 are relatives to total intracranial volume. The column "Globus Pallidus" refers to the volume of the Globus Pallidus. The column "Left Lobe I.II (GM)" refers to the volume of the gray matter of lobes I and II of the cerebellum. The values presented in Table 6.2 are slightly different from values presented in Table 6.1, this is because the boundaries enhancement method, when applied to a given

segmentation, eventually moves the edges one voxel in or one voxel out of the structure, slightly changing its volume.

A statistical test was applied to these new values to verify if the results obtained when applying the edge improvement method have significant differences with respect to those obtained with volBrain. Since the samples of the Globus Pallidus structure come from a Normal distribution, and met the criterium of Homocedasticity as presented in the previous chapter (see Table 5.5 and Table 5.7), the existence of a difference between the means of both results was verified by means of a Student's T-test. As can be seen in Table 6.3, the P-value of the test is 0.9928, so it is verified that there is no significant difference between both results.

Now, when applying the Student's T-test to the data of the Globus Pallidus structure obtained after applying the method for improving the boundaries between regions, on the volBrain results, it is corroborated that there is a significant difference between the YOs and COs; However, according to Table 6.4 the P-value is 0.0161, which is less than the P-value obtained from the values of this structure before applying the method for improving the boundaries between regions (See Table 5.5). This suggests that there is possibly a more pronounced difference in the volume of the Globus Pallidus structure between YOs and COs than there was initially.

A similar procedure was carried out on results of the left lobe I and II of the cerebellum. Given the samples of the left lobe I and II of the cerebellum do not met the criterium of Homocedasticity as presented in the previous chapter (see Table 5.10), the existence of a difference between the means of the values of the left lobe I and II of the cerebellum, before and after applying the method for improving boundaries, was verified by means of a Mann-Whitney test. As can be seen in Table 6.5, the P-value of the test is 0.9578, so it is verified that there is no significant difference between both results.

Now, when applying the Mann-Whitney T-test to the data of the left lobe I and II of the cerebellum obtained after applying the method for improving the boundaries between regions, on the volBrain results, it is corroborated that there is a significant difference between the YOs and COs; However, according to Table 6.6 the P-value is 0.0172, which is less than the P-value obtained from the values of this structure before applying the method for improving the boundaries between regions (See Table 5.11). This again suggests that there is possibly a more pronounced difference in the volume of the left lobe I and II of the cerebellum between YOs and COs than there was initially.

Table 6.1: Numerical values of the structures that showed significant differences between YOs and COs, before applying the method for improving region boundaries

Subject	Type	Globus Pallidus	Left Lobe I-II (GM)
1	CO	0,149857879	0,002943000
2	CO	0,178720515	0,002588100
3	CO	0,127174294	0,001258400
4	CO	0,154255038	0,002011600
5	CO	0,162453683	0,001864900
6	CO	0,150807288	0,001681200
7	CO	0,164807886	0,001710400
8	CO	0,147376593	0,002124200
9	CO	0,155343814	0,002117100
10	CO	0,173889902	0,004450000
11	CO	0,148459036	0,002268200
12	CO	0,162728568	0,002009000
13	CO	0,166211957	0,002460700
14	CO	0,171237409	0,002141400
15	CO	0,168890779	0,002910300
16	CO	0,15374318	0,001559700
17	CO	0,191883666	0,001700800
18	CO	0,160885925	0,002402200
19	CO	0,14026678	0,002406000
20	CO	0,164200375	0,002661500
21	CO	0,156723811	0,002548000
22	YO	0,150648412	0,001354300
23	YO	0,157945544	0,003666000
24	YO	0,157590373	0,001784200
25	YO	0,151453699	0,003138900
26	YO	0,16902229	0,002742600
27	YO	0,116307454	0,002611200
28	YO	0,13024043	0,001880100
29	YO	0,163940195	0,004909000
30	YO	0,155358965	0,001871800
31	YO	0,167613934	0,004595700
32	YO	0,147656713	0,002425700
33	YO	0,155131449	0,003449300
34	YO	0,14731349	0,003175100
35	YO	0,152454998	0,002773300
36	YO	0,1312319	0,003991800
37	YO	0,13186048	0,002443000
38	YO	0,14346912	0,002070300
39	YO	0,145066481	0,002494600
40	YO	0,163881667	0,003814900

Table 6.2: Numerical values of the structures that showed significant differences between YOs and COs, after applying the method for improving region boundaries

Subject	Type	Globus Pallidus	Left Lobe I-II (GM)
1	1	0,147565467	0,0029457
2	1	0,178333920	0,0025562
3	1	0,127381557	0,0012401
4	1	0,156488649	0,0019994
5	1	0,163847558	0,0018026
6	1	0,146026401	0,0016582
7	1	0,165840588	0,0016798
8	1	0,153202906	0,0020749
9	1	0,158729778	0,0020752
10	1	0,178442755	0,0044487
11	1	0,154712356	0,0023304
12	1	0,164102007	0,0020509
13	1	0,170832197	0,0024052
14	1	0,174957613	0,0021058
15	1	0,166156449	0,0029712
16	1	0,153070014	0,0016010
17	1	0,195810233	0,0016652
18	1	0,156192957	0,0024568
19	1	0,134586943	0,0023893
20	1	0,162447611	0,0026431
21	1	0,155096789	0,0025740
22	2	0,155502625	0,0013980
23	2	0,159725572	0,0036377
24	2	0,165850081	0,0018837
25	2	0,150414205	0,0031452
26	2	0,154601811	0,0027995
27	2	0,119356781	0,0025865
28	2	0,136979617	0,0019966
29	2	0,167539553	0,0049172
30	2	0,145588837	0,0019130
31	2	0,158613577	0,0045437
32	2	0,156936399	0,0024572
33	2	0,148040694	0,0034145
34	2	0,138143483	0,0031400
35	2	0,152225562	0,0027161
36	2	0,140231511	0,0039757
37	2	0,133390649	0,0024135
38	2	0,137979087	0,0021252
39	2	0,150326523	0,0024497
40	2	0,160972211	0,0037517

Table 6.3: T-test to verify equality of means between the values of the Globus Pallidus structure before and after applying the method for boundary improvement

T-test for equality of means			
	Statistic	Degrees of freedom	Significance level
Globus Pallidus	-0.0615	78	0.9928

Table 6.4: T-test to verify the existence of a significant difference in the Globus Pallidus structure between YOs and COs after applying the bondary improvement method

T-test for equality of means			
	Statistic	Degrees of freedom	Significance level
Globus Pallidus	2.5194	38	0.0161

Table 6.5: Mann-Whitney-test to verify equality of means between the values of the Left Lobe I and II of the cerebellum before and after applying the method for boundary improvement

	Cerebellum Left Lobe I-II
W of Wilcoxon	1614
Z	-0.0529
Significance level	0.9578

Table 6.6: Mann-Whitney-test to verify the existence of a significant difference in the the Left Lobe I and II of the cerebellum between YOs and COs after applying the bondary improvement method

	Cerebellum Left Lobe I-II
W of Wilcoxon	342
Z	-2.3834
Significance level	0.0172

6.2 | Conclusion

This chapter presented the results of applying the method for improving region boundaries on the segmentation results of the volBrain platform. Chapter 4 presented numerical results of this method, showing an improving on segmentation boundaries. This chapter, on the other hand, did not show numerical results but an indirect measurement of its quality, because the ground truth segmentation of the subjects is not available.

The results obtained after applying the edge improvement method are very similar to those obtained with volBrain. This is confirmed by statistical tests, which indicate that there is no significant difference in the results. However, the results obtained after applying the edge improvement method show that the uncertainty in accepting the differences between the YOs and the COs is reduced after applying this method, since the P-value of the statistical tests decreased after the application of the method, going from 0.028 to 0.0161 for the Globus Pallidus, and from 0.022 to 0.0172 for the lobe I-II of the cerebellum.

Given that the ground truth segmentation of the subjects is not available, it cannot be concluded that the results obtained in the segmentation after applying this method, are better than those obtained without applying them, since the results are statistically the same; but they hint that, eventually, its application may yield greater precision when it comes to establishing small differences at the structural level, as is the case of this study.

It is necessary to perform more tests and counting on the ground truth segmentation, to quantify the contribution of this method on the identification of biomarkers; however, the results until now obtained are promising.

References

Adams, R. and Bischof, L. (1994). Seeded region growing. *IEEE Transactions on Pattern Analysis and Machine Intelligence*, 16(6):641–647.

Aharon, M., Elad, M., and Bruckstein, A. M. (2006a). The k-svd: an algorithm for designing overcomplete dictionaries for sparse representation. *IEEE Transactions On Signal Processing*, 54(11):4311–4322.

Aharon, M., Elad, M., and Bruckstein, A. M. (2006b). On the uniqueness of overcomplete dictionaries, and a practical way to retrieve them. *Journal of Linear Algebra and Applications*, 416:48–67.

Aja-Fernandez, S. and Tristan-Vega, A. (2013). A review on statistical noise models for magnetic resonance imaging. Technical Report LPI, TECH-LPI2013-01, Universidad de Valladolid.

Aja-Fernández, S., Pieciak, T., and Vegas-Sánchez-Ferrero, G. (2015). Spatially variant noise estimation in mri: A homomorphic approach. *Medical Image Analysis*, 20(1):184–197.

Ashburner, J. and Friston, K. J. (2005). Unified segmentation. *NeuroImage*, 26(3):839–851.

Badrinarayanan, V., Kendall, A., and Cipolla, R. (2017). Segnet: A deep convolutional encoder-decoder architecture for image segmentation. *IEEE Transactions on Pattern Analysis and Machine Intelligence*, 39(12):2481–2495.

Bao, C. and Ji, H. (2016). Dictionary learning for sparse coding: Algorithms and convergence analysis. *IEEE Transactions on Pattern Analysis and Machine Intelligence*, 38(37):1356–1369.

Baselice, F., Ferraioli, G., Pascazio, V., and Sorriso, A. (2017). Bayesian mri denoising in complex domain. *Magnetic Resonance Imaging*, 38:112–122.

Benou, A., Veksler, R., Friedman, A., and Riklin, R. T. (2017). Ensemble of expert deep neural networks for spatio-temporal denoising of contrast-enhanced mri sequences. *Medical Image Analysis*, 42:145–159.

Bhujle, H. V. and Vadavadagi, B. H. (2019). Nlm based magnetic resonance image denoising – a review. *Biomedical Signal Processing and Control*, 47:252–261.

Biomarkers Definitions Working Group (2001). Biomarkers definition workgroup, biomarkers and surrogate endpoints: preferred definitions and conceptual framework. *Clinical Pharmacology and Therapeutics*, 69(3):89–95.

Biswal, B. B., Yetkin, F. Z., Haughton, V. M., and Hyde, J. (1995). Functional connectivity in the motor cortex of resting human brain using echo-planar mri. *Magnetic Resonance in Medicine*, 34(4):537–541.

Blair, R. J. R., Colledge, E., and Mitchell, D. G. V. (2001). Somatic markers and response reversal: Is there orbitofrontal cortex dysfunction in boys with psychopathic tendencies? *Journal of Abnormal Child Psychology*, 29(6):499–511.

Bloch, F. (1946). Nuclear induction. *Physical Review*, 70(7-8):460–474.

Bloch, F., Hansen, W. W., and Packard, M. (1946). The nuclear induction experiment. *Physical Review*, 70(7-8):474 – 480.

Bosboom, J., Stoffers, D., Stam, C., van Dijk, B., Verbunt, J., Berendse, H., and Wolters, E. (2006). Resting state oscillatory brain dynamics in parkinson's disease: An meg study. *Clinical Neurophysiology*, 117(11):2521–2531.

Buades, A., Coll, B., and Morel, J.-M. (2005a). A non-local algorithm for image denoising. In *Proceedings of the 2005 IEEE Computer Society Conference on Computer Vision and Pattern Recognition (CVPR'05)*, pages 60–65, San Diego, CA, USA.

Buades, A., Coll, B., and Morel, J.-M. (2005b). A review of image denoising algorithms, with a new one. *Multiscale Modeling and Simulation: A SIAM Interdisciplinary Journal, Society for Industrial and Applied Mathematics*, 4(2):490–530.

Buades, A., Coll, B., and Morel, J.-M. (2011). Non-local means denoising. *Image Processing On Line*, 1:208–212.

Budrys, T., Veikutis, V., Lukosevicius, S., Gleizniene, R., Monastyreckiene, E., and Kulakiene, I. (2018). Artifacts in magnetic resonance imaging: how it can really affect diagnostic image quality and confuse clinical diagnosis? *Journal of Vibroengineering*, 20(2).

Canny, J. F. (1983). *Finding Edges and Lines in Images*. Massachusetts Institute of Technology Publications, Cambridge, Massachusetts.

Chang, H.-H., Li, C.-Y., and Gallogly, A. H. (2018). Brain mr image restoration using an automatic trilateral filter with gpu-based acceleration. *IEEE Transactions on Biomedical Engineering*, 65(2):400–413.

Chen, C.-L. and Tai, C.-L. (2010). Adaptive fuzzy color segmentation with neural network for road detections. *Engineering Applications of Artificial Intelligence*, 23(3):400–410.

Cocosco, C. A., Kollokian, V., Kwan, R. K. S., and Evans, A. C. (1997). Brainweb: Simulated brain database. https://brainweb.bic.mni.mcgill.ca/.

Cope, L. M., Ermer, E., Gaudet, L. M., Steele, V. R., Eckhardt, A. L., Arbabshirani, M. R., Caldwell, M. F., Calhoun, V., and Kiehl, A. K. (2014). Abnormal brain structure in youth who commit homicide. *NeuroImage: Clinical*, 4:800–807.

Coupé, P. (2019). https://sites.google.com/site/pierrickcoupe/softwares.

Coupé, P., Yger, P., Prima, S., Hellier, P., Kervrann, C., and Barillot, C. (2008). An optimized blockwise nonlocal means denoising filter for 3-d magnetic resonance images. *IEEE Transactions on Medical Imaging*, 27(4):425–441.

Craig, M. C., Catani, M., Deeley, Q., Latham, R., Daly, E., Kanaan, R., Picchioni, M., McGuire, P. K., Fahy, T., and Murphy, D. G. (2009). Altered connections on the road to psychopathy. *Molecular Psychiatry*, 14(10):946–953.

Cufí, X., Muñoz, X., Freixenet, J., and Martí, J. (2003). A review of image segmentation techniques integrating region and boundary information. *Advances in Imaging and Electron Physics*, 120:1–39.

Dabov, K., Foi, A., Katkovnik, V., and Egiazarian, K. (2006). Image denoising with block-matching and 3D filtering. In *Image Processing: Algorithms and Systems, Neural Networks, and Machine Learning*, volume 6064, pages 354 – 365. International Society for Optics and Photonics, SPIE.

del Fresno, M., Vénere, M., and Clausse, A. (2009). A combined region growing and deformable model method for extraction of closed surfaces in 3d ct and mri scans. *Computerized Medical Imaging and Graphics*, 33(5):369–376.

Despotović, I., Goossens, B., and Philips, W. (2015). Mri segmentation of the human brain: Challenges, methods, and applications. *Computational Intelligence Techniques in Medicine*, 2015.

Dong, B., Jin, R., and Weng, G. (2019). Active contour model based on local bias field estimation for image segmentation. *Signal Processing: Image Communication*, 78:187–199.

Dong, W., Shi, G., and Li, X. (2008). Efficient nonlocal-means denoising using the svd. In *2008 15th IEEE International Conference on Image Processing*, pages 1732–1735, San Diego, CA, USA.

Dong, W., Shi, G., and Li, X. (2013). Nonlocal image restoration with bilateral variance estimation: A low-rank approach. *IEEE Transactions on Image Processing*, 22(2):700–711.

Duda, R. and Hart, P. (1973). *Pattern Classification and Scene Analysis*. John Wiley and Sons, New York.

Eckart, C. and Young, G. (1936). The approximation of one matrix by another of lower rank. *Psychometrika*, 1:211–218.

Efron, B., Hastie, T., Johnstone, I., and Tibshirani, R. (2004). Least angle regression. *The Annals of Statistics*, 32(2):407–499.

Elad, M. and Aharon, M. (2006). Image denoising via sparse and redundant representations over learned dictionaries. *IEEE Transactions on Image Processing*, 15(15):3736–3745.

Elster, A. D. (2020). Questions and answers in mri. http://mriquestions.com/partial-volume-effects.html. [Web; accessed on 04-18-2020].

Erasmus, L. J., Hurter, D., Naude, M., Kritzinger, H. G., and Acho, S. (2004). A short overview of mri artefacts. *South African Journal of Radiology*, pages 13–17.

Fan, L., Zhang, F., Fan, H., and Zhang, C. (2019). Brief review of image denoising techniques. *Visual Computing for Industry, Biomedicine, and Art*, 2(7):1–12.

Fingelkurts, A. A., Fingelkurts, A. A., and Kähkönen, S. (2002). Functional connectivity in the brain - is it an elusive concept? *Neuroscience and Biobehavioral Reviews*, 28(8):241–550.

Fitzgerald, R. (2001). Error in radiology. *Clinical Radiology*, 56:938–946.

Foi, A. (2011). Noise estimation and removal in mr imaging: The variance-stabilization approach. In *IEEE International Symposium on Biomedical Imaging: From Nano to Macro*, pages 1809–1814, Chicago, IL, USA.

Friston, K. J. (2009). Modalities, modes, and models in functional neuroimaging. *Science*, 326(5951):399–403.

Gonzalez, R. C. and Woods, R. E. (2017). *Digital Image Processing 3rd edition*. Pearson, 3 edition.

Gordon, H. L., Baird, A. A., and End, A. (2004). Functional differences among those high and low on a trait measure of psychopathy. *Biological Psychiatry*, 56(7):516–521.

Gregory, S., D. ffytche, A. Simmons, V. K. M. H. S. H., and Blackwood, N. (2012). The antisocial brain: psychopathy matters. *Archives of General Psychiatry*, 69(9):962–972.

Gudbjartsson, H. and Patz, S. (1995). The rician distribution of noisy mri data. *Magnetic Resonance in Medicine*, 34(6):910–914.

Hao, Y., Wang, T., Zhang, X., Duan, Y., Yu, C., Jiang, T., and Fan, Y. (2014). Local label learning (lll) for subcortical structure segmentation: Application to hippocampus segmentation. *Human Brain Mapping*, 35:2674–2697.

He, F., Fu, C., Shao, H., and Teng, J. (2019). An image segmentation algorithm based on double-layer pulse-coupled neural network model for kiwifruit detection. *Computers Electrical Engineering*, 79.

Henderson, G., Ifeachor, E., Hudson, N., Goh, C., Outram, N., Wimalaratna, S., Percio, C. D., and Vecchio, F. (2006). Development and assessment of methods for detecting dementia using the human electroencephalogram. *IEEE Transactions on Biomedical Engineering*, 53(8):1557 – 1568.

Hong, H., Zhang, L., Xie, F., Zhuang, R., Jiang, D., Liu, H., Li, J., Yang, H., Zhang, X., Nie, L., and Li, Z. (2019). Rapid one-step 18f-radiolabeling of biomolecules in aqueous media by organophosphine fluoride acceptors. *Nature Communications*, 10:1–7.

Hore, A. and Ziou, D. (2010). Image quality metrics: Psnr vs. ssim. In *20th International Conference on Pattern Recognition*, pages 2366–2369, Istanbul, Turkey.

Horwitz, B. (2003). The elusive concept of brain connectivity. *Neuroimage*, 19(2):466–470.

Hou, Z. (2003). Adaptive singular value decomposition in wavelet domain for image denoising. *Pattern Recognition*, 36(8):1747–1763.

Hu, J., Zhou, J., and Wu, X. (2016). Non-local mri denoising using random sampling. *Magnetic Resonance Imaging*, 34(7):990–999.

Jiang, D., Dou, W., Vosters, L., Xu, X., Sun, Y., and Tan, T. (2018). Denoising of 3d magnetic resonance images with multi-channel residual learning of convolutional neural network. *Japanese Journal of Radiology*, 36(9):566–574.

Jiang, W., Shi, F., Liao, J., Liu, H., Wang, T., Shen, C., Shen, H., Hu, D., Wang, W., and Shen, D. (2017a). Disrupted functional connectome in antisocial personality disorder. *Brain Imaging and Behavior*, 11(4):1071–1084.

Jiang, W., Shi, F., Liu, H., Li, G., Ding, Z., Shen, H., Shen, C., Lee, S.-W., Hu, D., Wang, W., and Shen, D. (2017b). Reduced white matter integrity in antisocial personality disorder: A diffusion tensor imaging study. *Scientific Reports*, 7(43002):1–11.

Kahali, S., Adhikari, S. K., and Sing., J. K. (2017). A combined region growing and deformable model method for extraction of closed surfaces in 3d ct and mri scans. *Applied Soft Computing*, 60(C):213 – 327.

Kang, M., Jung, M., and Kang, M. (2018). Rician denoising and deblurring using sparse representation prior and nonconvex total variation. *Journal of Visual Communication and Image Representation*, 54:80–99.

Khedr, W., Ali, R., and Ismail, F. (2012). Image denoising using k-svd algorithm based on gabor wavelet dictionary. *International Journal of Computer Applications*, 59(2):30–33.

Kidoh, M., Shinoda, K., Kitajima, M., Isogawa, K., Nambu, M., Uetani, H., Morita, K., Nakaura, T., Tateishi, M., Yamashita, Y., and Yamashita, Y. (2019). Deep learning based noise reduction for brain mr imaging: Tests on phantoms and healthy volunteers. *Magnetic Resonance in Medical Sciences*, pages 1–12.

Kimpe, T. and Tuytschaever, T. (2007). Increasing the number of gray shades in medical display systems how much is enough? *Journal of Digital Imaging*, 20(4):422–432.

Klosowski, J. and Frahm, J. (2017). Image denoising for real-time mri. *Magnetic Resonance in Medicine*, 77(3):1340–1352.

Koch, M. A., Norris, D. G., and Hund-Georgiadis, M. (2002). An investigation of functional and anatomical connectivity using magnetic resonance imaging. *Neuroimage*, 16(1):241–550.

Kong, Z., Han, L., Liu, X., and Yang, X. (2018). A new 4-d nonlocal transform-domain filter for3-d magnetic resonance images denoising. *IEEE Transactions on Medical Imaging*, 37(4):941–954.

Kurth, F., Gaser, C., and Luders, E. (2015). A 12-step user guide for analyzing voxel-wise gray matter asymmetries in statistical parametric mapping (spm). *Nature Protocols*, 10(2):293–304.

L. Wang, F. Shi, W. L. J. H. G. and Shen, D. (2011). Automatic segmentation of neonatal images using convex optimization and coupled level sets. *NeuroImage*, 58(3):805–817.

Leal, N., Moreno, S., and Zurek, E. (2019). Simple method for detecting visual saliencies based on dictionary learning and sparse coding. In *14th Iberian Conference on Information Systems and Technologies (CISTI)*, pages 1–5, Coimbra, Portugal.

Lei, B. and Fan, J. (2019). Image thresholding segmentation method based on minimum square rough entropy. *Applied Soft Computing*, 84.

Li, C., Xu, C., Gui, C., and Fox, M. D. (2010). Distance regularized level set evolution and its application to image segmentation. *IEEE Transactions on Image Processing*, 19(12):3243–3254.

Li, H., He, X., Tao, D., Tang, Y., and Wang, R. (2018). Joint medical image fusion, denoising and enhancement via discriminative low-rank sparse dictionaries learning. *Pattern Recognition*, 79:130–146.

Li, Z., He, H., Yin, Z., and Chen, F. (2014). A color-gradient patch sparsity based image inpainting algorithm with structure coherence and neighborhood consistency. *Signal Processing*, 99:116–128.

Liu, J. (2011). Early health risk factors for violence: Conceptualization, review of the evidence, and implications. *Aggression and Violent Behavior*, 16(1):63–73.

Liu, L., Yang, H., Fan, J., Wen, R., and Duan, Y. (2019). Rician noise and intensity nonuniformity correction (nnc) model for mri data. *Biomedical Signal Processing and Control*, 49:506–519.

Maggioni, M., Katkovnik, V., Egiazarian, K., and Foi, A. (2013). A nonlocal transform-domain filter for volumetric data denoising and reconstruction. *IEEE Transactions on Image Processing*, 22(1):119–133.

Makropoulos, A., Gousias, I. S., Ledig, C., Aljabar, P., Serag, A., Hajnal, J. V., Edwards, A. D., Counsell, S. J., and Rueckert, D. (2014). Automatic whole brain mri segmentation of the developing neonatal brain. *IEEE Transactions on medical imaging*, 33(9):1818–1831.

Malini, S. and Moni, R. S. (2015). Image denoising using multiresolution singular value decomposition transform. *Procedia Computer Science*, 46:1708–1715.

Mandal, P. K., Banerjee, A., Tripathi, M., and Sharma, A. (2018). A comprehensive review of magnetoencephalography (meg) studies for brain functionality in healthy aging and alzheimer's disease (ad). *Frontiers in Computational Neuroscience*, 12(60).

Manjón, J. V., Carbonell, J., Lull, J., García, G., Martí, L., and Robles, M. (2008). Mri denoising using non-local means. *Medical Image Analysis*, 12(4):514–523.

Manjón, J. V. and Coupé, P. (2016). volbrain: An online mri brain volumetry system. *Frontiers in Neuroinformatics*.

Manjón, J. V., Coupé, P., and Buades, A. (2015). Mri noise estimation and denoising using non-local pca. *Medical Image Analysis*, 22(1):35–47.

Manjón, J. V., Coupé, P., Buades, A., Collins, L., and Robles, M. (2012). New methods for mri denoising based on sparseness and self-similarity. *Medical Image Analysis*, 16(1):18–27.

Maosong, R., Jinrong, H., Yang, C., Hu, C., Huaiqiang, S., Jiliu, Z., and Yi, Z. (2019). Denoising of 3d magnetic resonance images using a residual encoderdecoder wasserstein generative adversarial network. *Medical Image Analysis*, 55:165–180.

McKeown, M. J., Makeig, S., Brown, G. G., Jung, T. P., Kindermann, S. S., Bell, A. J., and Sejnowski, T. (1998). Analysis of fmri data by blind separation into independent spatial components. *Human Brain Mapping*, 6(3):160–188.

Mesejo, P., Valsecchi, A., Marrakchi-Kacem, L., Cagnoni, S., and Damas, S. (2015). Biomedical image segmentation using geometric deformable models and metaheuristics. *Computerized Medical Imaging and Graphics*, 43:167–178.

Mohan, J., Krishnaveni, V., and Guo, Y. (2014). A survey on the magnetic resonance image denoising methods. *Biomedical Signal Processing and Control*, 9:56–69.

Moradi, N. and Mahdavi-Amiri, N. (2019). Kernel sparse representation based model for skin lesions segmentation and classification. *Computer Methods and Programs in Biomedicine*, 182.

Odgers, C. L., Burnette, M. L., Chauhan, P., Moretti, M. M., and Reppucci, D. (2005). Misdiagnosing the problem: Mental health profiles of incarcerated juveniles. *The Canadian Child and Adolescent Psychiatry Review*, 14(1):26–29.

Ogawa, S., Lee, T. M., Nayak, A. S., and Glynn, P. (1990). Oxygenation-sensitive contrast in magnetic resonance image of rodent brain at high magnetic fields. *Magnetic Resonance in Medicine*, 14(68-78).

Oghabian, M. (2020). Mri artifacts causes and correction. `http://www.oghabian.net/download/MRI%20Artifacts%20Causes%20and%20Correction.pdf`. [Web; accessed on 04-18-2020].

Osipova, D., Rantanen, K., Ahveninen, J., Ylikoski, R., Happola, O., Stranberg, T., and Pekkonen, E. (2006). Source estimation of spontaneous meg oscillations in mild cognitive impairment. *Neuroscience Letters*, 45(1-2):57–61.

Otsu, N. (1979). A threshold selection method from gray-level histograms. *IEEE Transactions on Systems, Man, and Cybernetics*, 9(1):62–66.

Paquola, C., Bennett, M. R., and Lagopoulos, J. (2016). Understanding heterogeneity in grey matter research of adults with childhood maltreatment—a meta-analysis and review. *Neuroscience and Biobehavioral Reviews*, 69:299–312.

Passat, N., Ronse, C., Baruthio, J., Armspach, J. P., Maillot, C., and Jahn, C. (2005). Region-growing segmentation of brain vessels: an atlas-based automatic approach. *Journal of Magnetic Resonance Imaging*, 21(6):715–725.

Peng, Z., Qu, S., and Li, Q. (2019). Interactive image segmentation using geodesic appearance overlap graph cut. *Signal Processing: Image Communication*, 78:159–170.

Pham, D. L., Xu, C., and Prince, J. L. (2000). Current methods in medical image segmentation. *Annual Review of Biomedical Engineering*, 2(2000):315–337.

Phophalia, A. and Mitra, S. K. (2017). 3d mr image denoising using rough set and kernel pca method. *Magnetic Resonance Imaging*, 36:135–145.

Pieciak, T., Rabanillo-Viloria, I., and Aja-Fernández, S. (2018). Bias correction for non-stationary noise filtering in mri. In *IEEE 15th International Symposium on Biomedical Imaging (ISBI 2018)*, pages 307–310, Washington, DC, USA.

Prastawa, M. (2007). *An MRI segmentation framework for brains with anatomical deviations*. PhD thesis, University of North Carolina at Chapel Hill.

Prastawa, M., Gilmore, J. H., Lin, W., , and Gerig, G. (2005). Automatic segmentation of mr images of the developing newborn brain. *Medical Image Analysis*, 9(5):457–466.

Prescott, J. W. (2013). Quantitative imaging biomarkers: The application of advanced image processing and analysis to clinical and preclinical decision making. *Journal of Digital Imaging*, 26(1):97–108.

Prewitt, J. M. S. (1970). Object enhancement and extraction. In *Picture Processing and Psychopictorics*, pages 75–149. Academic Press, New York.

Purcell, E. M., Torrey, H. C., and Pound, R. V. (1946). Resonance absorption by nuclear magnetic moments in a solid. *Physical Review*, 69(1-2):37–38.

Raghuvanshi, D., Hasan, S., and Agrawal, M. (2012). Analysing image denoising using non local means algorithm. *International Journal of Computer Applications*, 56(13):7–11.

Rajwade, A., Rangarajan, A., and Banerjee, A. (2012). Image denoising using the higher order singular value decomposition. *IEEE Transactions on Pattern Analysis and Machine Intelligence*, 35(4):849–862.

Ramirez, I., Sprechmann, P., and Sapiro, G. (2010). Classification and clustering via dictionary learning with structured incoherence and shared features. In *IEEE Computer Society Conference on Computer Vision and Pattern Recognition*, pages 3501–3508, San Francisco, CA, USA.

Renfrew, D. L., Franken, E. A., Berbaum, K. S., Weigelt, F. H., and Abu-Yousef, M. M. (1992). Error in radiology: classification and lessons in 182 cases presented at a problem case conference. *Radiology*, 183(1):145–150.

Rinck, P. A. (2015). *Magnetic Resonance in Medicine: The Basic Textbook of the European Magnetic Resonance Forum*. Wiley-Blackwell.

Roberts, L. G. (1965). Machine perception of three-dimensional solids. *Optical and Electro-Optical Information Processing*, pages 159–197.

Romero, C., Ghisi, J. P., Mazzucco, J., and Ternak, A. (2007). Imágenes con tensor de difusión en resonancia magnética. *Revista argentina de neurocirugía*, 21(1):49–52.

Sadek, R. (2012). Svd based image processing applications: State of the art, contributions and research challenges. *International Journal of Advanced Computer Science and Applications - IJACSA*, 3(7):26–34.

Sato, J. R., de Oliveira-Souza, R., Thomaz, C. E., Basílio, R., Bramati, I. E., Jr, E. A., Tovar-Moll, F., Hare, R. D., and Moll, J. (2011). Identification of psychopathic individuals using pattern classification of mri images. *Social Neuroscience*, 6(5-6):627–639.

Schacter, D., Gilbert, D. T., and Wegner, D. M. (2011). *Psychology (2nd Edition)*. Worth, New York.

Schiffer, B., Müller, B. W., Scherbaum, N., Hodgins, S., Forsting, M., Wiltfang, J., Gizewski, E. R., and Leygraf, N. (2011). Disentangling structural brain alterations associated with violent behavior from those associated with substance use disorders. *Archives of General Psychiatry*, 68(10):1039–1049.

Sprechmann, P. and Sapiro, G. (2010). Dictionary learning and sparse coding for unsupervised clustering. In *IEEE International Conference on Acoustics, Speech and Signal Processing*, pages 2042–2045, Dallas, TX, USA.

Stam, C. J., Jones, B. F., Manshanden, I., A. van Cappellen van Walsum, T. M., Verbunt, J., de Munck, J., van Dijk, B., Berendse, H., and Scheltens, P. (2006). Magnetoencephalographic evaluation of resting-state functional connectivity in alzheimer's disease. *Neuroimage*, 32(3):1335–1344.

Stosic, D., Stosic, D., Ludermir, T. B., and Ren, T. I. (2019). Natural image segmentation with non-extensive mixture models. *Journal of Visual Communication and Image Representation*, 63.

Tampere University of Technology, D. (2019). Image and video denoising by sparse 3d transform-domain collaborative filtering. http://www.cs.tut.fi/ foi/GCF-BM3D/.

Tang, Y., Long, J., Wang, W., Liao, J., Xie, H., Zhao, G., and Zhang, H. (2016). Aberrant functional brain connectome in people with antisocial personality disorder. *Scientific Reports*, 6(26209):1–12.

Tao, D., Cheng, J., Gao, X., Li, X., and Deng, C. (2016). Robust sparse coding for mobile image labeling on the cloud. *IEEE Transactions on Circuits and Systems for Video Technology*, 27:62–72.

Tong, T., Wolz, R., , P. C., Hajnal, J. V., and Rueckert, D. (2013). Segmentation of mr images via discriminative dictionary learning and sparse coding: Application to hippocampus labeling. *NeuroImage*, 76(1):11–23.

Turek, J. (2015). *Topics in Sparse Representation Modeling and Applications*. PhD thesis, Technion — Israel Institute of Technology.

Uddin, L. Q., Kelly, A. M. C., Biswal, B. B., Margulies, D. S., Shehzad, Z., Shaw, D., Ghaffari, M., Rotrosen, J., Adler, L. A., Castellanos, F. X., and Milham, M. (2008). Network homogeneity reveals decreased integrity of default-mode network in adhd. *Journal of Neuroscience Methods*, 169(1):249–254.

Underwood, L. A. and Washington, A. (2016). Mental illness and juvenile offenders. *International Journal of Environmental Research and Public Health*, 13(2):228–242.

United Nations Environment Programme, ILO, and WHO (2001). Biomarkers in risk assessment: Validity and validation. http://www.inchem.org/documents/ehc/ehc/ehc222.htm. [Web; accessed on 05-14-2019].

Valencia, M. and Cuartas, J. M. (2016). Potential biomarkers in personality disorders: current state and future research. *International Journal of Psychological Research*, 9(1):98–112.

Veraart, J., Novikov, D. S., Christiaens, D., Ades-aron, B., Sijbers, J., and Fieremans, E. (2016). Denoising of diffusion mri using random matrix theory. *NeuroImage*, 142(15):394–406.

Wang, G., Liu, Y., Xiong, W., and Li, Y. (2018a). An improved non-local means filter for color image denoising. *Optik*, 173:157–173.

Wang, H., Xiao, X., Peng, X., Liu, Y., and Zhao, W. (2017). Improved image denoising algorithm based on superpixel clustering and sparse representation. *Applied Sciences*, 7(5).

Wang, H. and Yushkevich, P. A. (2013). Multi-atlas segmentation with joint label fusion and corrective learning-an open source implementation. *Frontiers in Neuroinformatics*, 7:1–12.

Wang, M., Yan, W., and Zhou1, S. (2018b). Image denoising using singular value difference in the wavelet domain. *Mathematical Problems in Engineering*, 2018:1–19.

Wang, Z., Bovik, A. C., Sheikh, H. R., and Simoncelli, E. P. (2004). Image quality assessment: From error visibility to structural similarity. *IEEE Transactions on Image Processing*, 13(4):600–612.

Weglinski, T. and Fabijanska, A. (2011). Brain tumor segmentation from mri data sets using region growing approach. In *Proceedings of the 7th International Conference on Perspective Technologies and Methods in MEMS Design (MEMSTECH'11)*, page 185–188.

Weisenfeld, N. I. and Warfield, S. K. (2009). Automatic segmentation of newborn brain mri. *NeuroImage*, 47(2):564–572.

Xu, P., Chen, B., Xue, L., Zhang, J., Zhu, L., and Duan, H. (2019). A new mnfbm4d denoising algorithm based on guided filtering for hyperspectral images. *ISA Transactions*, 92:315–324.

Xue, H., Srinivasan, L., and Jiang, S. (2007). Automatic segmentation and reconstruction of the cortex from neonatal mri. *NeuroImage*, 38(3):461–477.

Yuan, J. (2019). Mri denoising via sparse tensors with reweighted regularization. *Applied Mathematical Modelling*, 69:552–562.

Yushkevich, P. A., Piven, J., Hazlett, H. C., Smith, R. G., Ho, S., Gee, J. C., and Gerig, G. (2006). User-guided 3d active contour segmentation of anatomical structures: significantly improved efficiency and reliability. *Neuroimage*, 31(3):1116–1128.

Zhang, K. (2020). Beyond a gaussian denoiser: Residual learning of deep cnn for image denoising (tip, 2017). https://github.com/cszn/DnCNN/tree/4a4b5b8bcac5a5ac23433874d4362329b25522ba. [Web; accessed on 02-02-2020].

Zhang, K., Zuo, W., Chen, Y., Meng, D., and Zhang, L. (2017). Beyond a gaussian denoiser: Residual learning of deep cnn for image denoising. *IEEE Transactions on Image Processing*, 26(7):3142–3155.

Zhang, X., Peng, J., Xu, M., Yang, W., Zhang, Z., Guo, H., , Chen, W., Feng, Q., Wu, E. X., and Feng, Y. (2017). Denoise diffusion-weighted images using higher-order singular value decomposition. *NeuroImage*, 156:128–145.

Zhang, X., Xu, Z., Jia, N., Yang, W., Feng, Q., Chen, W., and Feng, Y. (2015a). Denoising of 3d magnetic resonance images by using higher-order singular value decomposition. *Medical Image Analysis*, 19(1):75–86.

Zhang, Y., Yang, Z., Hu, J., Zou, S., and Fu, Y. (2019). Mri denoising using low rank prior and sparse gradient prior. *IEEE Access*, 7:45858–45865.

Zhang, Z., Xu, Y., Yang, J., Li, X., and Zhang, D. (2015b). A survey of sparse representation: Algorithms and applications. *IEEE Access*, 3:490–530.

Zheng, Y., Jeon, B., Xu, D., Wu, J. Q., and Zhang, H. (2015). Image segmentation by generalized hierarchical fuzzy c-means algorithm. *Journal of Intelligent and Fuzzy Systems*, 28(2):961–973.

Zhou, Z., Tian, R., Wang, Z., Yang, Z., Liu, Y., Liu, G., Wang, R., Gao, J., Song, J., Nie, L., and Chen, X. (2017). Artificial local magnetic field inhomogeneity enhances t2 relaxivity. *Nature Communications*, 8:1–10.

Zhuo, J. and Gullapalli, R. P. (2006). Teaching points for aapm/rsna physics tutorial for residents: Mr artifacts, safety, and quality control. *Radio Graphics*, 26.